UNIVERSIDADE ESTADUAL PAULISTA
"JÚLIO DE MESQUITA FILHO"
Campus de Ilha Solteira - SP

Roberta Irma Martin

Nonlinear control system based on variable structure and sliding modes for two beam optical interferometry

Ilha Solteira

2018

Roberta Irma Martin

Nonlinear control system based on variable structure and sliding modes for two beam optical interferometry

Thesis submitted to the Faculdade de Engenharia de Ilha Solteira as requisite to obtain the degree of PhD in Electrical Engineering.
Field of Expertise: Automation

Advisor: Cláudio Kitano
Co-Advisor: Marcelo Carvalho Minhoto Teixeira

Ilha Solteira
2018

FICHA CATALOGRÁFICA
Desenvolvido pelo Serviço Técnico de Biblioteca e Documentação

M379n

Martin, Roberta Irma.
Nonlinear control system based on variable structure and sliding modes for two beam optical interferometry / Roberta Irma Martin. -- Ilha Solteira: [s.n.], 2018
125 f. : il.

Tese (doutorado) - Universidade Estadual Paulista. Faculdade de Engenharia de Ilha Solteira. Área de conhecimento: Automação, 2018

Orientador: Cláudio Kitano
Co-orientador: Marcelo Carvalho Minhoto Teixeira
Inclui bibliografia

1. Interferometria óptica de dois feixes. 2. Controle não linear. 3. Estrutura variável e modos deslizantes.

Raiane da Silva Santos
Supervisora Técnica de Seção
Seção Técnica de Referência, Atendimento ao usuário e Documentação
Diretoria Técnica de Biblioteca e Documentação
CRB/8 - 9999

unesp

UNIVERSIDADE ESTADUAL PAULISTA

Câmpus de Ilha Solteira

CERTIFICADO DE APROVAÇÃO

TÍTULO DA TESE: Nonlinear control system based on variable structure and sliding modes for two beam optical interferometry

AUTORA: ROBERTA IRMA MARTIN
ORIENTADOR: CLAUDIO KITANO
COORIENTADOR: MARCELO CARVALHO MINHOTO TEIXEIRA

Aprovada como parte das exigências para obtenção do Título de Doutora em ENGENHARIA ELÉTRICA, área: AUTOMAÇÃO pela Comissão Examinadora:

Prof. Dr. CLAUDIO KITANO
Departamento de Engenharia Elétrica / Faculdade de Engenharia de Ilha Solteira

Prof. Dr. RICARDO TOKIO HIGUTI
Departamento de Engenharia Elétrica / Faculdade de Engenharia de Ilha Solteira

Prof. Dr. JEAN MARCOS DE SOUZA RIBEIRO
Departamento de Engenharia Elétrica / Faculdade de Engenharia de Ilha Solteira

Prof. Dr. GILDER NADER
Centro de Metrologia de Fluidos / Instituto de Pesquisas Tecnológicas

Prof. Dr. NICOLAU ANDRÉ SILVEIRA RODRIGUES
Departamento de Física / Instituto Tecnológico de Aeronáutica

Ilha Solteira, 21 de março de 2018

Acknowledgements

For the accomplishment of this thesis the support and endeavor of many people was necessary, whom I would like to thank.

I would like to thank Dr. Cláudio Kitano
for the advisement, friendship, knowledge and character imparted to me and...
...if the band you're in starts playing different tunes
I'll see you on the dark side of the Moon
I can't think of anything to say, except
I think it's marvellous!

To Dr. Marcelo C. M. Teixeira
for the advisement, great creativity and support with the control theory which was essential for this work. Also, for always placing a pole on the right side of my ideas!

To Dr. João Marcos S. Sakamoto
for receiving me in his laboratory, for the friendship and encouragement. Also, for the imagination and bright ideas to carry on this research.

To the FEIS-UNESP employees and technicians, especially for Everaldo for the patience, friendship, teas, discussions, for taking care of Roben and for all the hard and respectful work.

To the IEAv-CTA
for receiving me in its laboratory and for lending opto-electronics components.

Special thanks to Renato
for the enjoyable partnership, great patience and for the observations and discussions about digital signal processing and Pink Floyd.

To my friends and roommates Perdido and Castor
for the productive discussions about the control theory, digital systems and some other quite less productive subjects.

To my parents, Joao and Elza, and my brother, Rodolfo.

To my friends Etieny, Bruno, Stephany, Kelly, Martin, Guilherme and Fernando
for all the support, ear lending, laughs, coffees, hamburgers, games, and strength. The road would have been much more difficult and boring without you.

And all that is now
And all that is gone
And all that's to come
And everything under the Sun is in tune
But the Sun is eclipsed by the Moon.
Roger Waters - Eclipse (The Dark Side of the Moon)

Abstract

This work presents the theoretical and experimental study of a nonlinear control system designed for two beam optical interferometry based on variable structure and sliding modes. The proposed system presents high accuracy, robustness and, furthermore, is simple and low cost, increasing the measurement capability for different applications of interferometric sensors. Compared with other control techniques applied in optical interferometry, this control technique presents important features and takes in account the nonlinear characteristic of the interferometer, increasing its measurement capability. Consequently, a reset circuit is not necessary, the interferometer can work in harsh environments, the assembly and adjustment of the parameters is simpler (easy implementation), with simple setup and the effective cost, achieving high robustness and accuracy. Regarding demodulation techniques based on signal spectrum (J1..J4), the proposed system has a higher dynamic range, resolution, can measure time delay and operate with arbitrary signal waveforms. Also, it improves the temporal demodulation methods increasing the accuracy for small amplitude signals, maintaining the quadrature condition (maximum point of sensitivity) and, therefore, eliminates the effect of signal fading, even under strong external disturbances around the interferometer setup such as vibration, temperature variation and air current flow. The stability of the linearized system was studied through the Lyapunov's linearization method and the local stability of the equilibrium points were proved. Through the phase plane method, we considered all the nonlinearities from the system, and we proved that for any initial condition, the nonlinear system is stable and converges to the equilibrium point. As a result, the system is globally asymptotically stable and it does not tend to a limit cycle nor to instability. Finally, we obtained the Lyapunov equation for the nonlinear system taking into account the phase plane analysis, proving the system's stability. Therefore, this approach can fully compensate the nonlinear behavior of the interferometer, keep it in the quadrature point and suppress the signal fading for arbitrary signal waveforms, sinusoidal signals or zero input signal, even under strong external disturbances. The system proved to be suitable for dynamic operations, in different applications as: characterization of piezoelectric actuators, characterization of fiber response to temperature, ultrasound detection and the detection of longitudinal waves generated by a Q-switched laser on aluminum and steel samples, as shown in this work. The high robustness allows the system to be embedded and to operate in harsh environments such as factories, bringing the interferometry outside the laboratory.

Keywords: Two beam optical interferometry. Nonlinear control. Variable Structure and sliding modes.

Resumo

Este trabalho apresenta um estudo teórico e experimental de um sistema de controle não linear baseado em estrutura variável e modos deslizantes desenvolvido para interferômetro de dois feixes. O sistema proposto apresenta alta precisão, robustez e, além disso, é simples e de baixo custo, aumentando a capacidade de medição para diferentes aplicações de sensores interferométricos. Comparado a outras técnicas de controle aplicadas a interferometria óptica, esta técnica apresenta importantes vantagens e leva em consideração a característica não linear do interferometro, aumentando seu poder de medição. Consequentemente, um circuito de reset não é necessário, o interferometro pode trabalhar em ambientes com grandes perturbações, a montagem e ajuste dos parâmetros é mais simples (fácil implementação), com simples configuração e custo efetivo, atingindo alta robustez e acurácia. Comparado as técnicas de demodulação baseado no espectro do sinal (J1..J4), o sistema proposto tem faixa dinâmica e resolução maiores, podendo medir atraso no tempo e operar com formas de onda arbitrárias. Além disso, aperfeiçoa os métodos de demodulação temporais aumentando a precisão para sinais de baixa amplitude, mantendo a condição de quadratura (ponto máximo de sensibilidade) e, portanto, elimina o efeito do desvanecimento do sinal, mesmo diante de grandes perturbações ao redor do sistema como, vibrações, variações de temperatura e correntes de ar. A estabilidade do sistema linearizado foi estudada através do método de linearização de Lyapunov e a estabilidade local dos pontos de equilíbrio foram provadas. Através do método do plano de fase, todas as não linearidades do sistema foram consideradas, e provou-se que para qualquer condição inicial, o sistema não linear é estável e converge para o ponto de equilíbrio. Como resultado, o sistema é globalmente assintóticamente estável e não tende a um ciclo limite ou à intabilidade. Finalmente, foi obtido a equação de Lyapunov do sistema não linear considerando a análise do plano de fase, provando novamente a estabilidade do sistema de controle. Portanto, essa abordagem pode compensar o comportamento não linear do interfometro, mantendo-o na condição de quadratura e eliminando o efeito do desvanecimento do sinal para formas de onda arbitrárias, senoidais ou sem sinal de entrada, mesmo diante de grandes perturbações externas. O sistema provou ser eficiente para operações dinâmicas em diferentes aplicações como: caracterização de atuadores piezoelétricos, caracterização da resposta da fibra à temperatura, detecção de ultrassom e detecção de ondas longitudinais geradas por um laser Q-switched em amostras de alumínio e aço, conforme mostrado neste trabalho. A alta robustez oferecida pelo controlador permite que o sistema seja embarcado e opere em ambientes com grandes perturbações como fábricas, trazendo a interferometria para fora do laboratório.

Palavras-chave: Interferometria óptica de dois feixes. Controle não linear. Estrutura variável e modos deslizantes.

List of Figures

List of Tables

Contents

1 Introduction

The development of optical interferometry sensors has increased during the 20th century, due to the laser advent in 1960 (MAIMAN, 1960) and their high spatial and temporal coherence. The interference pattern, it is possible to detect physical quantities with high accuracy. The interference pattern occurs by the superposition of two or more light waves, producing a result that is the sum of the intensity of the overlapping wave contributions. For instance, if two harmonic waves with the same frequency, amplitude, polarization and direction are in-phase, the resultant at each point is the sum of the intensities, called total constructive interference. On the other hand, when the phase difference between the two waves is 180°, the intensities will be subtracted and we have other extreme, called total destructive interference (HECHT, 2002). This intensity distribution is called fringe interference pattern.

A laser interferometer is a high sensitivity instrument that converts a physical quantity variation in optical phase variation which, in turn, is converted to optical intensity that can be electronically measured. Therefore, several types of physical quantities can be measured with the induction of an optical phase variation in one of the interferometer arms, e.g., displacement (XIE et al., 2010), temperature, pressure (HOCKER, 1979), strain (MURPHY et al., 1991), angular velocity (VALI; SHORTHILL, 1976) and many other physical parameters.

Extremely small values of these physical quantities can be detected by interferometers, as described in the literature (UDD; SPILLMAN, 2011; GIALLORENZI et al., 1982). Regarding mechanical displacement measurement, the interferometry is able to detect a vibration amplitude on the order of 10^{-14} m for a conventional system (YIMNIRUN et al., 2003), that is, with the length of the arms smaller than 0.5 m. The interferometry can be applied in nanotechnology (DEVASIA; ELEFTHERIOU; MOHEIMANI, 2007), positioning of samples, microelectronics (VERMA; KIM; SHAKIR, 2005), cell manipulation (PUTRA et al., 2007), electronic microscopy instruments (YU et al., 1999), lens positioning for laser interferometers (JING et al., 2002) and many other sectors of fine mechanics, where microscopic and precise positioning of parts are required.

However, due to its high sensitivity and ability to detect such small displacements, the interferometer also detects spurious environmental disturbances as, for instance, spurious temperature variations (on the scale of micro kelvin), nano-mechanical vibrations, air turbulence, and so on. Considering the nonlinear nature of the interferometer characteristic curve, these effects contribute to generate signal fading (SHEEM; GIALLORENZI; KOO, 1982), leading to ambiguity of results and direction (CHEN et al., 2014). This behavior

usually leads to a nontrivial process to extract the interest signal, due to the complexity of the signal demodulation process, since it is phase-modulated with a superimposed fading signal.

1.1 Optical phase homodyne demodulation techniques

In order to overcome these problems, several techniques for signal demodulation and fading minimization were developed, as homodyne and heterodyne techniques, with spectral or temporal methods and open loop or closed loop methods. In this work, we are concerned on detection of small input signal amplitude (less than $\pi/2$ rad). Therefore, we are focused on active homodyne detection, since it can offer a lower noise floor than the one achieved by heterodyne techniques, usually limited by laser frequency, intensity and acoustic noise (MOORE et al., 2002).

Homodyne demodulation techniques based on signal spectrum demodulation (SUDARSHANAM; SRINIVASAN, 1989; SUDARSHANAM; CLAUS, 1993) are restrictive in terms of dynamic range, resolution, time delay measurement, and operation with arbitrary signal waveforms. When compared with spectral methods, the temporal methods (BARBOSA et al., 2010; CHEN et al., 2014; CONNELLY; GALETI; KITANO, 2015; GALETI; KITANO; CONNELLY, 2015; PANG et al., 2007; PISANI, 2009; ZHEN et al., 2010) are more versatile and powerful, being intensified by the wide dissemination of modern data acquisition systems available on the market (powerful acquisition and control platforms as Digital Signal Processors (DSPs), Field Programmable Gate Arrays (FPGAs), among others).

However, while spectral methods benefit from passive (open loop operation) compensation of the fading problem, temporal methods (BARBOSA et al., 2010; CHEN et al., 2014; CONNELLY; GALETI; KITANO, 2015; GALETI; KITANO; CONNELLY, 2015; PANG et al., 2007; PISANI, 2009; ZHEN et al., 2010) require active (closed loop operation) compensation techniques for small amplitude signals (less than $\pi/2$ rad), in order to (i) maintain the interferometer in quadrature condition (maximum point of sensitivity) and, therefore, eliminate the effect of signal fading; or (ii) linearize the interferometric characteristic curve by operating in the high-gain mode (CHEUNG; BARNES; HASKELL, 2003), converting the sinusoidal characteristic curve to a straight segment (SHIRAI; BARNES; HASKEL, 1999).

1.2 Nonlinear control approach

Linear control methods have been regularly employed in order to stabilize interferometers and accurately estimate phase (BARNES et al., 2002; CHEUNG; BARNES;

HASKELL, 2003; FRITSCH; ADAMOVSKY, 1981; JACKSON et al., 1980; WHITE; EMMONY, 1985). Despite the wide variety of linear systems techniques, their use applied to nonlinear systems, such as interferometers, can bring limitations and do not ensure the necessary robustness in system performance, since that, to maintain its value, linear control methods rely on the key assumption that the disturbance has a value small enough to keep the system at the equilibrium point. For the cases in which the disturbance is large enough to take the system out of the equilibrium point, a linear controller is likely to present a very poor performance or even to be unstable, due to its inability to deal with the nonlinearities in the system. Therefore, the disturbance may not be properly compensated. In fact, there are linear control systems that handle with large disturbances, but they usually have reset circuits in their composition, which increases the system complexity. At the same time, the reset voltage action can interrupt the measurement process, severely compromising the phase detection capability of the sensor. In recent publications, solutions for this issue have been described, through the use of an optical fiber Michelson interferometer and fiber Bragg gratings (FBGs) (XIE; CHEN; REN, 2009; XIE; CHEN; ZHANG, 2009). However, although presenting good functioning in controlled environments such as laboratories, these systems can be difficult to be used in real-world applications.

In order to overcome these issues, modern control techniques, such as robust control laws and Linear Matrix Inequalities (LMIs) were applied in Hui et al. (2013) and Deng et al. (2017) for interferometric system and in similarly equated systems using high voltage optical sensors. However, in the context of LMIs applied in these systems, the projects still take into account the linearized system.

Following a novel perspective, the main objective of this work is to develop a nonlinear control system designed for two beam optical interferometry, based on variable structure control and sliding modes. This approach can fully compensate the nonlinear behavior in the interferometer and lead to high accuracy control for very large disturbances, providing ease of implementation and high robustness (SLOTINE; LI et al., 1991). Reset circuitry is not necessary, which means that there are not spurious signals generated by the reset process, providing considerably decrease in the cost and complexity of hardware systems and circuitry.

The high robustness provided by this approach allows the system to be embedded and operate in places with high mechanical or environmental disturbances, being suitable to operate in harsh environments such as industries and factories, bringing the interferometry to outside the laboratory.

This control scheme was applied to a bulk Michelson interferometer and to an optical fiber Mach-Zehnder interferometer, and can be easily applied to various other systems that are similarly equated, such as Sagnac interferometers. The key components,

principles of operation, stability study and an example of application are presented.

1.3 Thesis outline

For a better understanding of the theme, this work is divided in six chapters. In Chapter 2 it is presented fundamentals of optical interferometry theory, and the principle of operation and the scheme of a bulk Michelson and all-fiber Mach-Zehnder interferometer. In Chapter 3, we present the mathematical model of the proposed nonlinear control to stabilize the interferometric system, and the system's stability study. Computational simulations are performed, based on mathematical modeling. Details of the different interferometers configuration used regarding the application of the nonlinear control technique are shown in Chapter 4, as well as details of the analog and digital control implementation. In Chapter 5 the experimental results considering the application of the nonlinear control technique in the bulk Michelson and all-fiber Mach-Zehnder interferometer are presented, as well as the different interferometers configuration used. The experimental phase plane was acquired and compared with simulation curves for different situations, in order to validate the model. After that, the controlled interferometers were tested on dynamic operation, first in the characterization of the optical fiber response to temperature, characterization of piezoelectric actuators and later to detect ultrasound waves directly from the surface of the sample. Finally, in Chapter 6, the main conclusion of this work are presented, as well as some proposed future works.

2 Optical Interferometry

In this chapter, the fundamentals of optical interferometry theory are presented, as well as the principles of operation and the schemes of a bulk Michelson and an all-fiber Mach-Zehnder interferometers.

2.1 Bulk Michelson Interferometer

The bulk Michelson interferometer configuration is shown in Fig. 1. The laser beam is split in two by the beam-splitter; one of these beams, called reference beam (or reference arm), travels towards the reference mirror and is reflected back, while the other one, called sensor beam (or sensor arm), travels towards the sample under evaluation and is also reflected back. The two beams are then recombined in the beam-splitter and directed towards the photodetector, which detects the interference signal.

Figure 1 – The bulk Michelson Interferometer.

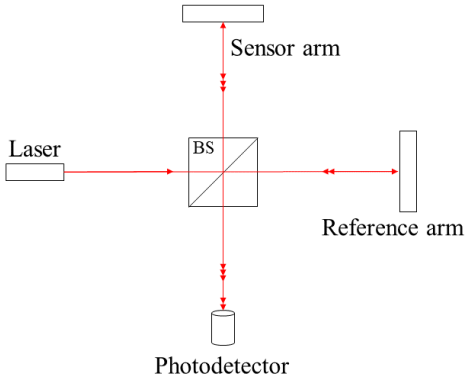

Source: From author.

The optical signal acquired from the photodetector is converted to electrical voltage by a transimpedance circuit. Considering an homodyne interferometer with the reference and the sensor beam generated by the same optical source, after passing through a neutral beam splitter, the two beams have identical polarization. Thereby, we can disregard the vectorial nature of these fields and perform a scalar analysis, using phasor notation.

Considering the interferometer configuration shown in Fig. 1, we can associate to the reference arm an electrical field with amplitude E_{01}, and to the sensor arm, E_{02}. Therefore, the electrical field of the interferometer originating from the reference ($E_R(t)$)

and the sensor ($E_S(t)$) arms, in rotating phasor representation, are:

$$E_R(t) = E_{01}e^{j\omega_o t} \tag{1a}$$

$$E_S(t) = E_{02}e^{j(\omega_o t+\phi(t))} \tag{1b}$$

where ω_o is the optical angular frequency and $\phi(t)$ is the optical phase delay between the two interferometric beams.

The total field is given by:

$$E_T = E_{01}e^{j\omega_o t} + E_{02}e^{j(\omega_o t+\phi(t))} \tag{2}$$

The output intensity of the interferometer is proportional to the average value of the Poynting vector, which is given by the dot product, as shown in (3):

$$I(t) = \frac{E_T.E_T^*}{2} \tag{3}$$

where $E_T.E_T^*$ is the product between the total electrical field and its complex conjugate.

Considering (2) and (3), we can obtain the output intensity:

$$I(t) = (|E_{01}|^2 + |E_{02}|^2 + E_{01}E_{02}e^{j\phi(t)} + E_{01}E_{02}e^{-j\phi(t)})/2 \tag{4}$$

where E_{01} and E_{02} are real.

The optical frequency ω_o (in the order of 10^{14} rad/s) was supressed in (4), since the practical photodetector has a low pass characteristic, and cannot respond to this frequency order. However, it can acquire the lower temporal variations of $\phi(t)$.

Rewriting (4) and using the Euler identity (MILNE-THOMSON; ABRAMOWITZ; STEGUN, 1972), we have:

$$I(t) = \frac{1}{2}\left[E_{01}^2 + E_{02}^2 + 2E_{01}.E_{02}\cos(\phi(t))\right] \tag{5}$$

Equation (5) can be separated into two components: optical intensities from individual sources (DC bias), and an interference term, given by the fields product. The interference term is associated with the fringe movement due the variation of the phase $\phi(t)$.

Rewriting (5) we obtain:

$$I(t) = \frac{E_{01}^2 + E_{02}^2}{2}\left[1 + \frac{2E_{01}.E_{02}}{E_{01}^2 + E_{02}^2}\cos(\phi(t))\right] \tag{6}$$

However, considering (3), the optical intensity in the reference and sensor arms can be rewritten as shown in (7a) and (7b):

$$I_R = E_{01}^2/2 \tag{7a}$$

$$I_S = E_{02}^2/2 \tag{7b}$$

Besides that, the output fringe visibility (V) of the interferometer indicates the contrast between maximum and minimum of $I(t)$. Therefore, V can be expressed by:

$$V = \frac{2E_{01}.E_{02}}{E_{01}^2 + E_{02}^2} = \frac{\sqrt{I_R I_S}}{(I_R + I_S)/2} \tag{8}$$

Rewriting (6) in terms of (7a), (7b) and (8), we obtain:

$$I(t) = (I_R + I_S)\,[1 + V\cos(\phi(t))] \tag{9}$$

If the beam splitter has a splitting ratio of 50:50, we will have a unity visibility (V), since the optical intensities I_R and I_S are equal. Therefore, the optical intensity in each interferometer arm will be the same, such that $E_{01} = E_{02} = E_0/\sqrt{2}$. Also, making $I_0 = E_0^2/2$, where I_0 is the optical intensity of the laser, then the interferometer output intensity can be established as:

$$I(t) = I_0\,[1 + V\cos\phi(t)] \tag{10}$$

To be strictly accurate, the visibility V ($0 \leqslant V \leqslant 1$) in (10) relies on several parameters such as coherence of optical source, alignment and polarization between the output beams. Therefore, in a practical situation, the $V = 1$ situation is difficult to be achieved. However, we can get close to it by adjusting the interferometer alignment.

Let us assume that an optical phase shift, given by $\phi(t)$ in the interferometer may be separated into a signal term, $\Delta\phi(t)$, and a static phase shift, ϕ_0, thus:

$$\phi(t) = \Delta\phi(t) + \phi_0 \tag{11}$$

where $\Delta\phi(t)$ is the signal of interest, and ϕ_0 happens due to the difference between the optical path lengths of the interferometer arms. The ϕ_0 term is given by (12) (UDD; SPILLMAN, 2011):

$$\phi_0 = \frac{2\pi}{\lambda} n_S l_S \tag{12}$$

where λ is the laser wavelength in vacuum, n_S is the refractive index and l_S is the total difference between the interferometer arms.

Considering that the signal of interest $\Delta\phi(t)$ can be caused by a variation in the refractive index (Δn_S) and/or in the arm length (Δl_S), when some perturbation to be measured actuates in the interferometer sensor arm, there is the occurrence of an optical phase shift, shown in (13):

$$\Delta\phi(t) = \frac{2\pi}{\lambda}\left[l_S\Delta n_S(t) + n_S\Delta l_S(t)\right]\chi \tag{13}$$

where χ is the sensibility factor, that is equal to 2 in the case of the Michelson interferometer, since the laser beam pass two times along its arms, doubling the sensibility (for the Mach-Zehnder interferometer, $\chi = 1$ is used). Considering also, that the medium of propagation is the air ($n_S = 1$) and that there is no refractive index variation, we obtain (14):

$$\Delta\phi(t) = \frac{2\pi}{\lambda}\left[\Delta l_S(t)\right]2 = \frac{4\pi}{\lambda}\left[\Delta l_S(t)\right] \tag{14}$$

For the purpose of characterization of linear systems, as in the case of piezoelectric actuators working in its linear region, we use the signal of interest $\Delta\phi(t)$ as a sinusoidal signal. Then, there is a proportional relation between $\Delta l_S(t)$ and $\Delta\phi(t)$, and we obtain the following relation:

$$\Delta\phi(t) = x\sin(\omega t) \tag{15}$$

where x is the phase modulation index in radians, and ω is the modulation frequency.

The intensity output is then converted to electrical voltage by a photodetector with a proportionality constant A using (10). Therefore, the interferometer output will become:

$$v(t) = A\left[1 + V\cos(\Delta\phi(t) + \phi_0)\right] \tag{16}$$

where the constant A accounts for the laser power, photodiode responsivity, amplifier gain, and V is the fringe visibility.

Ideally, ϕ_0 should be constant, however, due to spurious disturbances acting over the interferometer arm, it is actually a quasi-static quantity (variation occurs usually below 20 Hz), and in a few seconds the amplitude of this drift can easily be on the order of 2π rad or higher (UDD; SPILLMAN, 2011). This variation in ϕ_0 makes the interferometer operation point to vary with time, causing signal fading. This issue will be presented in Section 2.3.

2.2 All-fiber Mach-Zehnder interferometer

The all-fiber Mach-Zehnder interferometer configuration is shown in Fig. 2. The light from the beam is split in two by the fiber coupler 1, with part of the beam being transmitted to a reference fiber arm and the other part being transmitted to a sensor fiber arm. These two outputs, after passing through the sensor and reference coils, are recombined by the fiber coupler 2 and detected by the photodetectors ($PD1$ and $PD2$). Finally, a suitable demodulator is used to detect the phase modulated signal of interest.

Figure 2 – All-fiber Mach-Zehnder interferometer.

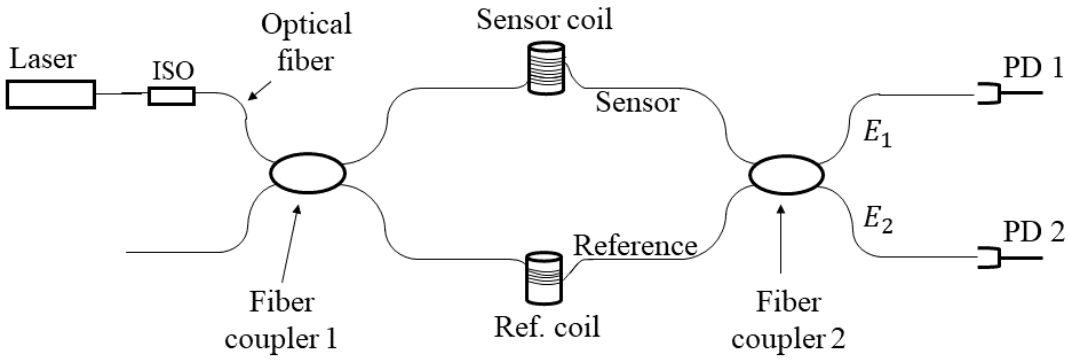

Source: From author.

Considering the power transmission coefficients for electrical field of the two couplers (t_1 and t_2) and optical power losses (α_R and α_S) associated with reference and sensor arms, respectively, the electrical fields at output 1 (E_1, in Fig. 2) of the interferometer originating from sensor, $E_S(t)$, and reference, $E_R(t)$, arms are:

$$E_R(t) = E_0\sqrt{\alpha_R(1-t_1)(1-t_2)}e^{j\left(\omega_o t+\phi_R+\frac{\pi}{2}+\frac{\pi}{2}\right)} \tag{17}$$

and

$$E_S(t) = E_0\sqrt{\alpha_S t_1 t_2}e^{j(\omega_o t+\phi_S)} \tag{18}$$

where E_0 is the laser field amplitude, ω_o is the optical frequency and, $\phi_{R,S}$ the optical phase shift. It should be noted that the two additional phase of $\pi/2$ rad in (17) are caused by crossed coupling.

The total field (E_T) incident on $PD1$ is given by:

$$E_T(t) = E_1(t) = E_0 e^{j\omega_o t}\left(\sqrt{\alpha_S t_1 t_2}e^{j\phi_S} - \sqrt{\alpha_R(1-t_1)(1-t_2)}e^{j\phi_R}\right) \tag{19}$$

The output intensity of the interferometer is proportional to the average value of the poynting vector, which is given by the dot product, as show in (3).

Using (19) and (3), the output intensity is given by:

$$I_1(t) = \frac{E_0^2}{2}\left[\alpha_S t_1 t_2 + \alpha_R(1-t_1)(1-t_2) - \sqrt{\alpha_R\alpha_S t_1 t_2(1-t_1)(1-t_2)}\left(e^{-j(\phi_R-\phi_S)} + e^{j(\phi_R-\phi_S)}\right)\right] \tag{20}$$

Using Euler identity and defining $|E_0^2|/2 = I_0$:

$$I_1(t) = I_0\left[\alpha_S t_1 t_2 + \alpha_R(1-t_1)(1-t_2) - 2\sqrt{\alpha_R\alpha_S t_1 t_2(1-t_1)(1-t_2)}\cos(\phi_R-\phi_S)\right] \tag{21}$$

The right side of (21) can be separated into an optical intensity of individual source (DC bias), and another one which is the interference term, associated with the fringe movement due the relative variation of the phases ϕ_R and ϕ_S.

Furthermore, the output fringe visibility (V_1) of the interferometer indicates the contrast between maximums and minimums of $I_1(t)$. Therefore, V can be expressed by:

$$V_1 = \frac{I_{max} - I_{min}}{I_{max} + I_{min}} \tag{22}$$

which from (21) gives:

$$V_1 = \frac{2\sqrt{\alpha_R\alpha_S t_1 t_2(1-t_1)(1-t_2)}}{\alpha_S t_1 t_2 + \alpha_R(1-t_1)(1-t_2)} \tag{23}$$

Considering the complementary output of the interferometer (E_2, in Fig. 2), we see that this has a similar output which is given by:

$$I_2(t) = I_0\left[\alpha_S t_1(1-t_2) + \alpha_R(1-t_1)t_2 + 2\sqrt{\alpha_R\alpha_S t_1 t_2(1-t_1)(1-t_2)}\cos(\phi_R-\phi_S)\right] \tag{24}$$

and the fringe visibility is given by:

$$V_2 = \frac{2\sqrt{\alpha_R\alpha_S t_1 t_2(1-t_1)(1-t_2)}}{\alpha_S t_1(1-t_2) + \alpha_R(1-t_1)t_2} \tag{25}$$

If the couplers have a splitting ratio of 0.5, i. e., $t_1 = t_2 = 0.5$, we will have equal visibilities ($V_1 = V_2 = V$). Furthermore, assuming $\alpha = \alpha_R = \alpha_S$ then $V = 1$ and $\phi = \phi_R - \phi_S$, we can rewrite (21) and (24) in the following manner:

$$I_1(t) = \frac{I_0\alpha}{2}(1-\cos\phi) \tag{26}$$

$$I_2(t) = \frac{I_0\alpha}{2}(1+\cos\phi) \tag{27}$$

2.3 Signal Fading

Due to its high sensitivity, the interferometer also detects spurious environmental disturbances (changing ϕ_0), such as temperature variations (on the scale of micro kelvin), nano-mechanical vibrations, air turbulence, and so on.

Considering (10) and (11), the slow variable phase ϕ_0 causes a variation in the total phase ϕ, that makes the operation point to vary with time, causing signal fading. Any random change in the length or in the refractive index of one arm of the interferometer produces a change in the amplitude of the detected signal. This behavior has several sources, and usually leads to a nontrivial process to extract the signal of interest, making the interferometer operation even more difficult.

In order to understand more deeply the problem, the phase shift ϕ in (10) will be replaced by two terms, as written in (11), ϕ_0, that represents an environmental low frequency phase bias that slowly drifts with time, and the signal of interest $\Delta\phi$, which represents the signal induced by the differential phase shift, i.e. $\phi = \Delta\phi + \phi_0$.

The intensity term I, from (10) is plotted in Fig. 3 as a function of ϕ. This intensity illustrates the small-signal response at different bias phases ϕ_0. When the bias phase is an odd multiple of $\pm\pi/2$ rad, the interferometer is in quadrature and exhibits a linear response (for small signal conditions: less than $\pi/2$ rad). Then, we can rewrite (10) as follows:

$$I(t) = \frac{I_0}{2}\left[1 + \cos\left(\Delta\phi + \frac{\pi}{2}\right)\right] = \frac{I_0}{2}\left[1 - \sin(\Delta\phi)\right] \tag{28}$$

Assuming $\Delta\phi(t) = x\sin(\omega t)$ with $x \ll \pi/2$ rad, and using $\sin(a) \cong a$, (28) can be rewritten as:

$$I(t) \cong \frac{I_0}{2}\left[1 - x\sin(\omega t)\right] = \frac{I_0}{2}(1 - \Delta\phi) \tag{29}$$

The second term in (29) is proportional to the signal of interest $\Delta\phi$. The linear response occurs for $\Delta\phi$ signals with peak values lower than $\pi/2$ rad. In this case, the signal waveform can be arbitrary.

When the bias phase is a multiple of $\pm\pi$ rad, the cosine function alternates between peaks and valleys. In this case, the small-signal response is attenuated and heavily distorted. This phenomenon is known as the bias-induced signal fading, which prevents the direct use of the interferometric output for most sensor applications.

The random phase drifts decreases the measurement accuracy and, in the worst case, may prevent the proper operation of the measurement system. Therefore, there is a

Figure 3 – Signal fading problem in interferometers.

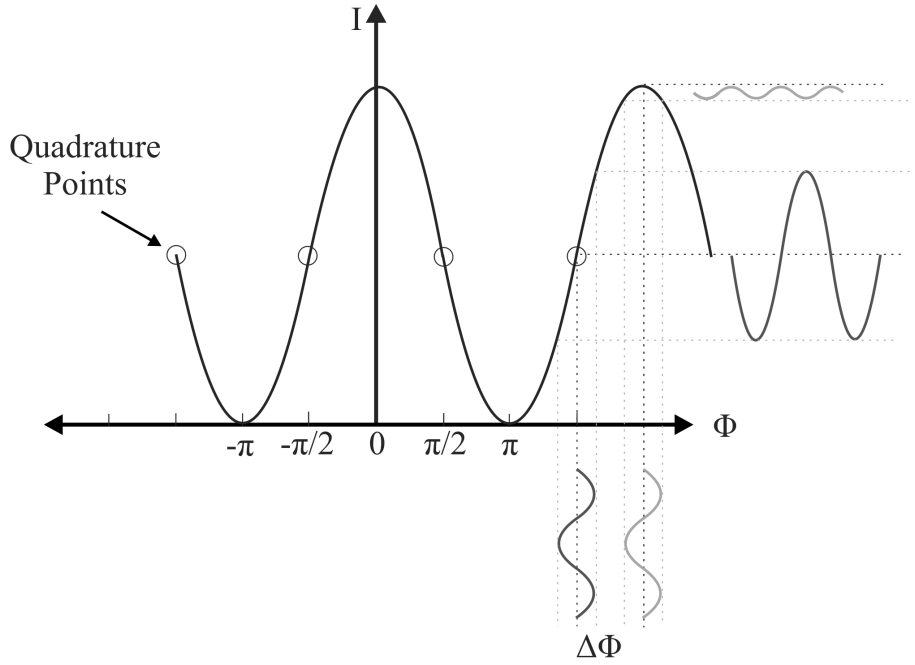

Source: From author.

problem of stabilization of the interferometer against environmental disturbances. This is, in fact, an usual problem for all types of two-beam interferometers.

As can be seen from (10), the output intensity (I) changes at a rate corresponding to the cosine of the phase shift (ϕ), which contains the information signal. The presence of this nonlinear function together with environmental drifts results in an interferometric signal fading, as shown in Fig. 3.

In cases in which $x \gg \pi/2$ rad, the output signal is not proportional to $\Delta\phi$, even under the quadrature condition. This behavior usually leads to a nontrivial process of extracting the signal of interest, due to the complexity of the signal demodulation process, since it is phase-modulated and superimposed with a fading signal.

In pursuance of overcoming these issues, several techniques for signal demodulation and fading minimization were developed, such as homodyne and heterodyne techniques (SUDARSHANAM; SRINIVASAN, 1989; SUDARSHANAM; CLAUS, 1993; PANG et al., 2007; PISANI, 2009; BARBOSA et al., 2010; CHEN et al., 2014) with spectral or temporal, open-loop or closed-loop methods.

In this work, we are concerned about the detection of small input signal amplitudes (less than $\pi/2$ rad). Therefore, we focus on active homodyne detection, since it can offer lower noise floor than that one achieved through the use of heterodyne techniques which, in turn, are usually limited by characteristics such as laser frequency, intensity and acoustic

noise (MOORE et al., 2002).

2.4 Demodulation of interferometric signals with nonlinear control system

In this work, two approaches for measuring the physical quantity under evaluation were employed: the low-gain approach for signals of interest with frequency above 20 Hz, and the modified high-gain approach for signals with frequency below 20 Hz.

2.4.1 Low modulation index with low-gain approach

The optical intensity outputs acquired from the interferometers are converted in electrical voltage by a photodetector with a proportionality constant A, and by eliminating the DC component of (16) we obtain the output:

$$v(t) = AV\cos(\phi) \tag{30}$$

The AV factor can be determined experimentally by a self-calibration procedure, by providing $\sin(\Delta\phi) = 1$, i.e., assuming the argument $\Delta\phi = \pi/2$ rad, and assuming the spurious phase shift ϕ_0 is in the quadrature point ($\phi_0 = \pi/2$ rad) by applying the low-gain control for ϕ_0 compensation as discussed in Chapter 3. In this case, the voltage amplitude (30) becomes:

$$v_{cal} = -AV\cos(\Delta\phi + \phi_0) = -AV\cos(\pi) \tag{31}$$

A kind of such self-calibration procedure will be presented in details in Chapter 4. Alternatively, we can obtain the AV factor without the need of generating the argument $\Delta\phi = \pi/2$. In this approach, we force the output signal to vary, under open loop operation, by applying a specific external perturbation in one arm of the interferometer (e.g., mechanical vibration, temperature variation or a ramp signal) which obliges the multifringe regime to occur and measure the maximum (V_{max}) and minimum (V_{min}) values that the output signal can assume. In this case, we can obtain the AV factor as follows:

$$v_{cal} = AV = \frac{V_{max} - V_{min}}{2} \tag{32}$$

Thus, after the self-calibration procedure to obtain the AV factor, the voltage becomes:

$$v(t) = v_{cal}\sin(\Delta\phi) \tag{33}$$

If $\Delta\phi(t) < \frac{\pi}{2}$ rad (peak values):

$$\Delta\phi(t) = \sin^{-1}(v(t)/v_{cal}) \tag{34}$$

For low modulation index, $\Delta\phi(t) \ll \pi/2$ rad, $\sin(\Delta\phi(t)) \approx \Delta\phi(t)$ in (33), and the signal of interest become (under condition $\phi_0 = \pi/2$ rad):

$$\Delta\phi(t) = \frac{v(t)}{v_{cal}} \tag{35}$$

Considering (14) to convert the phase variation in mechanical displacement variation, we obtain:

$$\Delta l = \frac{\lambda}{4\pi}\Delta\phi(t) \tag{36}$$

2.4.2 High modulation index with modified high-gain approach

In this section, we present a modified high-gain approach, in which both the signal of interest, $\Delta\phi$, and the static phase shift, ϕ_0, are compensated by the controller, as will be shown in Chapter 3. This approach offers many advantages. For instance, it presents a much greater linear dynamic range for amplitude, good performance under noise, no need for calibration process nor demodulation methods.

On the other hand, unlike the high-gain approach presented in Udd and Spillman (2011), in this system there is no filtering process to separate the signals of interest and perturbations due to the frequency range of interest. In this case, we are interested in signals with frequencies below 20 Hz and amplitudes above $\frac{\pi}{2}$ rad, and a large amount of tests with statistical average were performed and repeatability was used to guarantee the quality of the results under the environmental perturbations. Besides that, the interferometer was used in a low spurious disturbance environment.

Assuming that the signals $\Delta\phi$ and ϕ_0 are fully compensated and the interferometer is in quadrature condition, that is:

$$\phi = \Delta\phi + \phi_0 - \phi_c = \pi/2 \tag{37}$$

thus, (30) can be written as:

$$v(t) = AV\cos(\Delta\phi + \phi_0 - \phi_c) \tag{38}$$

with $\phi_c = \Delta\phi + \phi_0 - \pi/2$ being the feedback signal.

Therefore, the output voltage signal $v(t)$ is zero at the quadrature point, and the feedback phase signal, that contains the signal of interest, is given by:

$$\phi_c = G_{AMP} G_{PZT_{fb}} v_{fb} \tag{39}$$

where G_{AMP} is the linear amplifier gain in [V/V], $G_{PZT_{fb}}$ is the feedback piezoelectric actuator gain [rad/V] and v_{fb} is the feedback voltage signal, as will be detailed in Chapter 3. One can conclude that the signal of interest $\Delta\phi$ is present and varies linearly with the feedback voltage, considering the feedback piezoelectric actuators working in its linear region.

However, it is important to consider the frequency range to apply this technique, because the control system must have a sufficient gain to fully compensate the signal of interest, and the higher the frequency of the signal of the interest the greater the gain (especially when compared to low-gain approach (UDD; SPILLMAN, 2011)), which heavily restricts the dynamic range for frequency. Moreover, it is important to know the exact value of $G_{PZT_{fb}}$ to obtain ϕ_c.

3 Variable structure and sliding modes non-linear control applied to two beam interferometers

In this chapter, we present the mathematical model of the proposed nonlinear control to stabilize the interferometric system, and the system's stability analysis. Computational simulations are performed, based on the mathematical model of the interferometer.

3.1 System modeling

The control technique used to stabilize the interferometric system is called Variable Structure and Sliding Modes control (DECARLO; ZAK; MATTHEWS, 1988; UTKIN, 1978), which is characterized by the use of a sign function to feed the system through a switching surface, in which the system is not affected by the presence of matched uncertainties, implying that the uncertainties exist in the same channel as that of the control input. This control technique uses a discontinuous and consequently a nonlinear structure, and its application is strongly justified in the control of nonlinear systems, such as the interferometer. The advantages of using this technique is the ease of implementation and powerful ability to reject disturbances and plant uncertainties (robustness).

The block diagram of the closed loop system is shown in Fig. 4. This is a second order system since it comprises a low pass filter (LPF) and an integrator. The low-pass filter allows the compensation of low frequencies (bellow 20 Hz) components of v because of the spurious signal ϕ_0 occurs in low frequencies, mentioned in Chapter 2. On the other hand, the signal of interest remains unaltered in higher frequencies (above 20 Hz), in most of the applications of this work.

In Fig. 4, γ is the total feedback gain, LPF is a first order Butterworth low pass filter with cutoff frequency $f_c = 20$ Hz and transfer function $H(s) = \frac{W(s)}{V(s)} = \frac{1}{(1+\tau s)}$, where s is the Laplace transform variable and $\tau = \frac{1}{2\pi f_c} = \frac{1}{40\pi}$ seconds. The function sgn$(-)$ operates as follows:

$$\text{sgn}(e) = \begin{cases} 1 & \text{if } e > 0, \\ 0 & \text{if } e = 0, \\ -1 & \text{if } e < 0. \end{cases} \tag{40}$$

To illustrate the proposed control operation, the block diagram shown in Fig. 4 is initially assumed to operate without the low pass filter (LPF), resulting in a first order

Figure 4 – Block diagram of the proposed closed loop system.

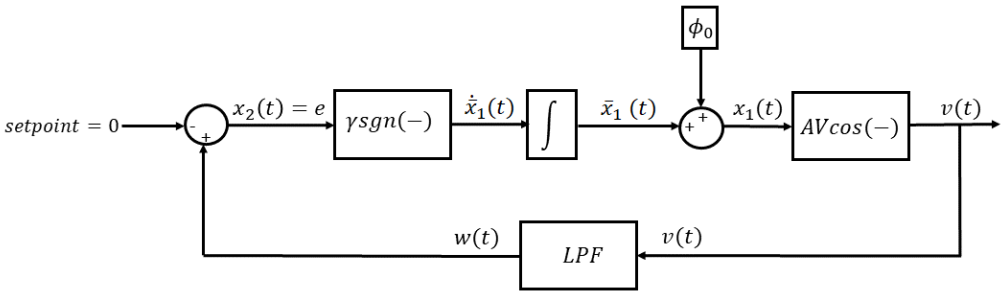

Source: From author.

system, as shown in Fig. 5.

Figure 5 – Simplified block diagram.

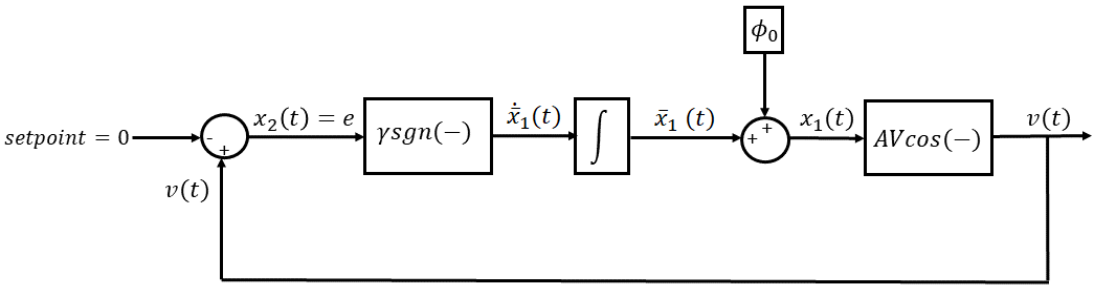

Source: From author.

Considering (41), we can design the block diagram shown in Fig. 6, where $\phi_0(0)$ is an initial condition of $\phi_0(t)$, such that:

$$\int_0^t \dot{\phi}_0(t)dt = \phi_0(t) - \phi_0(0) \tag{41}$$

Figure 6 – Modified block diagram.

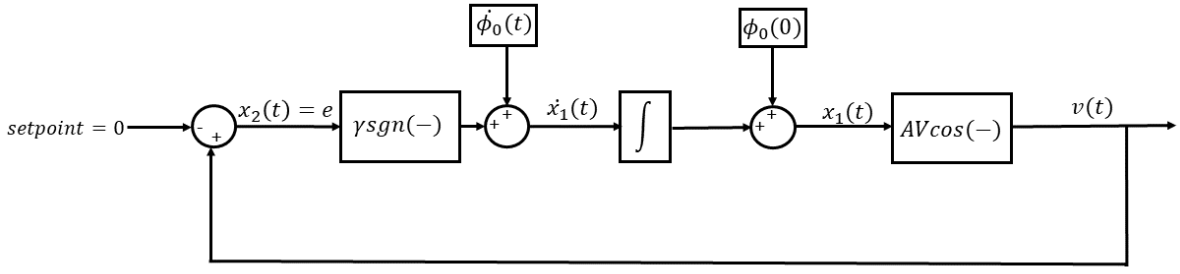

Source: From author.

From Figs. 5 and 6 and considering $\gamma > |\dot{\phi}_0|$ for $t \geq 0$, we can describe the variation rate of the state variable x_1 as follows:

$$\dot{x}_1 = \gamma \text{sgn}[AV\cos(x_1)] + \dot{\phi}_0 = \begin{cases} \gamma + \dot{\phi}_0 > 0 & \text{if } \cos(x_1) > 0, \\ \gamma + \dot{\phi}_0 < 0 & \text{if } \cos(x_1) < 0, \\ \dot{\phi}_0 & \text{if } \cos(x_1) = 0. \end{cases} \tag{42}$$

Regarding (42), we can generate the first order phase-plane shown in Fig. 7, where the direction of motion is determined by the sign of $v(t)$ for $\gamma > |\dot{\phi}_0|$.

Figure 7 – First order phase plane for $\gamma > |\dot{\phi}_0|$.

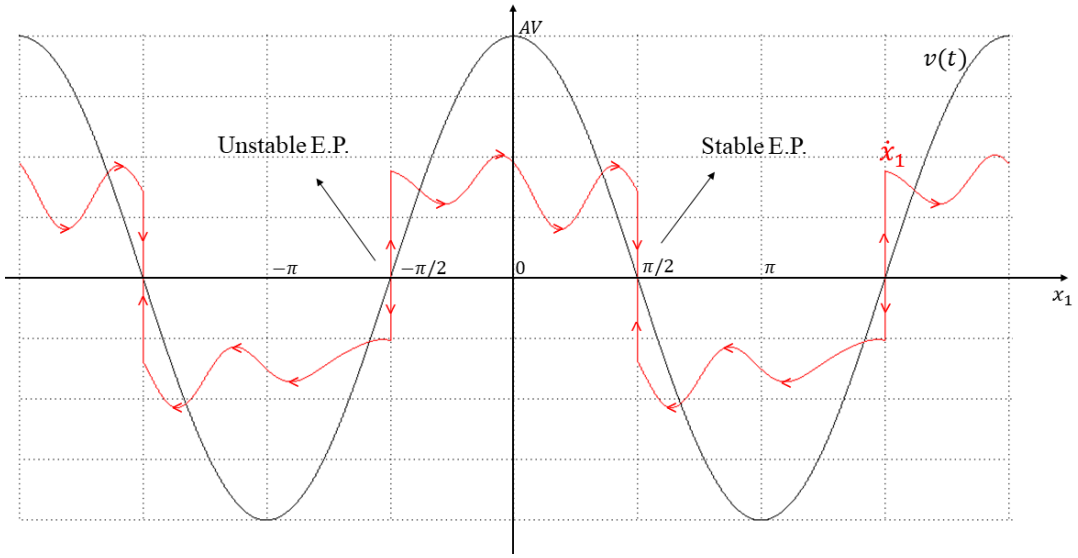

Source: From author.

For instance, consider that γ and AV are both positive. Starting the control system with an initial condition $0 \leq x_1(t) < \pi/2$, an error $e > 0$ ($\cos(x_1) > 0$ or $v(t) > 0$) will lead the function $\text{sgn}(e)$ to switch to a positive value, making $\dot{x}_1(t) = \gamma + \dot{\phi}_0$ positive, and leading the integrator output (x_1) to increase, causing to x_1 to go to the right in Fig. 7, when $v(t) > 0$. Consequently, $v(t)$ will decrease, bringing the error to zero ($e = 0$) and the output signal $v(t) = AV\cos(\phi_0 + x_1(t))$ to the condition of phase quadrature (stable equilibrium point (E.P.) in Fig. 7). If the initial error is $e < 0$ ($\cos(x_1) < 0$ or $v(t) < 0$), for $\pi < x_1(t) \pm 0$ for example, then the function $\text{sgn}(e)$ will switch to a negative value, making $\dot{x}_1(t) = \gamma + \dot{\phi}_0$ negative, and leading x_1 to decrease and goes to the left in Fig. 7, when $v(t) < 0$. Consequently, $v(t)$ will increase, bringing again the error to zero ($e = 0$). Besides that, the higher the γ gain value, the higher the variation rate of the integrator and, hence, the faster the system will reach the setpoint.

It is important to note from Fig. 7 that, if $\gamma < |\dot{\phi}_0|$ the disturbance will affect the state variable x_1 increasing rate, which can lead the system to instability as illustrated in

Fig. 8. The complete stability analysis will be performed in this chapter, and this specific situation will be seen in the next section.

Figure 8 – First order phase plane for $\gamma < |\dot{\phi}_0|$.

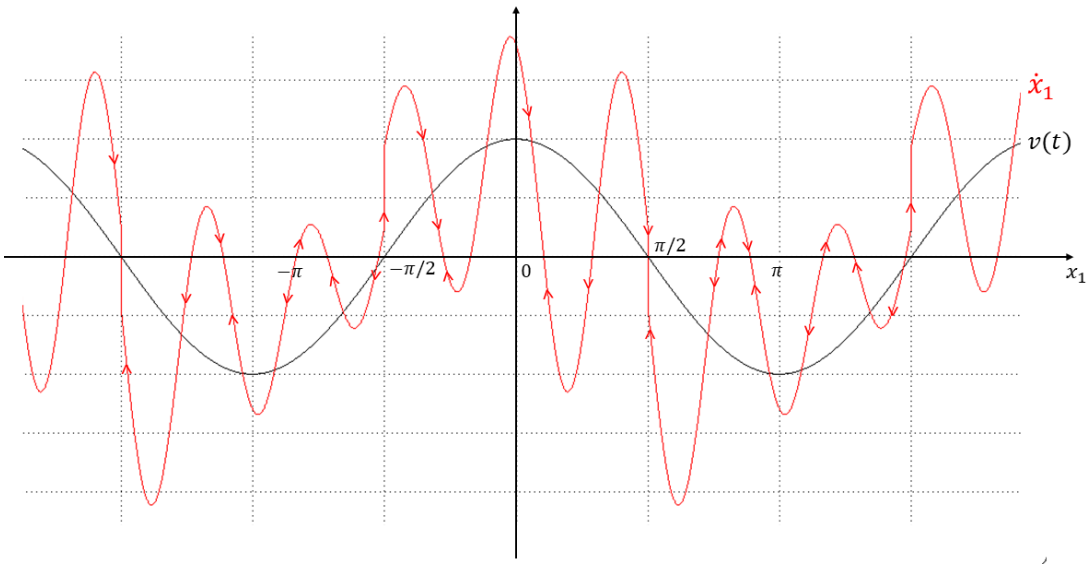

Source: From author.

Also, if $AV\cos(x_1) = 0$, the control is not acting on the system because the error is zero, and $\dot{x}_1 = \dot{\phi}_0$ from (42). In this case, the variation rate of x_1 is affected only by $\dot{\phi}_0$. However, in the moment that the error becomes different from zero, the control starts to actuate, taking the system to the equilibrium point, and leading the error to zero again. This effect will cause an oscillation around the equilibrium point known as chattering, discussed in Section 3.3.4.

3.2 State-Space Representation

To describe the closed loop system in the state-space representation, the block diagram shown in Fig. 4 was modified considering (41), and we can design the block diagram shown in Fig. 9.

Regarding the low-pass filter transfer function and making $w(t) = x_2(t)$, with $setpoint = 0$, we obtain:

$$X_2(s)(1 + \tau s) = V(s) \tag{43}$$

Applying the inverse Laplace transform in (43), we obtain:

$$x_2(t) + \tau\dot{x}_2(t) = v(t) \tag{44}$$

Figure 9 – Block diagram used in the system analysis.

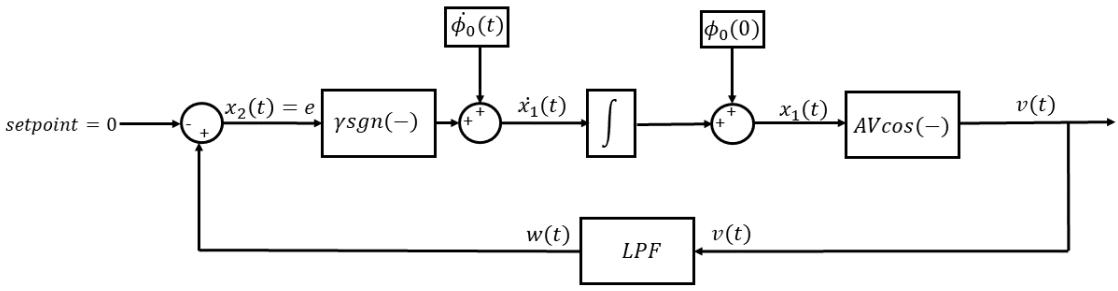

Source: From author.

Therefore, using the block diagram shown in Fig. 9 and (44), the state equations that represent the interferometric system are the following:

$$\dot{x}_1(t) = \gamma \text{sgn}(x_2) + \dot{\phi}_0, \gamma > 0 \tag{45}$$

and

$$\dot{x}_2(t) = \frac{AV}{\tau}\cos(x_1) - \frac{x_2}{\tau}, AV, \tau > 0 \tag{46}$$

where x_1 and x_2 are the system state variables. As can be seen in Martin et al. (2017a), from (45), the control condition is given by:

$$\gamma > |\dot{\phi}_0| \tag{47}$$

The control condition implies that $\text{sgn}(\dot{x}_1) = \text{sgn}[\gamma \text{sgn}(x_2) + \dot{\phi}_0] = \text{sgn}(x_2)$. Thus, $\dot{x}_1$ depends only on x_2 and the disturbance does not affect the x_1 increasing rate. It should be noted that, the higher the gain γ of the system, the faster the state x_1 converge to the equilibrium point, and more robust will be the system. Consequently, the overshoot will be greater and the settling time, shorter.

From the state equations and the control condition, the system equilibrium points are given by:

$$\dot{x}_1 = 0 \rightarrow \text{sgn}(x_2) = 0 \rightarrow x_2 = 0 \tag{48}$$

and

$$\dot{x}_2 = 0, x_2 = 0 \rightarrow AV\cos(x_1) = 0 \rightarrow x_1 = k\frac{\pi}{2} \tag{49}$$

for $k \in [\ldots, -3, -1, 1, 3, \ldots]$.

In the next sections, the convergence of the system to the equilibrium point $(x_1 = k\pi/2, x_2 = 0)$ will be evaluated.

3.3 Stability study

3.3.1 Lyapunov analysis of the linearized system

The Lyapunov's linearization method allows the evaluation of the local stability of a nonlinear system. Therefore, if an equilibrium point of the linearized system is strictly stable, then this point (and around it) are locally asymptotically stable for that particular nonlinear system (SLOTINE; LI et al., 1991).

The stability around the origin (the steady state point) will then be studied choosing a specific equilibrium point ($x_1^* = \pi/2, x_2^* = 0$) that will be defined as the new origin of the state-space. In this way, we perform the following change of variables:

$$y_1 = x_1 - x_1^* = x_1 - \frac{\pi}{2} \tag{50}$$

and

$$y_2 = x_2 - x_2^* = x_2 \tag{51}$$

where x_i^* is the state x_i at the equilibrium point for $i = 1, 2$. Based on (45) and (46), the system is now described by the state equations:

$$\dot{y_1} = \gamma \text{sgn}(y_2) = f_1(y_1, y_2) \tag{52}$$

and

$$\dot{y_2} = \frac{AV}{\tau} \cos\left(y_1 + \frac{\pi}{2}\right) - \frac{y_2}{\tau} = -\frac{AV}{\tau} \sin(y_1) - \frac{y_2}{\tau} = f_2(y_1, y_2) \tag{53}$$

From (52) and (53) and the control condition, the equilibrium points of the system are:

$$\dot{y_1} = 0 \rightarrow \gamma \text{sgn}(y_2) = 0 \rightarrow y_2 = 0 \tag{54}$$

and

$$\dot{y_2} = 0 \rightarrow \sin(y_1) = 0 \rightarrow y_1 = k\pi \tag{55}$$

for $k \in [\dots, -2, -1, 0, 1, 2, \dots]$.

For the system linearization, the sign function is approximated by a sigmoid function given by $\dot{y_1} = \gamma \text{sgm}(y_2) = \gamma y_2/(|y_2| + \epsilon)$, where $\epsilon > 0$ is sufficiently small. Thus, the linearization around the state variables given by (54) and (55) (SLOTINE; LI et al., 1991), for an even k, is given by:

$$\begin{bmatrix} \Delta\dot{y}_1 \\ \Delta\dot{y}_2 \end{bmatrix} = \begin{bmatrix} \frac{\partial f_1}{\partial y_1} & \frac{\partial f_1}{\partial y_2} \\ \frac{\partial f_2}{\partial y_1} & \frac{\partial f_2}{\partial y_2} \end{bmatrix}_{\substack{y_1 = k\pi \\ y_2 = 0}} \begin{bmatrix} \Delta y_1 \\ \Delta y_2 \end{bmatrix} = D_{2\times 2} \begin{bmatrix} \Delta y_1 \\ \Delta y_2 \end{bmatrix} = \begin{bmatrix} 0 & \frac{\gamma}{\epsilon} \\ -\frac{AV}{\tau} & -\frac{1}{\tau} \end{bmatrix} \begin{bmatrix} \Delta y_1 \\ \Delta y_2 \end{bmatrix} \tag{56}$$

The eigenvalues s of matrix D are given by $\{\det(sI_d - D) = 0, s \in \mathbb{C}\}$, where I_d is the identity matrix, and correspond to the closed loop poles of the linearized system. For this case, the determinant results is:

$$det(sI_d - D) = s^2 + \frac{1}{\tau}s + \frac{AV\gamma}{\tau\epsilon} = 0 \tag{57}$$

for τ, ϵ, γ and AV positives.

Therefore, the system poles are given by:

$$p_{1,2} = -\frac{1}{2\tau} \pm \frac{1}{2}j\sqrt{\left(\frac{4AV\gamma}{\tau\epsilon}\right) - \left(\frac{1}{\tau^2}\right)} \tag{58}$$

which can be rewritten as:

$$p_{1,2} = -\frac{1}{2\tau} \pm j\left[\frac{1}{2}\left(\sqrt{\frac{4AV\gamma}{\tau\epsilon}}\right)\left(\sqrt{1 - \frac{\epsilon}{4\tau AV\gamma}}\right)\right] \tag{59}$$

The dynamic equation for a second order system is given by (OGATA; SEVERO, 1998):

$$p = -\xi\omega_n \pm j\omega_n\sqrt{1 - \xi^2} \tag{60}$$

where ω_n is the undamped natural frequency and ξ is the damping ratio.

Therefore, the undamped natural frequency and the damping ratio can be rewritten as:

$$\omega_n = \sqrt{\frac{AV\gamma}{\tau\epsilon}} \tag{61}$$

and

$$\xi = \sqrt{\frac{\epsilon}{4\tau AV\gamma}} \tag{62}$$

One can observe by (59) that, if we decrease the time constant τ, the real component of the pole will be even more negative, moving away the poles from the imaginary axis. Therefore, the system dynamic will be faster, decreasing the settling and rise times due the expressions of ω_n and ξ in (61) and (62), respectively. Also, the control signal will be faster and can follow these variations.

Besides that, if the AV factor increases with the constant τ, then, the rising time will decrease. However, the overshoot percentage will be greater, increasing the oscillation in the system response. If we have a small AV factor, the rising time will be greater, so if we have a disturbance ϕ_0 faster than the rise time, then the control will not be able to suppress this disturbance. Therefore, to overcome this problem it is necessary to increase

the gain γ. It can be observed by (59), if the AV factor decreases, the gain γ must increase in order to maintain the dynamic characteristic of the system described by (60).

Considering that $\tau = 1/40\pi$ seconds, $\epsilon = 0.01$,$\gamma = 54$ rad (experimental values) and $AV = 1$ V (set as 1 V in this analysis, without loss of generality), the poles for k even are $s_{1,2} = (-63 \pm j821)$ which, according to Slotine, Li et al. (1991), correspond to a stable focus, i.e., this equilibrium point is strictly stable. Then, the nonlinear system is locally asymptotically stable. Similarly, for k odd, we obtain the poles $s_1 = -889$ and $s_2 = 763$, which correspond to a saddle point (SLOTINE; LI et al., 1991). Thus, these equilibrium points are unstable (MARTIN et al., 2017a). Besides that, being D a constant, with real elements and nonsingular matrix, a necessary and sufficient condition to the equilibrium point $y_1 = k\pi$ and $y_2 = 0$, for k even, to be strictly stable is that, for any symmetric positive definite matrix Q, there exists an unique symmetric matrix P positive definite, solution for the Lyapunov equation in (63) (SLOTINE; LI et al., 1991):

$$D^T P + PD = -Q \tag{63}$$

for Q a symmetric positive definite matrix.

Substituting the D values in (65) and making $Q = I_d$, where I_d is the identity matrix, we obtain:

$$\begin{bmatrix} 0 & -\frac{AV}{\tau} \\ \frac{\gamma}{\epsilon} & -\frac{1}{\tau} \end{bmatrix} \begin{bmatrix} p_{11} & p_{12} \\ p_{12} & p_{22} \end{bmatrix} + \begin{bmatrix} p_{11} & p_{12} \\ p_{12} & p_{22} \end{bmatrix} \begin{bmatrix} 0 & \frac{\gamma}{\epsilon} \\ -\frac{AV}{\tau} & -\frac{1}{\tau} \end{bmatrix} = - \begin{bmatrix} 1 & 0 \\ 0 & 1 \end{bmatrix} \tag{64}$$

Thus, the P matrix is given by:

$$P = \begin{bmatrix} \frac{\epsilon AV}{2\gamma} + \frac{\epsilon}{2AV\gamma} + \frac{\tau}{2} & \frac{\tau}{2AV} \\ \frac{\tau}{2AV} & \frac{\tau}{2} + \frac{\tau^2\gamma}{2\epsilon AV} \end{bmatrix} \tag{65}$$

Applying the Sylvester's theorem (SLOTINE; LI et al., 1991), we obtain $p_{11} = \left(\frac{\epsilon AV}{2\gamma} + \frac{\epsilon}{2AV\gamma} + \frac{\tau}{2}\right) > 0$ and $det(P) > 0$. Thus, P is a positive definite matrix and the linearized system is strictly stable. Therefore, the linear approximation is only locally stable while the nonlinear system is globally asymptotically stable, as we shall see in Sections 3.3.3 and 3.3.5.

3.3.2 First Harmonic Method

In this section, we apply the first harmonic method (SLOTINE; LI et al., 1991) to analyze the error applied by the nonlinear control system to the interferometric output. This method is based on expanding the nonlinear and discontinuous function in coefficients of Fourier series.

To proceed with this analysis, we make the consideration that $s = j\omega$. Then, we assume that the system is operating in steady state and close to the equilibrium point, in $x_1 = \pi/2$ rad, and with $\phi_0 = 0$, conditions achieved by the control condition described in (47). Consider that the input of the system is $\Delta\phi(t) = \Delta x_1 = B\sin(\omega t)$, and the low pass filter (LPF) in Fig. 4 has the transfer function:

$$\frac{W(j\omega)}{V(j\omega)} = \frac{1}{\tau j\omega + 1} \tag{66}$$

If the amplitude of the input signal (B) is sufficiently small and the system is linearized around the equilibrium point $x_1 = \pi/2$ rad, then the system output for $\Delta x_1 \ll 1$ can be given by:

$$v = AV\cos(\pi/2 + \Delta x_1) = -AV\sin(\Delta x_1) \approx -AV\Delta x_1 \tag{67}$$

Consider the block $\gamma\text{sgn}(-)$ in Fig. 4 with an input given by a sinusoidal wave described by $e = x_2 = \tilde{A}\sin(\omega t + \alpha_{fh})$, where $\tilde{A} > 0$ is the amplitude, ω is the angular frequency and α_{fh} is the variable that adds a degree of freedom in the final steps of the first harmonic analysis and will be used to find the error in feedback loop.

The output signal will then be a square wave with frequency equal to the input signal. The output of the block $\gamma\text{sgn}(-)$ can be expanded in Fourier series as follows, and we can disregard the phase (α_{fh}) without loss of generality:

$$\dot{\bar{x}}_1 = a_0 + \sum_{n=1}^{\infty} a_n\cos(n\omega t) + b_n\sin(n\omega t) \tag{68}$$

where:

$$a_n = \frac{1}{\pi}\int_0^{2\pi} \dot{\bar{x}}_1\cos(n\omega t)d(\omega t) \tag{69}$$

and

$$b_n = \frac{1}{\pi}\int_0^{2\pi} \dot{\bar{x}}_1\sin(n\omega t)d(\omega t) \tag{70}$$

The a_0 coefficient was suppressed, since the sign function is assumed as being symmetric and periodic. Also, the sign function is given by $\dot{\bar{x}}_1 = \gamma\text{sgn}(e)$. Then, the $\dot{\bar{x}}_1$ output is described as follows:

$$\dot{\bar{x}}_1 = \gamma\text{sgn}(e) = \gamma\text{sgn}[\tilde{A}\sin(\omega t)] = \begin{cases} +\gamma, \omega t \in [0, \pi)\,, \\ -\gamma, \omega t \in [\pi, 2\pi) \end{cases} \tag{71}$$

Thus, the first harmonic output coefficients are given by:

$$a_1 = \frac{1}{\pi}\int_0^{2\pi} \gamma \text{sgn}\left(\tilde{A}\sin(\omega t)\right)\cos(\omega t)\, d\omega t \tag{72}$$

Rewriting:

$$a_1 = \frac{1}{\pi}\int_0^{\pi} \gamma\cos(\omega t)\, d\omega t + \frac{1}{\pi}\int_{\pi}^{2\pi} (-\gamma)\cos(\omega t)\, d\omega t = 0 \tag{73}$$

For the b_1 coefficient:

$$b_1 = \frac{1}{\pi}\int_0^{2\pi} \gamma \text{sgn}\left(\tilde{A}\sin(\omega t)\right)\sin(\omega t)\, d\omega t \Rightarrow \tag{74}$$

$$b_1 = \frac{1}{\pi}\int_0^{\pi} \gamma\sin(\omega t)\, d\omega t + \frac{1}{\pi}\int_{\pi}^{2\pi} -\gamma\sin(\omega t)\, d\omega t \Rightarrow \tag{75}$$

$$b_1 = \frac{2}{\pi}\int_0^{\pi} \gamma\sin(\omega t) d\omega t \Rightarrow \tag{76}$$

$$b_1 = \frac{2}{\pi}\gamma[-\cos(\omega t)]\Big|_0^{\pi} = \frac{2\gamma}{\pi}[-\cos(\pi) - (-\cos(0))] \Rightarrow \tag{77}$$

$$b_1 = \frac{4\gamma}{\pi} \tag{78}$$

Consequently, the output of the sign function block in terms of the first harmonic is $\dot{\bar{x}}_1 = \frac{4\gamma}{\pi}\sin(\omega t + \alpha_{fh})$. Therefore, a simplified block diagram is obtained, and an analysis using a sinusoidal input as input is performed, as shown in Fig. 10.

Figure 10 – Modified block diagram in terms of first harmonic.

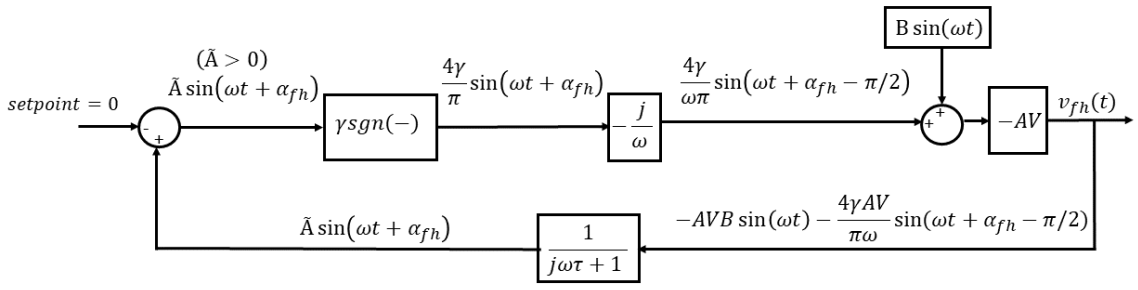

Source: From author.

One can observe that the signal after the integrator block $(-j/\omega)$ is $\overline{x}_1 = \left(\frac{4\gamma}{\pi\omega}\right)\sin\left(\omega t + \alpha_{fh} - \frac{\pi}{2}\right)$ and the interferometric output signal $(v_{fh}(t))$ is given by:

$$v_{fh}(t) = -AVB\sin(\omega t) - \frac{4\gamma AV}{\pi\omega}\sin(\omega t + \alpha_{fh} - \pi/2) \tag{79}$$

$$v_{fh}(t) = -AVB\sin(\omega t) + \frac{4\gamma AV}{\pi\omega}\sin(\omega t + \alpha_{fh} + \pi/2) \tag{80}$$

Besides that, the output can be rewritten considering the LPF block as follows:

$$-\frac{AVB}{\sqrt{(\tau\omega)^2+1}}\sin(\omega t - \tan^{-1}(\tau\omega)) + \frac{4\gamma AV}{\pi\omega\sqrt{(\tau\omega)^2+1}}\sin\left(\omega t + \alpha_{fh} - \tan^{-1}(\tau\omega) + \frac{\pi}{2}\right) = \tilde{A}\sin(\omega t + \alpha_{fh}) \tag{81}$$

In this work, it was assumed that the operation frequency of the signal of interest is much greater than the cutoff frequency of the low-pass filter ($\omega\tau \gg 1$), in order suppress only the ϕ_0 component in low-gain approach, as shown in Section 2.4.1. In this case, $\frac{1}{\sqrt{(\tau\omega)^2+1}} \cong \frac{1}{\tau\omega}$ and $-\tan^{-1}(\tau\omega) \cong -\frac{\pi}{2}$, then, (81) can be rewritten as follows:

$$-AVB\sin\left(\omega t - \frac{\pi}{2}\right) + \frac{4\gamma AV}{\pi\omega}\sin(\omega t + \alpha_{fh}) = \frac{\tilde{A}}{(\tau\omega)^{-1}}\sin(\omega t + \alpha_{fh}) \tag{82}$$

Considering $B > \frac{4\gamma}{\pi\omega}$, the solution for α_{fh} occurs when $\alpha_{fh1} = -\frac{\pi}{2} + 2k\pi$ and for $\alpha_{fh2} = \frac{\pi}{2} + 2k\pi$ for $k \in \mathbb{Z}$ and, consequently, $\tilde{A}_1 = -\frac{AV}{\omega\tau}\left(B - \frac{4\gamma}{\pi\omega}\right)$ and $\tilde{A}_2 = \frac{AV}{\omega\tau}\left(B + \frac{4\gamma}{\pi\omega}\right)$. In these cases:

$$v_{fh1}(t) = \left(-AVB + \frac{4\gamma}{\pi\omega}AV\right)\sin(\omega t) \tag{83}$$

and

$$v_{fh2}(t) = \left(-AVB - \frac{4\gamma}{\pi\omega}AV\right)\sin(\omega t) \tag{84}$$

where $v_{fh1}(t)$ and $v_{fh2}(t)$ are the output signal in terms of voltage in the first harmonic method for the two solutions.

We observed from block diagram in Fig. 10 that the signal after the integrator can not have a phase constant $\alpha_{fh1} = -\frac{\pi}{2} + 2k\pi$ because this signal would be lead in time in relation with the input signal. Therefore, the remaining solution is $\alpha_{fh2} = \frac{\pi}{2} + 2k\pi$. Also, with the simulations we observed that the output signal with the feedback system differs from the input signal by a $\frac{4\gamma}{\pi\omega}$ positively, according to the (84) as will be seen.

Then, the approximated amplitude for the output will be $-AV\left[B+\frac{4\gamma}{\pi\omega}\right]$ which leads us to conclude that the error obtained by the first harmonic method is positive and is given by:

$$E_{FHM}=\frac{4\gamma}{\pi\omega} \tag{85}$$

Considering (85) one can observe that the error only depends of the feedback gain γ and the signal of interest frequency ω, which are well known parameters, and decreases as the signal frequency ω increases. It is important to note that, to correct the output signal in term of the error described in (85), we have to subtract the E_{FHM} of the $-\frac{v_{fh}}{AV}$ amplitude in radians.

In order to evaluate the error obtained by the first harmonic method, simulations were carried out using Simulink®. The output signal error in simulation (E_{SML}) was obtained using $\gamma = 157.5$ (practical value), with a signal of interest with peak voltage of 0.5 rad for different frequencies, as shown in Fig. 11 for 1 kHz frequency with the signal of interest (B) in red and the measured ($\frac{v_{fh}}{AV}$) in black.

Figure 11 – Error in output signal obtained by the simulation, with the signal of interest (B) in red and the measured ($\frac{v_{fh}}{AV}$) in black.

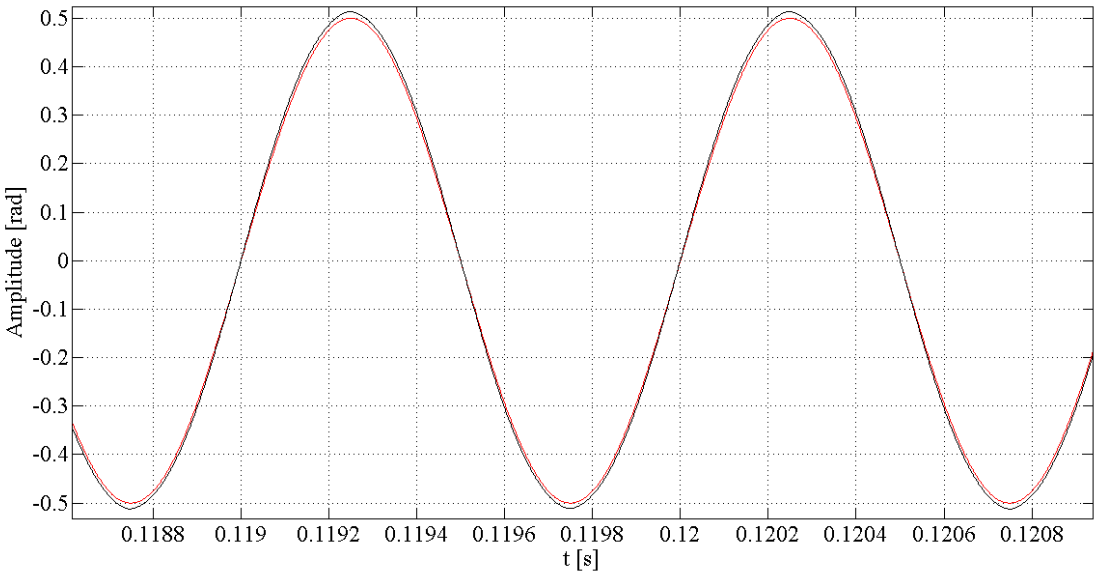

Source: From author.

The error for the first harmonic method (E_{FHM}) was calculated using (85) for the same gain and frequencies, and compared with the simulation (E_{SML}), as shown in Table 1.

Table 1 – Error with simulation and first harmonic method.

$Freq.[Hz]$	$E_{SML}[rad]$	$E_{FHM}[rad]$
500	0.0684	0.0638
750	0.0472	0.04255
1000	0.0328	0.03191
1250	0.0254	0.02553
1500	0.0204	0.02127
5000	0.0058	0.00638

It is important to point out that, the error simulation it was proved that it has the same value of the obtained by the first harmonic method, and only depends on feedback gain γ and the signal of interest frequency ω. According to Table 1, one can observe a good agreement between E_{SML} and E_{FHM}, and that the overall error in the closed-loop system decreases as the signal frequency increases, becoming negligible for frequencies above 5 kHz. Therefore, this is a very important result due to its application in the correction of the error in the output signal in practical system, as will be seen in this work, increasing the overall accuracy of the system.

3.3.3 Phase-plane

The phase plane is a graphical method that allows us to generate a two-dimensional plane in the state space and, inside this plane, to draw motion trajectories for different initial conditions. In this way, it is possible to obtain information about the stability, behavior of the states, among other dynamic patterns of the system.

Many advantages of this method can be presented. For instance, as a graphical method, it allows us to visualize what happens with the nonlinear system starting from different initial conditions, without analytically solving the nonlinear equations. Besides, it is not restricted to small or smooth nonlinearities, but it is applied equally well to strong nonlinearities and discontinuities (SLOTINE; LI et al., 1991).

Considering the dynamics described by (45) and (46), the isoclines method will now be used, which involves directly the elimination of the time variable, and then the resolution of this equation for a functional relation between x_1 and x_2 (SLOTINE; LI et al., 1991). At a point (x_1, x_2) in the phase plane, the slope of the tangent to the trajectory can be determined by (86). An isocline is defined as being the locus of the points with a given tangent slope. Considering the interferometer system given by (45) and (46), an isocline with slope α is thus defined as bellow:

$$\frac{\dot{x}_2}{\dot{x}_1} = \frac{\partial x_2}{\partial x_1} = \frac{AV\cos(x_1) - x_2}{\tau\gamma \text{sgn}(x_2)} = \alpha \tag{86}$$

where AV, τ and γ are given positives constants.

The phase portrait is generated obtaining a field of directions tangents to the trajectories. Then, phase plane trajectories are formed from the field of directions. In Table 2, the directions of tangents to the trajectories are shown for $0 < x_1 < \pi$.

Table 2 – The directions of tangents to the trajectories for $0 < x_1 < \pi$.

x_2	x_1	$AV\cos(x_1) - x_2$	α	$\dot{x}_1$	$\dot{x}_2$
> 0	$> \pi/2$	< 0	< 0	> 0	< 0
> 0	$< \pi/2$	> 0	> 0	> 0	> 0
> 0	$< \pi/2$	< 0	< 0	> 0	< 0
< 0	$< \pi/2$	> 0	< 0	< 0	> 0
< 0	$> \pi/2$	< 0	> 0	< 0	< 0
< 0	$> \pi/2$	> 0	< 0	< 0	> 0

Taking different values of directions of tangents in Table 2, a set of isoclines can be drawn, and a field of directions of tangents to trajectories are generated, as shown in Fig 12. The direction of motion is determined by the sign of $\dot{x}_{1,2}$ at that point. That is, when $\dot{x}_1 > 0$ then x_1 increases and moves to the right in the phase. Similarly, when $\dot{x}_1 < 0$, x_1 shifts to the left and for $\dot{x}_1 = 0$, x_1 becomes constant at this point. The same analysis can be done to $\dot{x}_2$.

From (86), we can observe that considering $AV\cos(x_1) - x_2 = 0$, we have $\alpha = 0$, and when $x_2 = 0$ and $x_1 \neq k\pi/2$ for $k \in \mathbb{Z}$, $\alpha \to \infty$. Thus, the phase plane has a null derivative when crosses the curve $x_2 = AV\cos(x_1)$ and it has an infinite derivative when crosses the x_1 axis. The signals for different values of α are marked in the figure. Also, it is important to note that the analysis for $x_1 = k\pi/2$ has already been performed and from the direction of motion of the arrows that, the stable focus predicted in Section 3.3.1 is clockwise.

3.3.3.1 *Convergence analysis from* $x_2(0) \neq 0$ *to* $x_2(t) = 0$

It is possible to see that, to an initial condition $x_2(0) > 0$ in the phase plane, there are two different possibilities of states trajectories in the phase plane. The first one is illustrated in blue in Fig. 13. In that case, $x_1(t_F) = x_1(0)$ and the phase plane trajectory decreases until it reaches the x_1 axis in $x_1(t_G)$ with $x_2(t_G) = 0$, without crossing the curve $x_2 = AV\cos(x_1)$. In this situation, x_2 converge to zero and, consequently, the system convergence to the equilibrium point is guaranteed, as shown in the next steps.

The second possibility is illustrated in red in Fig. 13. In this case, $x_1(t_I) = x_1(0)$ and the trajectory decreases in x_2, as seen in the analysis by the isoclines method, and crosses the curve $x_2 = AV\cos(x_1)$ at the point $x_1(t_D)$. Analyzing the direction of motion given by the arrows, the curve goes to the right and it goes up until crosses the curve $x_2 = AV\cos(x_1)$ again in $x_1(t_E)$. Then, assuming the worst case, in which the trajectory

Figure 12 – System phase plane obtained through the isoclines method.

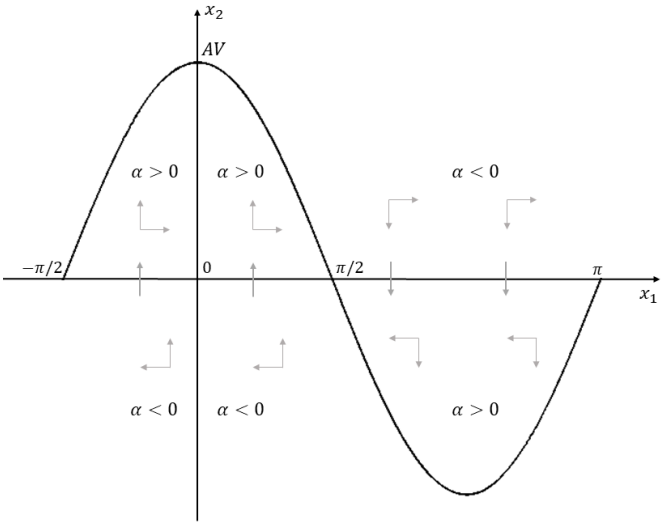

Source: From author.

decreases but continues to shift to the right: the curve crosses $x_2 = AV\cos(x_1)$ in $x_1(t_H)$, i.e., the curve does not converge to $x_2 = 0$, how we suppose in the first case ($x_1(0) = x_1(t_F)$).

Figure 13 – Trajectories in the phase plane.

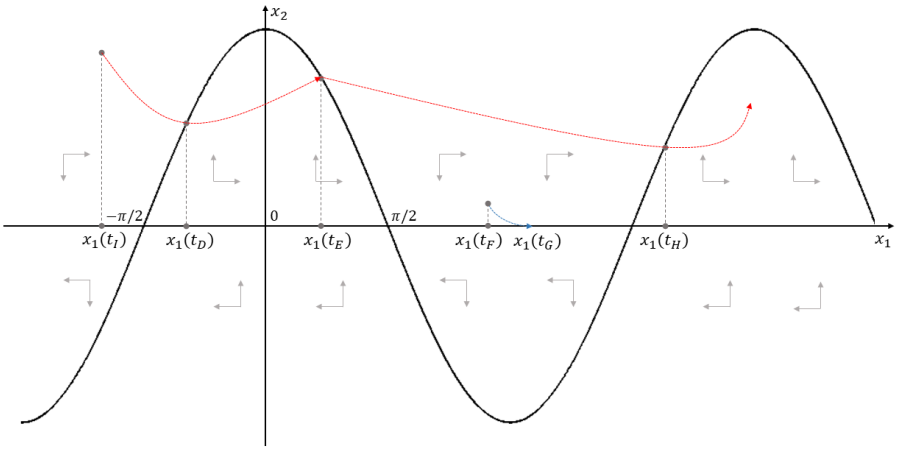

Source: From author.

Assuming $x_1(t_D)$ arbitrary, we will demonstrate now that $x_2(t_H) < x_2(t_D)$ each time that the trajectory crosses $x_2 = AV\cos(x_1)$, and the values of x_2 decreases successively until $x_2 = 0$.

From (86), we have:

$$\int_{x_1(t_D)}^{x_1(t_H)} \left(\frac{AV}{\tau} \cos(x_1) - \frac{x_2}{\tau} \right) dx_1 = \int_{x_2(t_D)}^{x_2(t_H)} \gamma \text{sgn}(x_2) dx_2 \tag{87}$$

Regarding Fig. 13, the trajectory remains in $x_2 > 0$ for $x_1(t_D) \leqslant x_1 \leqslant x_1(t_H)$, then $\text{sgn}(x_2) = 1$ in this range. Therefore,

$$\int_{x_2(t_D)}^{x_2(t_H)} \gamma \text{sgn}(x_2) dx_2 = \gamma(x_2(t_H) - x_2(t_D)) \tag{88}$$

Considering the integrals as the corresponding areas, according to Fig. 14, and $\tau > 0$, we have:

$$\int_{x_1(t_D)}^{x_1(t_H)} \left(\frac{AV}{\tau} \cos(x_1) - \frac{x_2}{\tau} \right) dx_1 = \frac{1}{\tau} \left(\int_{x_1(t_D)}^{x_1(t_E)} (AV \cos(x_1) - x_2)\, dx_1 + \int_{x_1(t_E)}^{x_1(t_H)} (AV \cos(x_1) - x_2)\, dx_1 \right) = \frac{1}{\tau}(Area_1 - Area_2) < 0 \tag{89}$$

Since, clearly from Fig. 14, $Area_2 > Area_1$.

Figure 14 – Comparative area analysis in the phase plane

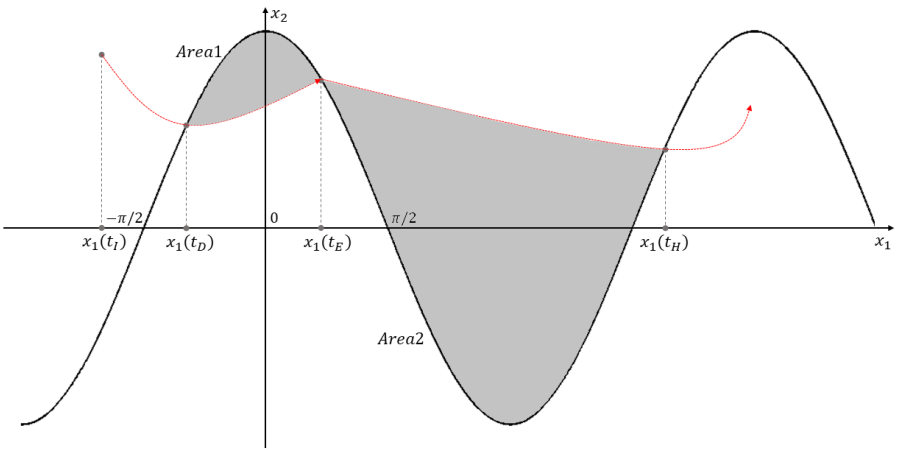

Source: From author.

Hence, from (88) and (89) for $\gamma > 0$, it follows that:

$$\gamma(x_2(t_H) - x_2(t_D)) < 0 \rightarrow x_2(t_H) - x_2(t_D) < 0 \tag{90}$$

Therefore,

$$x_2(t_H) < x_2(t_D) \tag{91}$$

One can observe by (91) that, when $t \to \infty$ the state x_2 converges to zero, what concludes the proof for this situation.

3.3.3.2 *Symmetry in the phase plane*

Finally, there is a need to analyze the case where $x_2(0) < 0$. To simplify this analysis, we will demonstrate the existence of a symmetry in the phase plane (SLOTINE; LI et al., 1991).

Considering the variables $z_1 = -x_1 + \pi$ and $z_2 = -x_2$, then, using (45) and (46) removing $\dot{\phi}_0$, one can rewrite the system as:

$$\dot{z}_1 = -\dot{x}_1 = -\gamma \text{sgn}(x_2) = -\gamma(-\text{sgn}(-x_2)) = \gamma \text{sgn}(z_2) \tag{92}$$

since $\text{sgn}(-x_2) = -\text{sgn}(x_2)$. And also,

$$\dot{z}_2 = -\dot{x}_2 = -\frac{AV}{\tau}\cos(x_1) + \frac{x_2}{\tau} = -\frac{AV}{\tau}\cos(-z_1 + \pi) - \frac{z_2}{\tau} \tag{93}$$

Now, $\cos(-z_1 + \pi) = -\cos(z_1)$, then,

$$\dot{z}_2 = \frac{AV}{\tau}\cos(z_1) - \frac{z_2}{\tau} \tag{94}$$

From (92) and (94), the resultant system is given by:

$$\dot{z}_1 = \gamma \text{sgn}(z_2) \tag{95}$$

and

$$\dot{z}_2 = \frac{AV}{\tau} cos(z_1) - \frac{z_2}{\tau} \tag{96}$$

One can observe by (95) and (96) that the resulting system has the same form from (45) and (46) removing $\dot{\phi}_0$, respectively, where the only exchanging is from $x_{1,2}$ to $z_{1,2}$. The new axes $z_{1,2}$ are superimposed on the original axes $x_{1,2}$ in Fig. 15.

Furthermore, the phase plane of the system is symmetric about the x_1 axis. Thus, it is possible to make a similar analysis to $x_2(0) < 0$, and one can conclude that $x_2(t)$ converge to zero.

Figure 15 – Symmetry in the phase plane.

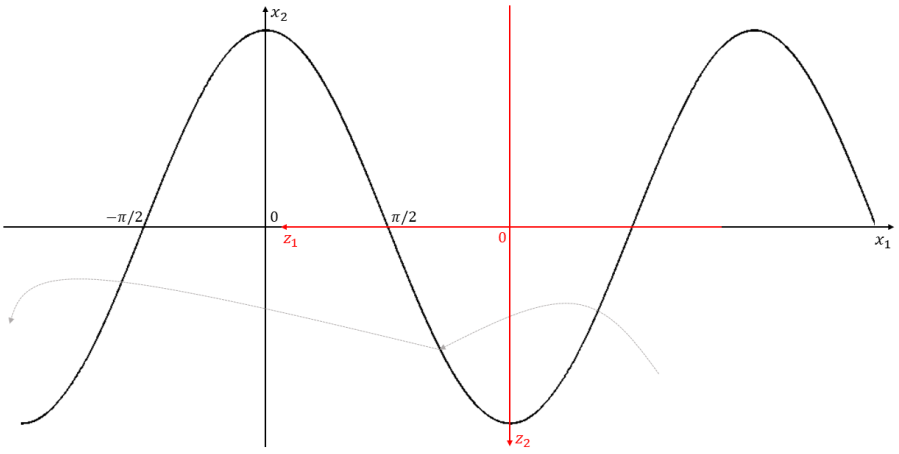

Source: From author.

3.3.3.3 *Convergence analysis from $x_2(t) = 0$ to the equilibrium point*

In the previous section, it was proved that the state $x_2(t)$ convergence to zero starting from any initial condition. Since the stable equilibrium points of the system correspond to a clockwise stable focus as seen in Section 3.3.1 and 3.3.3, we will verify, in this section, if the system state variables $x_1(t)$ and $x_2(t)$ go to the equilibrium point ($x_1 = k\pi/2, x_2 = 0$) from the following initial conditions: point A in $t = t_A = 0 \quad (x_1(t_A), x_2(t_A) = 0)$ and point B in $t = t_B = 0 \quad (x_1(t_B), x_2(t_B) = 0)$, shown in Fig. 16.

Figure 16 – Trajectories analysis from $x_2(t) = 0$ in the phase plane.

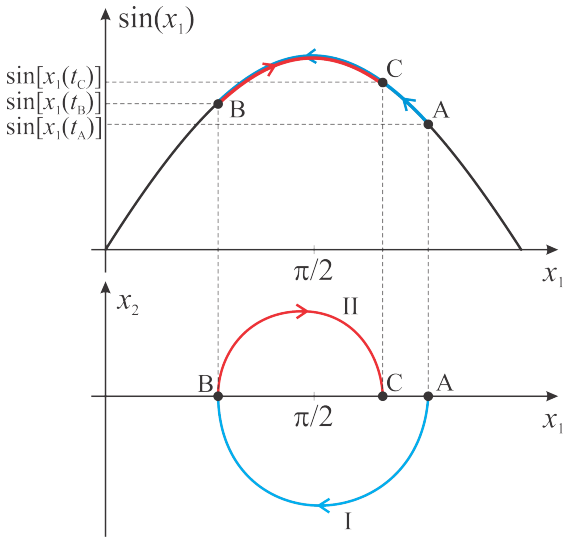

Source: From author.

For this case, we considered (45), (46) and (86) with the control condition described in (47), obtaining the following equation for trajectory I:

$$\int_{x_1(t_A)}^{x_1(t_B)} \left(\frac{AV}{\tau} \cos(x_1) - \frac{x_2}{\tau} \right) dx_1 = \int_{x_2(t_A)}^{x_2(t_B)} \gamma \text{sgn}(x_2) dx_2 \tag{97}$$

The term on the right side of (97) is null since $x_2(t_A) = x_2(t_B) = 0$ and the functions inside the integral depends only on x_2. Then, we can rewrite (97) as follows:

$$\int_{x_1(t_A)}^{x_1(t_B)} \frac{AV}{\tau} \cos(x_1) dx_1 = \int_{x_1(t_A)}^{x_1(t_B)} \frac{x_2}{\tau} dx_1 \tag{98}$$

The term on the right side of (98) corresponds to the area over the curve I, as shown in Fig. 16, which is positive for $x_2 < 0$. Thus, we can rewrite (98):

$$\frac{AV}{\tau} \left(\sin(x_1(t_B)) - \sin(x_1(t_A)) \right) = Area_I > 0 \tag{99}$$

Therefore, $\sin(x_1(t_B)) > \sin(x_1(t_A))$. On the same way, analyzing the trajectory II, from point B to point C in $t = t_C \quad (x_1(t_C), x_2(t_C) = 0)$, one can verify that $\sin(x_1(t_C)) > \sin(x_1(t_B))$. This means that the system approaches the equilibrium point, i.e., as time increases, $\sin(x_1(t))$ approaches 1 (x_1 approaches $\pi/2$), and the system does not tend to a limit cycle or to instability.

Regarding the conclusion obtained that $\sin(x_1(t_C)) > \sin(x_1(t_B))$, a second analysis about the convergence of x_1 to the equilibrium point can be done, as presented in Fig. 17, where $x_1(0) = a$ is the initial condition, and $x_1(t_f) = b$ is the next point of the state x_1.

Figure 17 – Convergence to the equilibrium point in the phase plane.

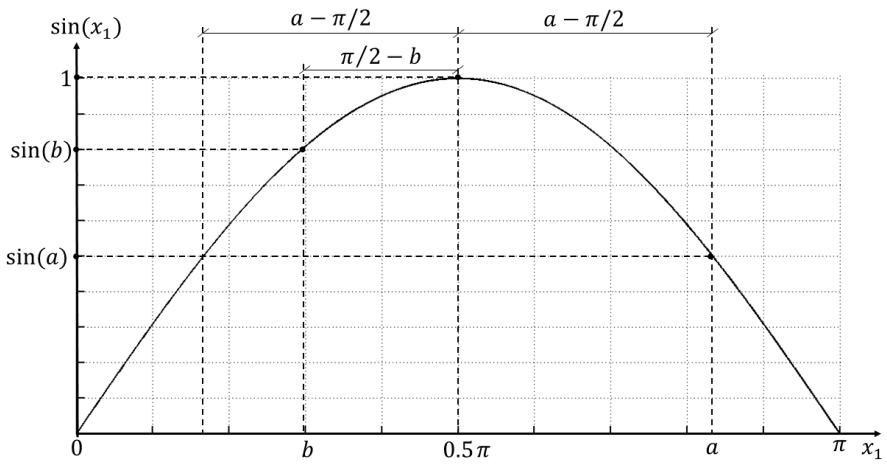

Source: From author.

First, we consider the hypotheses that $0 < a, b < \pi$, $\pi/2 < a < \pi$ and $0 < b < \pi/2$. Thus, if we consider $\sin(b) > \sin(a)$, we have $|b - \pi/2| < |a - \pi/2|$, therefore, the state x_1 approaches to $\pi/2$ and, consequently, the system approaches to the equilibrium point.

Proof: Due to the symmetry of the $\sin(x_1)$ with respect to $x_1 = \pi/2$, we can write:

$$\sin(a) = \sin(\pi/2 - (a - \pi/2)) = \sin(\pi - a) \tag{100}$$

One can observe that as $\pi/2 < a < \pi$, then $\pi - a \in (0, \pi/2)$. Therefore if $\sin(b) > \sin(a) = \sin(\pi - a) \rightarrow \sin(b) > \sin(\pi - a)$ and $\pi - a < b \rightarrow \pi/2 - b < a - \pi/2$, proving that the system approaches the equilibrium point.

3.3.3.4 *Phase Plane Simulation*

The phase-plane was obtained numerically, through the use of a program developed by the author using software MATLAB and the Runge-Kutta method, from (45) and (46), where the AV factor was obtained experimentally and the gain γ comprises the complete feedback loop gain, given by $\gamma = G_{\text{sgn}} G_{int} G_{AMP} G_{PZTfb}$, where G_{sgn} is the sign function gain, G_{int} is the integrator gain, G_{AMP} is the linear amplifier gain, and G_{PZTfb} is the feedback piezoelectric actuator gain. The linear amplifier (AMP) and the feedback piezoelectric actuator (PZT_{fb}) will be described in Section 4.

The simulation results are shown in Figs. 18 and 19, for several initial conditions x_0 at a circumference around the origin ($x_1 = 0$, $x_2 = 0$), according to $x_0 = r[\cos\theta \quad \sin\theta]^T$, where r is the circumference radius and $\theta \in \{0, \pi/32, 2\pi/32, \ldots, 2\pi\}$. All the trajectories inside the observation region converge to the point ($x_1 = \pi/2$, $x_2 = 0$) when time $t \rightarrow \infty$. For example, if the initial condition departs from point A, in Fig. 18(a), the solution will track the trajectory from the left to the right, mostly for $x_2 > 0$, towards the equilibrium point ($x_1 = \pi/2$, $x_2 = 0$). For an initial condition on point B, the solution will track the trajectory from the right to the left, mostly for $x_2 < 0$, towards the same equilibrium point. The point ($x_1 = \pi/2$, $x_2 = 0$) corresponds to a stable equilibrium point, according to state equation analysis. In Fig. 18(b) the two stable equilibrium points, ($x_1 = \pi/2$, $x_2 = 0$) and ($x_1 = -3\pi/2$, $x_2 = 0$) are visible, as well as an unstable equilibrium point in $x_1 = -\pi/2$, $x_2 = 0$. This behavior occurs due to the periodic and nonlinear characteristic of the interferometer, with infinite stable and unstable equilibrium points.

Besides that, computational simulations were carried out using the sigmoid approach with the parameters $\gamma = 1176\ rad/V$ and $\epsilon = 0.9$, obtaining the theoretical phase-plane shown in Figure 19. The parameter γ is the total feedback gain, which is composed of $G_{\text{sgm}} = 25\ V/V$, $G_{AMP} = 21\ V/V$ and $G_{PZT_{fb}} = 2.24\ rad/V$. More details of this approach will be seen in Section 3.3.4.

Figure 18 – Theoretical phase-plane for $\gamma = 54$ rad. (a) $x_o = r[(\cos\theta + (\pi/2r)) \quad \sin\theta]^T$. (b) $x_o = r[\cos\theta \quad \sin\theta]^T$.

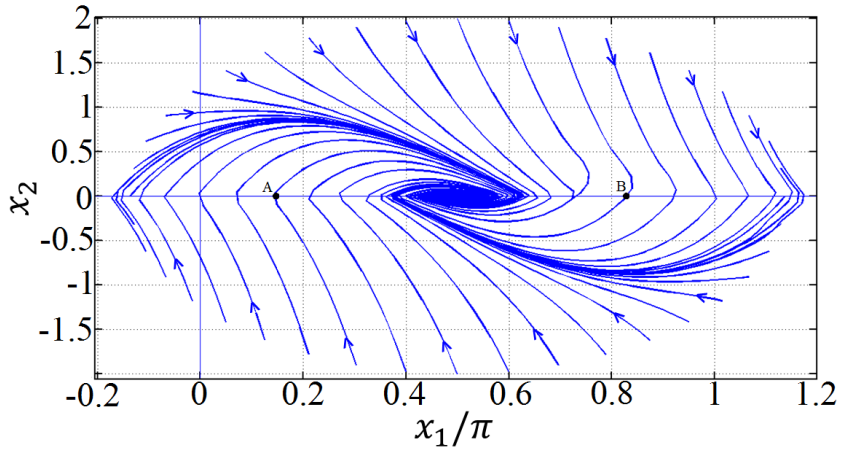

(a)

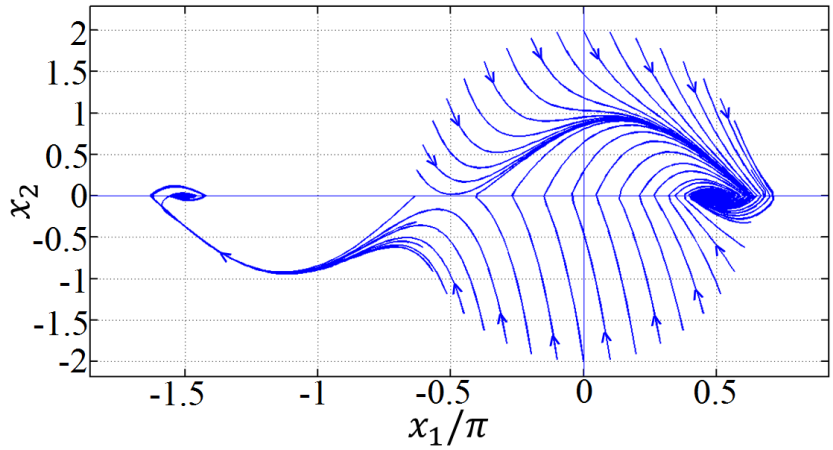

(b)

Source: From author.

In order to analyze the behavior of the system with the gain, the phase-plane was obtained for five different practical values of γ: $\gamma_1 = 5.01$, $\gamma_2 = 25.77$, $\gamma_3 = 320.69$, $\gamma_4 = 1176$ and $\gamma_5 = 2520$, as shown in Fig. 20. The values of the practical gains, G_{sgn}, G_{int}, G_{AMP} and G_{PZTfb}, used in each case, are shown in Table 3.

Table 3 – Practical gains used for the nonlinear control system.

γ	G_{sgn} or G_{sgm}	G_{amp}	G_{PZTfb}	G_{int}	type of function
5.01	15	21	0.035	0.4545	sign
25.77	15	21	0.18	0.4545	sign
320.69	15	21	2.24	0.4545	sign
1176	30	21	2.24	0.8333	sigmoid
2520	800	21	0.18	0.8333	sigmoid

For γ_4 and γ_5, the gain values are high, resulting in the occurrence of the chattering

Figure 19 – Theoretical phase plan for $\gamma = 1176\ rad/V$.

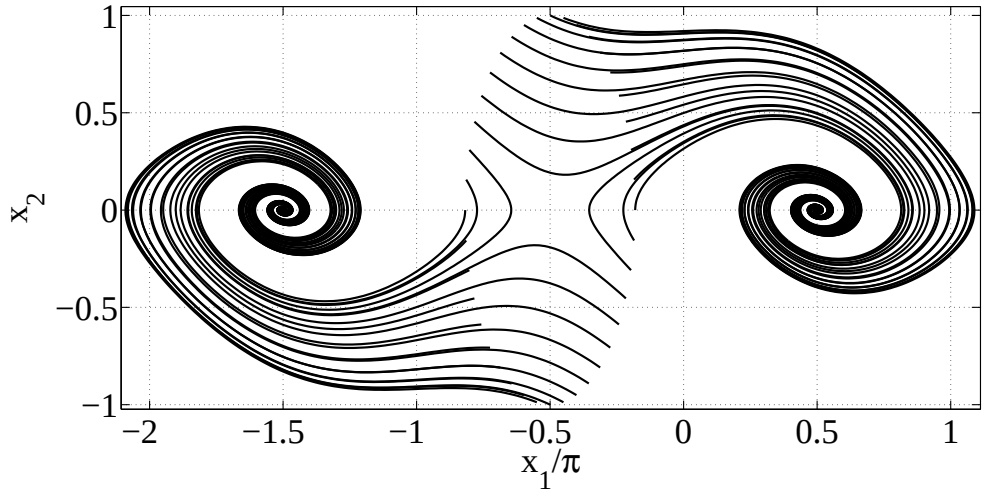

Source: From author.

problem, that will be shown in Section 3.3.4. To overcome this issue, a sigmoid function was chosen to be used instead of the sign function. The sigmoid function is given by $\text{sgm}(x_2) = x/(|x_2| + \epsilon)$, where $\epsilon > 0$ and sufficiently small. For γ_4 and γ_5 the values $\epsilon_4 = 0.9$ and $\epsilon_5 = 1.5$ were, respectively, used. The effect of using a sigmoid instead a sign function in the control system is shown in Fig. 20, and it will be presented in details in the next section.

As can be seen from Figs. 18 to 20, we evaluated a 2π region and, since the system is periodic, it always converges to a stable point, regardless the initial conditions. In addition, the system does not tend to a limit cycle nor to instability. Besides that, the higher the gain γ of the system, the faster the state x_1 converges to the equilibrium point, and more robust the system will be. Consequently, the overshoot will be greater and the settling time, shorter.

3.3.4 The use of the sigmoid approach

One drawback of sliding mode control when we have high gains in the feedback loop is the so-called chattering phenomenon, which consists of an oscillation around the sliding surface. According to Young, Utkin and Ozguner (1996), there are two main causes for this oscillation. First, because we consider an ideal behavior for the actuators, and therefore, the switching mechanism can work at infinite frequency. In this case, parasitic dynamics that were neglected can be excited, generating a small amplitude high frequency oscillation. In the second case, and most common, it is due to non-idealities on the actuator system, such as delay in the switching mechanism. To overcome this problem, many authors suggest changing the sign function by a sigmoid function (sgm) (ERTUGRUL et al., 1996;

Figure 20 – Theoretical phase plane for different gains: (a) $\gamma_1 = 5.01$, (b)$\gamma_2 = 25.77$, (c)$\gamma_3 = 320.69$, (d)$\gamma_4 = 1176$ and (e)$\gamma_5 = 2520$.

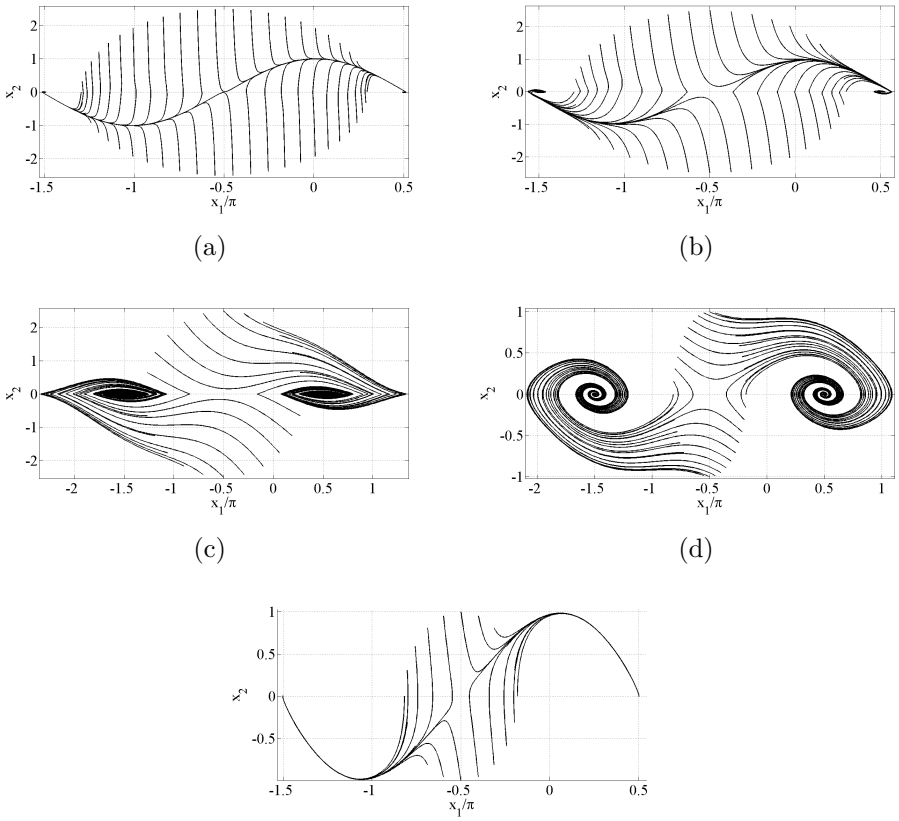

(a) (b) (c) (d) (e)

Source: From author.

SLOTINE; SASTRY, 1983; SLOTINE; LI et al., 1991).

In this work we used the following sigmoid approximation for high gains in the feedback loop ($\gamma > 100$):

$$G_{\text{sgm}}.\text{sgm}(y_2) = G_{\text{sgm}} \frac{y_2}{|y_2| + \epsilon} \tag{101}$$

The parameter ϵ allows the adjustment of the slope of the sigmoid function around the origin and the parameter G_{sgm} is the gain multiplying the function. One great advantage of the digital approach to the control system, presented in this work, is the capability to change the G_{sgm} parameter digitally, increasing the overall gain of the system.

Through the control condition described in (47), one can see that the value of γ must increase proportionally with the frequency of ϕ_0 in order to keep the closed loop stable. For example, assuming that ϕ_0 is a sinusoidal signal which must be suppressed:

$$\phi_0 = A \sin(\omega t) \tag{102}$$

and

$$\dot{\phi_0} = \omega A \cos(\omega t) \tag{103}$$

The frequency ω multiply the amplitude A, increasing the value of $|\dot{\phi_0}|$ significantly. Therefore, according to the Nyquist sampling theorem, and given the fact that γ can be changed digitally, the proposed system can be used to suppress signals with frequency up to the Nyquist frequency ($\frac{f_s}{2}$), where f_s is the sampling frequency.

In the proposed system, the chattering effect is caused due to the delay in the switching mechanism induced by the low pass filter and, for that reason, we can observe the chattering in the simulation. This effect becomes a drawback when we have a high closed-loop gain ($\gamma > 100$).

The simulation results for the closed-loop operation with sign and sigmoid functions are presented in Fig. 21. In this figure, the effect of the sigmoid function and its advantages over the sign function on the system can be clearly observed. The control system operates with a gain of $\gamma = 1176$, and the input signal shown in Fig. 21(a) contains only the disturbance, i. e. $\Delta\phi = 0$ with ϕ_0 a sinusoidal signal with peak voltage of 1 V and 3 Hz frequency. One can observe that the output signal, represented by Fig. 21(b), for the sign function (black line) is disturbed by the chattering phenomenon, oscillating around the equilibrium point. On the other hand, when the system operates with the sigmoid function (red line), this oscillation is heavily attenuated, smoothing the behavior of the system, and decreasing the chattering for the same gain value. The sign and sigmoid function signals used to control the system are shown in Fig. 21(c).

Figure 21 – Comparative analysis with (a) Input signals with $\Delta\phi = 0$ with ϕ_0 a sinusoidal signal 3 Hz frequency, (b) output signal for sign in black and sigmoid function in red (c) sign and sigmoid function

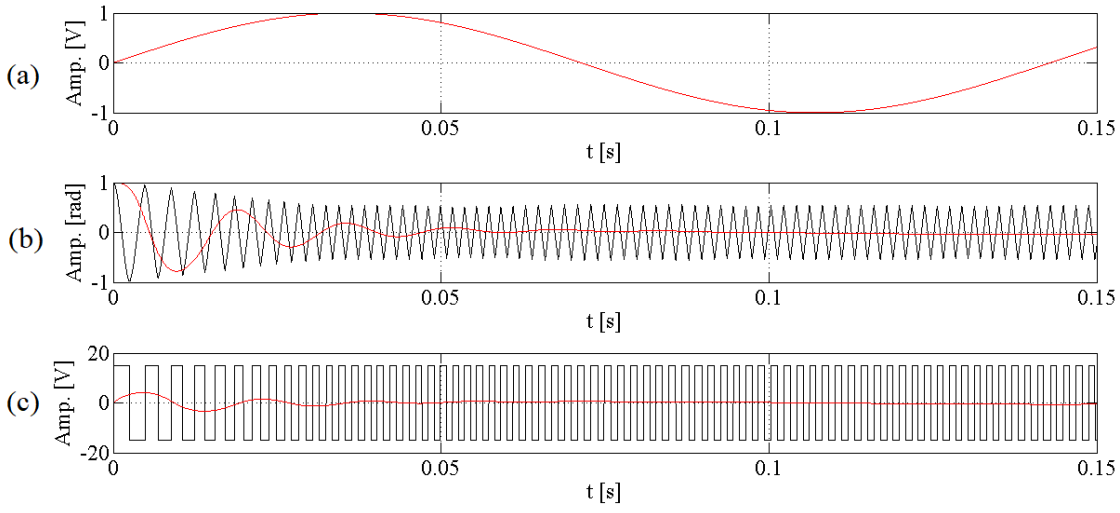

Source: From author.

Besides that, the sigmoid effect can be observed in the phase plane. One can observe in Fig. 22 that the system converges to the equilibrium point $(x_1 = \pi/2, x_2 = 0)$ with an abrupt change when the system state crosses the axis $x_2 = 0$, by using the sign function (black curve). On the other hand, the system has a smooth behavior for the sigmoid function (red curve). Consequently, the chattering effect observed is shorter for the sigmoid function.

Figure 22 – Phase plane comparative analysis for sign and sigmoid function.

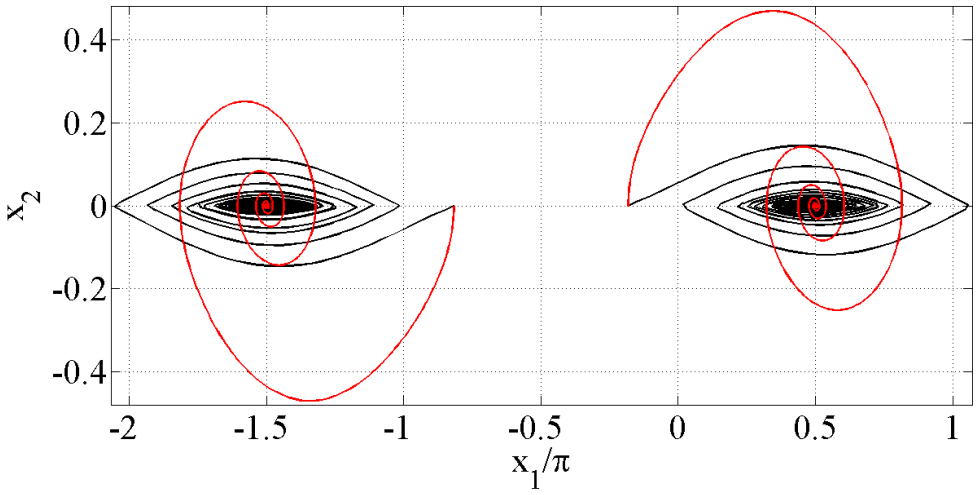

Source: From author.

3.3.5 Lyapunov analysis of the nonlinear system

In order to study the stability according to analysis of the nonlinear system, the choice of a specific equilibrium point $(x_1 = \pi/2,\ x_2 = 0)$ was necessary to be in the origin of the state-space. In this way, the stability around the origin, that is the steady state point, will be analyzed.

For a better approximation to a real system, the sign function is approximated by a sigmoid function given by $\text{sgm}(y_2) = y_2/(|y_2| + \epsilon)$, $\epsilon > 0$ (sufficiently small). Thus, by analogy with (52) and (53) the state equations are given by:

$$\dot{y}_1 = \gamma \frac{y_2}{|y_2| + \epsilon} \tag{104}$$

and

$$\dot{y}_2 = -\frac{AV}{\tau} \sin(y_1) - \frac{y_2}{\tau} \tag{105}$$

In order to proceed with the analysis, we use Global Invariant Set theorem (SLOTINE; LI et al., 1991), described in Theorem 3.1.

Theorem 3.1 – Global Invariant Set Theorem: Considering a time invariant (i.e., autonomous) system $\dot{x} = f(x)$, with f continuous, let $V_l(x)$ be a scalar function with continuous first partial derivatives. Assuming that $V_l(x) \to \infty$ as $||x|| \to \infty$ and $\dot{V}_l(x) \leqslant 0$ over the whole state space, let R be the set of all points where $V_l(x) = 0$, and N be the largest invariant set in R_l. Then, all the solutions globally asymptotically converge to N as $t \to \infty$ (SLOTINE; LI et al., 1991).

Consider a second order system with the form:

$$\ddot{x} + b(\dot{x}) + c(x) = 0 \tag{106}$$

where b and c are continuous functions with the sign conditions described in the following equations:

$$\dot{x} + b(\dot{x}) > 0 \quad \text{for} \quad \dot{x} \neq 0 \tag{107}$$

and

$$xc(x) > 0 \quad \text{for} \quad x \neq 0 \tag{108}$$

Together with the continuity assumptions, the sign conditions on the functions b and c imply that $b(0) = 0$ and $c(0) = 0$. A positive definite function for this system is described by (109) (SLOTINE; LI et al., 1991):

$$V_l = \frac{1}{2}\dot{x}^2 + \int_0^x c(y)dy \tag{109}$$

By deriving (109) we obtain:

$$\dot{V}_l = \dot{x}\ddot{x} + c(x)\dot{x} = -\dot{x}b(\dot{x}) - \dot{x}c(x) + c(x)\dot{x} = -\dot{x}b(\dot{x}) \leqslant 0 \tag{110}$$

Furthermore, by hypothesis, $\dot{x}b(\dot{x}) = 0$ only if $\dot{x} = 0$. This implies that $\ddot{x} = -c(x)$ by (106), which is nonzero as long as $x \neq 0$. Thus, $\ddot{x}$ is ever equal to zero only if $x = 0$ and the system is in the equilibrium point $x = 0$, $\dot{x} = 0$. In addition, with R_l equal to the set defined by $\dot{x} = 0$, the largest invariant set N in R_l contains only one point, namely $x = 0$, $\dot{x} = 0$. The use of the local invariant set theorem indicates that the origin is a locally asymptotically stable point.

Finally, the interferometric nonlinear system can be described by equations in the form of (109) and (110). By deriving (105) we obtain:

$$\ddot{y}_2 = -\frac{AV}{\tau}\cos(y_1)\dot{y}_1 - \frac{\dot{y}_2}{\tau} \tag{111}$$

Replacing (104) in (111) we obtain:

$$\ddot{y}_2 = -\frac{AV}{\tau}\cos(y_1)\gamma\frac{y_2}{|y_2|+\epsilon} - \frac{\dot{y}_2}{\tau} \tag{112}$$

Rewriting (112) we obtain a second order system as follows, where the arbitrary functions b and c, when compared with (106), represents $b(\dot{y}_2) = (\dot{y}_2)/\tau$ and $c(y_2) = -\frac{AV}{\tau}\cos(y_1)\gamma(y_2/(|y_2|+\epsilon))$:

$$\ddot{y}_2 + \frac{\dot{y}_2}{\tau} + \frac{AV}{\tau}\cos(y_1)\gamma\frac{y_2}{|y_2|+\epsilon} = 0 \tag{113}$$

Therefore, considering the conclusion obtained in Section 3.3.3, the state variable y_1 of the system will be between $-\pi/2 < y_1 < \pi/2$, and $\cos(y_1) > 0$, then a positive definite function for the system is:

$$V_l = \frac{1}{2}(\dot{y}_2^2) + \int_0^{y_2}\frac{AV}{\tau}\cos(y_1)\gamma\frac{y_2}{|y_2|+\epsilon}dy_2 \tag{114}$$

Differentiating (114), we obtain:

$$\dot{V}_l = \dot{y}_2\ddot{y}_2 + \left(\int_0^{y_2}\frac{AV}{\tau}\cos(y_1)\gamma\frac{y_2}{|y_2|+\epsilon}dy_2\right)\dot{y}_2 \tag{115}$$

Considering (112), we obtain:

$$\dot{V}_l = -\dot{y}_2\frac{\dot{y}_2}{\tau} \tag{116}$$

Therefore, according to the global invariant set theorem and the results obtained in Section 3.3.3, the equilibrium point at the origin is asymptotically stable.

It is important to note that, by using the output as a state variable, the control system forces this variable to zero independent of the operation point in one of the infinite equilibrium points, thus the proposed goal is achieved without the need to analyze which of the equilibrium points the system is operating.

3.4 Closed-loop simulation

The block diagram of the control system, shown in Fig. 4, was simulated on Simulink® as presented in Fig. 23.

The phase variation $\Delta\phi$ was provided by the piezoelectric actuator under evaluation (PZT) in an experimental setup. Provided that this piezoelectric actuator operates on its linear region, the phase shift (in radians) in the interferometer is directly proportional to

Figure 23 – Block diagram to simulate the closed loop Michelson interferometer.

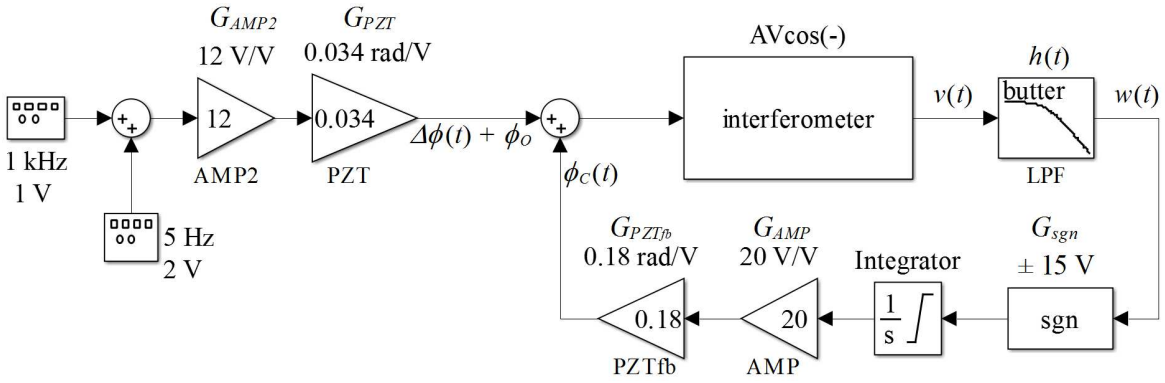

Source: From author.

the voltage (volts) applied. Thus, the signal of interest $\Delta\phi(t)$ and the static phase shift ϕ_o can be synthesized by voltage signal generators, and superimposed by the sum block. The signal of interest was sinusoidal with peak voltage of 1 V and 1 kHz frequency, while the static phase shift was a sinusoidal with peak voltage of 2 V and at a frequency of 5 Hz. The resultant signal was amplified by amplifier 2 (AMP2) ($G_{AMP2} = 12$ V/V) and applied on the PZT ($G_{PZT} = 0.034$ rad/V), that provided the conversion from voltage to angle in radians. This voltage simulates the signal of interest $\Delta\phi(t)$ superimposed by the static phase shift ϕ_o spurious variation.

The feedback loop comprises the low-pass filter (LPF) $h(t)$ (gain at the pass-band $G_{LPF} = 1$ V/V), the sgn function (sign function with gain $G_{\text{sgn}} = \pm 15$ V); the integrator $(1/s)$ followed by an amplifier AMP ($G_{AMP} = 21$ V/V) and the feedback piezoelectric actuator PZT_{fb} (gain $G_{PZT_{fb}} = 0.18$ rad/V), generating a total feedback gain of $\gamma = 56.7$ and justifying the choice of the sign function. The "interferometer" block simulates the relation $v(t) = AV\cos[\Delta\phi(t) + \phi_o + \phi_c]$, where the signal of correction is $\phi_c = -\phi_o + \pi/2$; the AV product was set to 1 V in the simulation. Therefore, the output signal will become in phase quadrature working point.

The simulation result for the open loop operation is presented in Fig. 24, where the input signal is shown in Fig. 24(a). One can observe that the output signal, represented by Fig. 24(b), was disturbed by the static phase shift ϕ_o spurious variation and the signal of interest $\Delta\phi(t)$ was not properly recovered, presenting a spurious low-frequency variation.

After that, the closed loop operation was simulated using the same parameters and the result is presented in Fig. 25.

One can observe that the output signal was properly recovered in Fig. 25(b), where the static phase shift spurious variation was removed, i.e., the signal fading was suppressed and the output signal remained on quadrature working point. The behavior of the sign function is shown in Fig. 25(c).

Figure 24 – Simulation results for open loop operation. (a) Input signal. (b) Output signal.

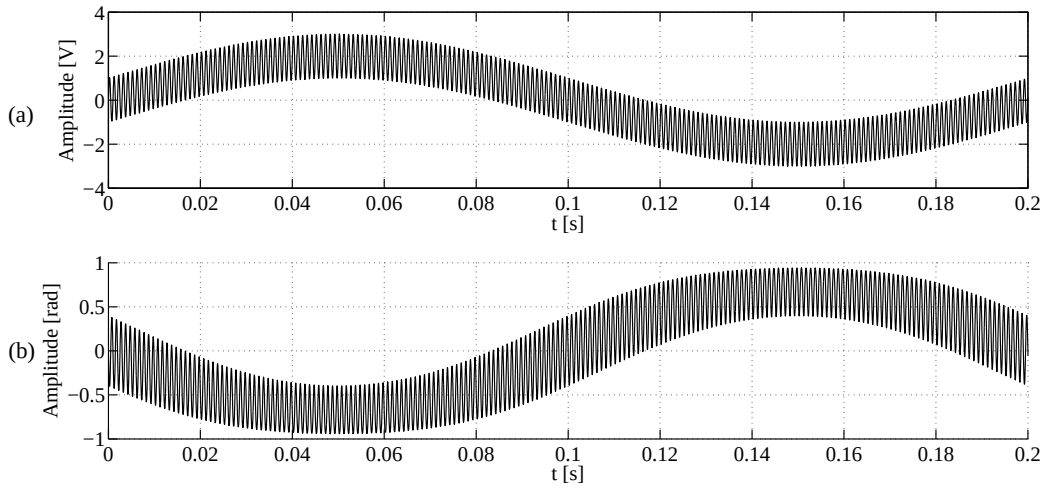

Source: From author.

Figure 25 – Simulation results for closed loop operation. (a) Input signal. (b) Output signal. (c) sign function.

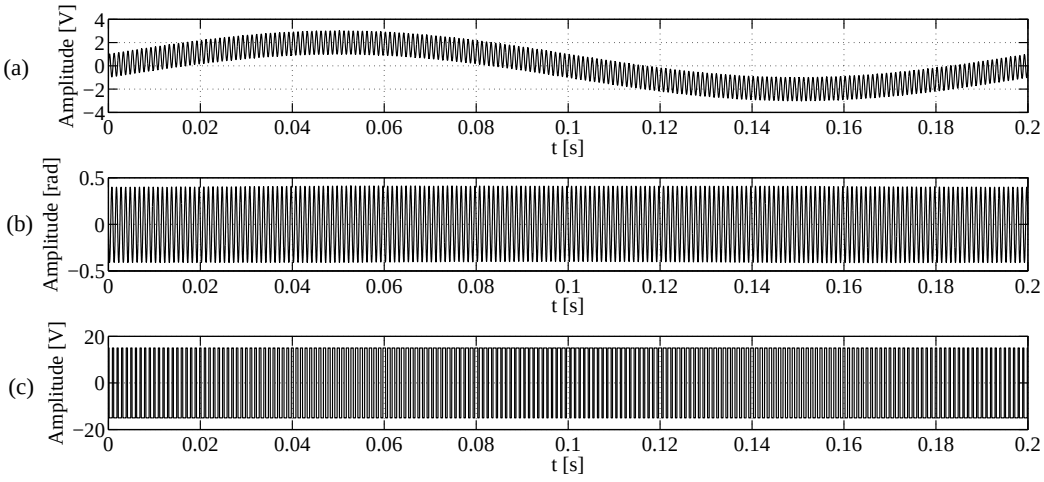

Source: From author.

4 Experimental Setup

In this chapter, details of the different interferometers configurations used regarding the application of the nonlinear control technique are shown, as well as details of the analog and digital control implementations.

4.1 Bulk Michelson interferometer

The experimental setup comprises the Michelson interferometer and the nonlinear control system, as shown in Fig. 26.

Figure 26 – Closed-loop Michelson interferometer setup.

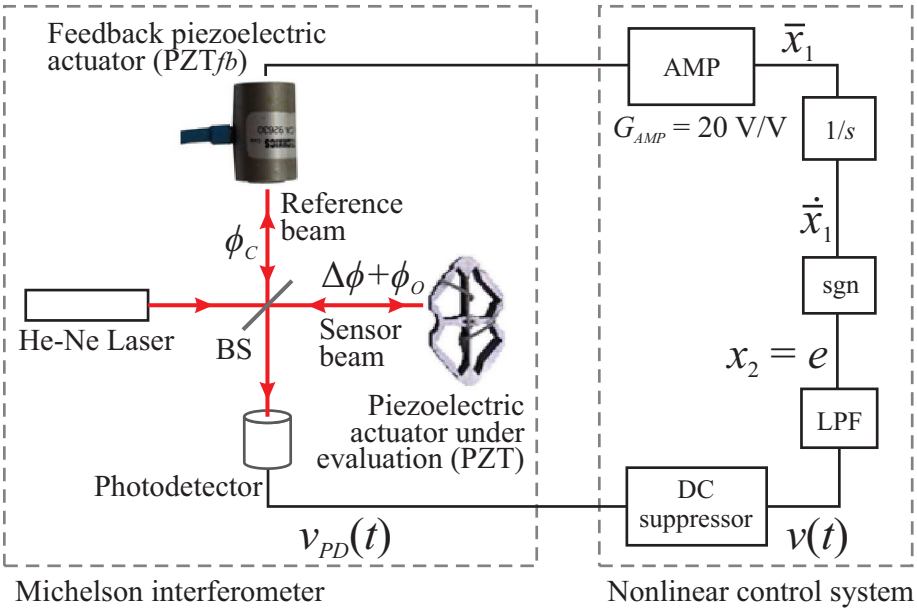

Source: From author.

In the Michelson interferometer, one of the arms contains the feedback piezoelectric actuator (PZT_{fb}), from Control Technics, while the other one contains the piezoelectric actuator under evaluation (PZT) (or an aluminum or steel sample). The optical signal acquired from the photodetector is converted to a voltage by a transimpedance circuit. Then, this voltage was processed by the electronic control circuit which, in turn, generated the nonlinear control signal to be applied on the feedback piezoelectric actuator, in order to keep the interferometer in quadrature and suppress the signal fading. It is noteworthy that this control system does not require a reset system, differently from usual control systems, as discussed in Chapter 1.

This experimental setup was used to detect the sinusoidal vibration to the characterization of a multi-axis piezoelectric actuator, acquiring sub-nanometric displacement amplitudes, linearity, hysteresis, frequency response and mechanical resonances of the actuator. Also, this setup allows to acquire arbitrary waveforms and study the nonlinear control system without interferometric input signal and acquire the experimental phase plane.

A photograph of the closed loop Michelson interferometer is shown in Fig. 27. It is important to note that, in this configuration the actuators have a tiny mirror attached to it.

Figure 27 – Photograph of closed-loop Michelson interferometer setup.

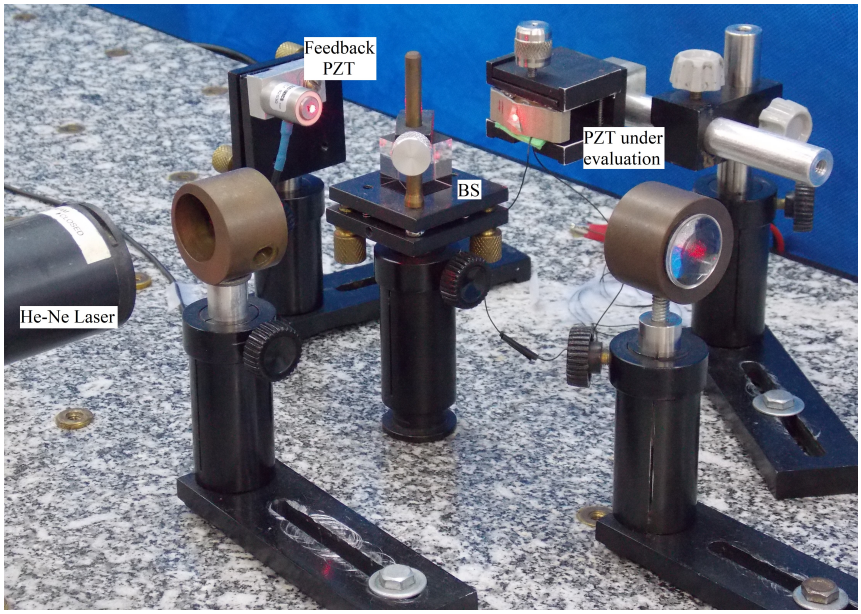

Source: From author.

4.1.1 Speckle interferometry

This section presents the experimental setup for speckle interferometry, that is a well established technique to characterize rough objects by optical means. For instance, when the samples (or object under evaluation) have a rough or polished (diffuse) surface without mirror in the interferometer arms, the laser beam is scattered taking a grainy appearance, as shown in Fig. 28. Consequently, a speckle pattern is obtained in the interferometer output (MALACARA, 2007). This approach offers the advantage that the alignment of the sample is not crucial for the proper operation of the interferometer, once we have speckle pattern in the interferometer arms, besides working with rough surface, increasing the range of application of the controlled interferometer. In additional, we

obtain the voltage output signal with a photodetector, making possible to use the same mathematical modeling of the conventional interferometer, showed in Section 2.1.

Figure 28 – Photograph of the speckle pattern resulting from the beam reflected by the sample.

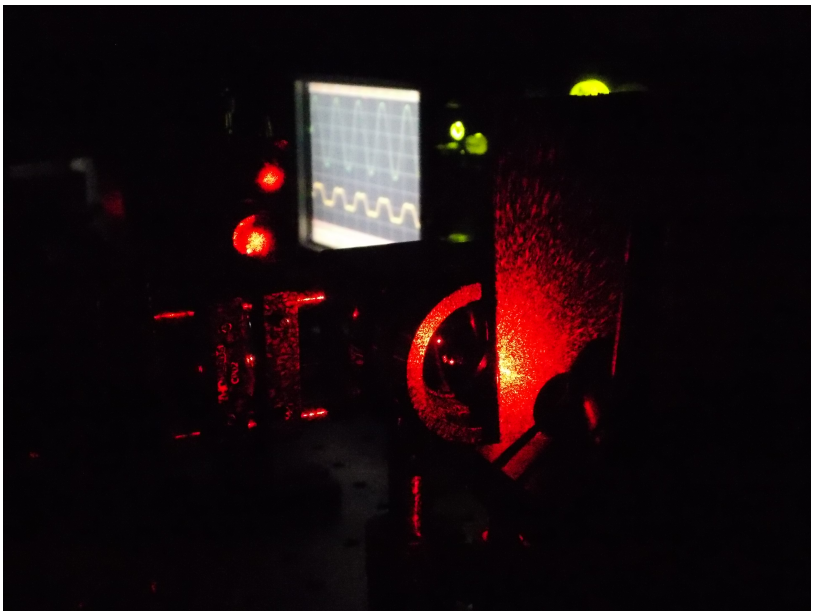

Source: From author.

There were used three different setups for speckle interferometry, the first and third ones to measurements of samples with a rough surface, and the second applied to a polished surface. The experimental setups comprise the Michelson interferometer and the nonlinear control system, as shown in Fig. 29. The Michelson interferometer was assembled with a He-Ne laser (wavelength of 632.8 nm and power of 5 mW), a beam-splitter (BS, 50 : 50 split ratio) and a photodetector for the first and second setups. In the first setup, shown in Fig. 29(a), a positive lens with focal length of 50 mm was used in the sensor arm, and negative lens with focal length of 40 mm and a neutral density filter (NDF) with optical density of 0.3 (with transmission of 50%) in the control arm. The positive lens was used to focus the laser beam in the sample that was without mirror, forming a speckle pattern in the sample reflection. On the other hand, the control actuator has a tiny mirror in the setup 1, then it was necessary to use a NDF and the negative lens to reduce the beam intensity, making possible to interfere it with beam reflected by the sample. This intensity distribution and the statistics of the speckle pattern are an indication of the roughness of the surface (MALACARA, 2007). Therefore, for a rough surface we will have a low intensity, being necessary to decrease it in the control arm.

In the second setup, shown in Fig. 29(b), both control and sensor arms are without mirrors, then, a positive lens with focal length of 75 mm was used in the interferometer

input to obtain the speckle pattern in the interferometer output. A photograph of the speckle interferometer is shown in Fig. 30.

Figure 29 – Experimental setup for rough surfaces: (a) Setup 1 with positive and negative lens for measurements in rough surfaces. (b) Setup 2 with positive lens only for measurements in polished surfaces.

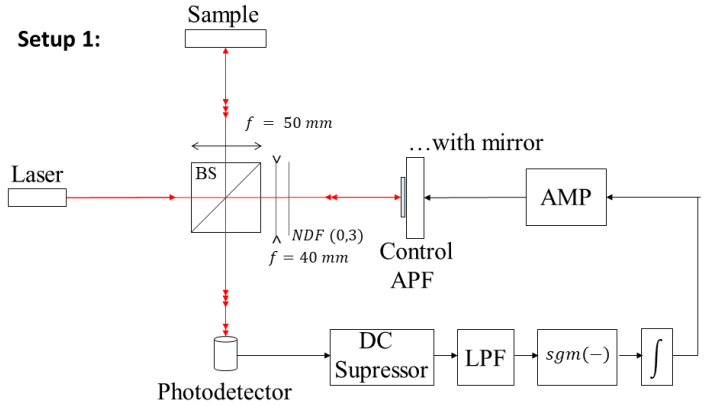

(a)

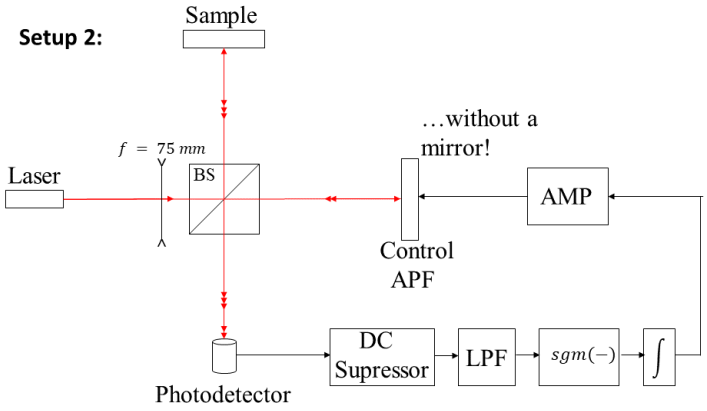

(b)

Source: From author.

It is important to point out that the sample in the sensor arm (for Setup 1 and 2) and the piezoelectric actuator in the control arm (only in Setup 2) are both without mirrors. Thus, we have a speckle pattern in the output signal. The AV factor in (16) will be small due to the scattering of the light in the interferometer's arms. Therefore, as the AV factor decreases, the gain γ must be increased in order to guarantee the stability, as shown in Section 3.3.1. Since these configurations were applied to laser ultrasound tests, the gain of the transimpedance circuit for this frequency range (>1 MHz) decreases considerably, affecting even more the AV factor, in the order of milivolts.

A third experimental setup for speckle interferometry was implemented aiming to achieve a better AV factor. In this setup, the interferometer was assembled with a He-Ne laser (wavelength of 632.8 nm and power of 30 mW), we use a tiny mirror in the control

Figure 30 – Photograph of closed-loop speckle Michelson interferometer setup.

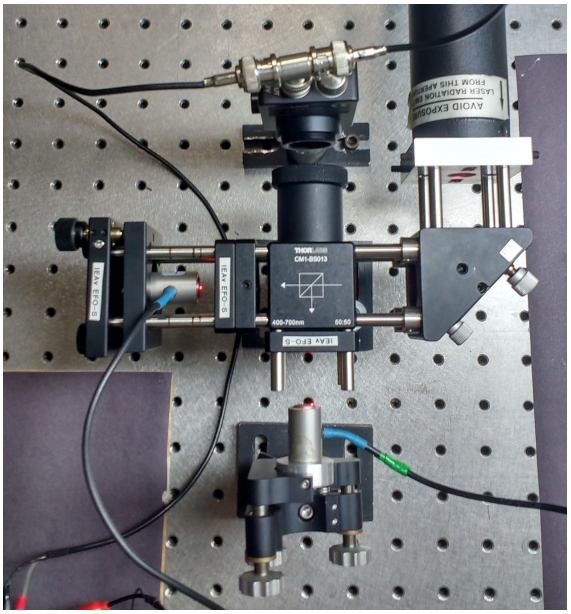

Source: From author.

arm and positive lens with focal length of 50 mm in the sensor arm, as shown in Fig. 31. The sample is positioned in the positive lens focus, which when combined with the control spot generate a scintillating dot in the interferometer output. It is important to note that in this case we do not have the fringe pattern in the interferometer output, only a single scintillating dot because the beam is not expanded in the interferometer arms. Therefore, the output intensity will be greater, resulting in a higher AV factor, in the order of volts.

Figure 31 – Experimental setup for speckle interferometry aiming to achieve a better AV factor.

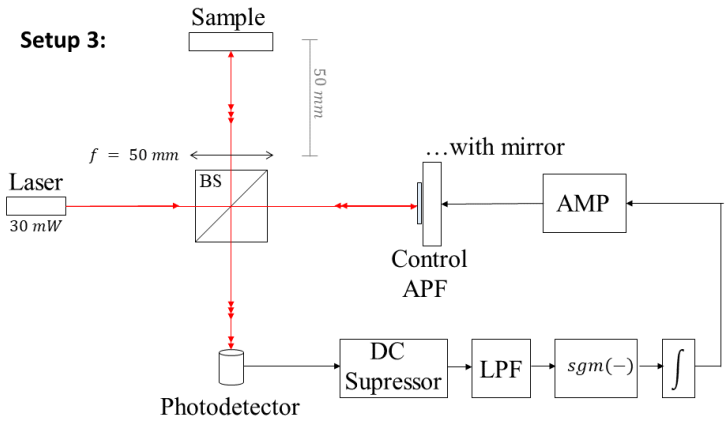

Source: From author.

These experimental setups were used to detect the sinusoidal vibration to the characterization of a piezoelectric actuator in the ultrasound range, acquiring sub-nanometric

displacement amplitudes, frequency response and mechanical resonances. Also, these setups were used to ultrasound detection and the detection of longitudinal waves generated by a Q-switched laser in aluminum and steel samples.

4.2 All-fiber Mach-Zehnder interferometer

The Mach-Zehnder configuration used in this work is shown in Fig. 32 (with fiber length and power values in each arm), based on the configurations presented in Udd and Spillman (2011) and Giallorenzi et al. (1982). This configuration comprises a CW diode laser (wavelength at 1550 nm and nominal optical power of 7 mW), isolator (Thorlabs, center wavelength at 1550 nm – ISO), single mode fiber (Thorlabs – model 980HP), two single mode couplers (Go4Fiber, operating wavelength at 1550 nm – C1 and C2), two phase shifters modulators (PZT1 and PZT2) and two photodetectors (PD1 and PD2 – from Newport, model 818-BB-30). The fusion splicer machine used is from Ericsson, model FSU-925-PM.

In Stowe, Moore and Priest (1982), Hi-Bi (polarization maintaining) fibers were used to control the polarization in interferometers due to the degradation of the output signal for uncorrelated random drifts in polarization (fading). It should be noted that for the proposed system, the fading problem was avoided using common fibers with the low-cost nonlinear control proposed in this work (MARTIN et al., 2017a), which reduces even more the overall costs and simplifies the system.

Figure 32 – Schematic of losses and fiber lengths in the all-fiber Mach-Zehnder interferometer.

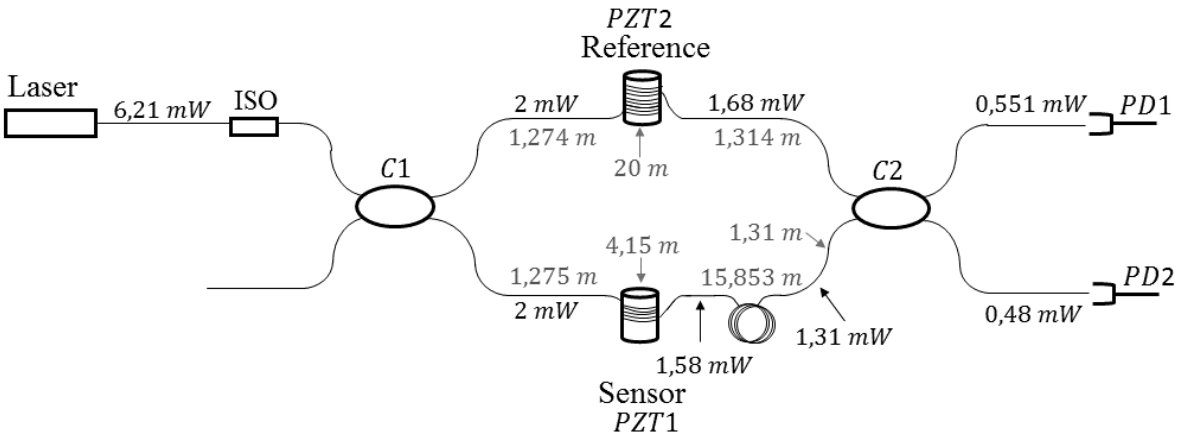

Source: From author.

A photograph of the Mach-Zehnder interferometer is shown in Fig. 33. The system is mounted in a PVC (polyvinyl chloride) structure, which makes it compact, lightweight, resistant and capable of being embedded.

Figure 33 – Photograph of Mach-Zehnder interferometer.

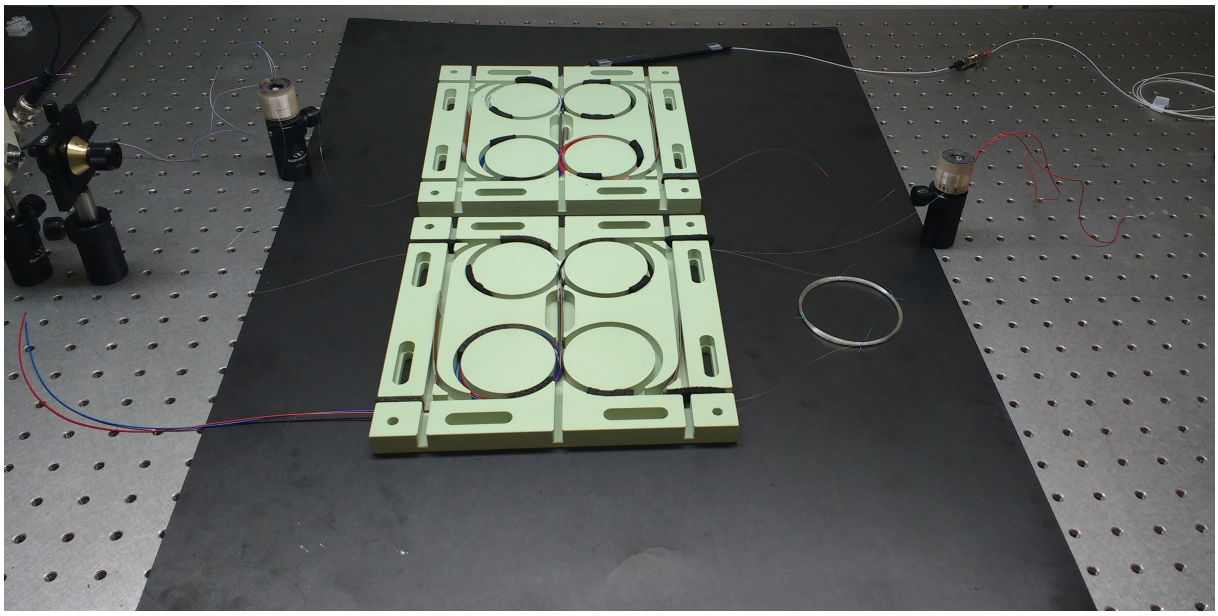

Source: From author.

The optical power in each point in the interferometer was measured with an optical power-meter model ML9001A from Anritsu at each step of the assembly, and the measurement are shown in Fig. 32. The total losses in each arm of the interferometer are given by:

$$\beta = 10 \log \left(\frac{P_{in}}{P_{out}} \right) \tag{117}$$

where P_{in} and P_{out} are the optical power in the system input and output, respectively.

Therefore, the total losses in the first and second arms are 11.12 dB and 10.519 dB, respectively, and they are mostly caused by insertion loss.

We applied the nonlinear control based on variable structure (MARTIN et al., 2017b) to the all fiber Mach-Zehnder interferometer as shown in Fig. 34. One of the arms of the Mach-Zehnder interferometer was assembled on the feedback phase modulator, and the other one, over the phase modulator under evaluation.

This experimental setup was used to detect the sinusoidal vibration to obtain the frequency response of a fiber phase modulator. Also, to characterize the optical fiber response to temperature. Regarding the control evaluation, this setup allows to obtain the experimental phase-plane for different gains γ and for the sign and sigmoid functions.

Figure 34 – Block diagram of the Mach-Zehnder interferometer with the nonlinear control system.

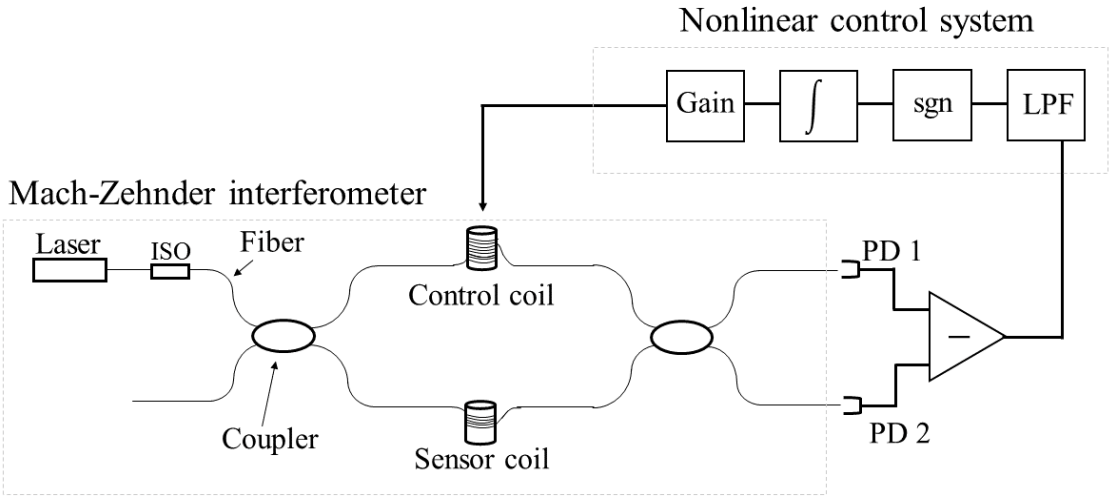

Source: From author.

4.2.1 Fiber phase modulator

There are several available materials that can be used as phase shifter. Usually they have a very small variation of the refractive index changes per applied voltage (JACKSON et al., 1980). In the all-fiber interferometer, we used phase shifters based on the piezoelectric effect. The piezoelectric actuator gain is generally small, although it is possible to amplify it by increasing the number of fiber turns around the piezoelectric actuator, as will be shown in this section.

A schematic of the proposed setup to build the optical fiber phase modulator using a piezoelectric cylinder and a single mode fiber is shown in Fig. 35. In order to determine the actuator gain, it is necessary to estimate the fiber length. A relationship between the gain and the fiber length is demonstrated experimentally in this section.

In the setup bench, one of the coil's extremity was used to initiate the fiber coiling around the PZT cylindrical transducer. The fiber was stretched using a weight with 19.46 g, according to Fig. 35. Therefore, to obtain the relationship between the gain and the fiber length, we used three different lengths for the experimental setup: 3 m, 12 m, 21 m.

A fiber segment was then attached using 5 spots of UV glue (Norland Optical Adhesive from Thorlabs) above the B mark on the PZT base (the glue spots are indicated with the A mark in Fig. 36). It is important to leave a spare gap of at least 1 m due to cleaving and possible splicing fails. It should be noted that at each spot of glue we need a three-minute exposure UV light was required to the glue to dry.

After coiling the fiber segment around the PZT, we rotated the holder axis, keeping

Figure 35 – Setup (a) schematic and (b) photograph to build the fiber phase modulator.

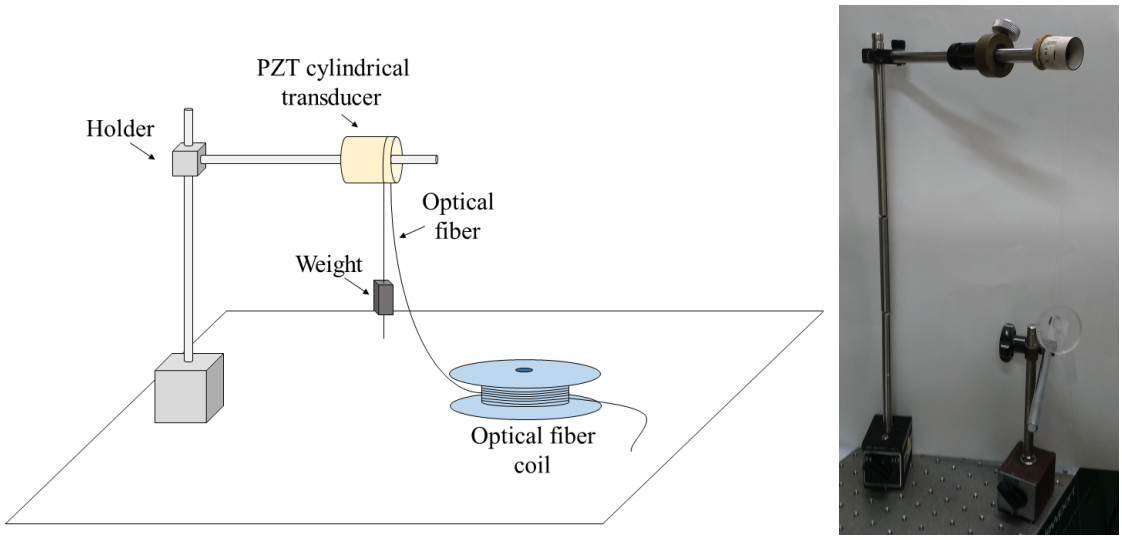

(a) (b)

Source: From author.

Figure 36 – Schematic of fiber segment attached to 5 spots of UV glue above the B mark on the PZT base.

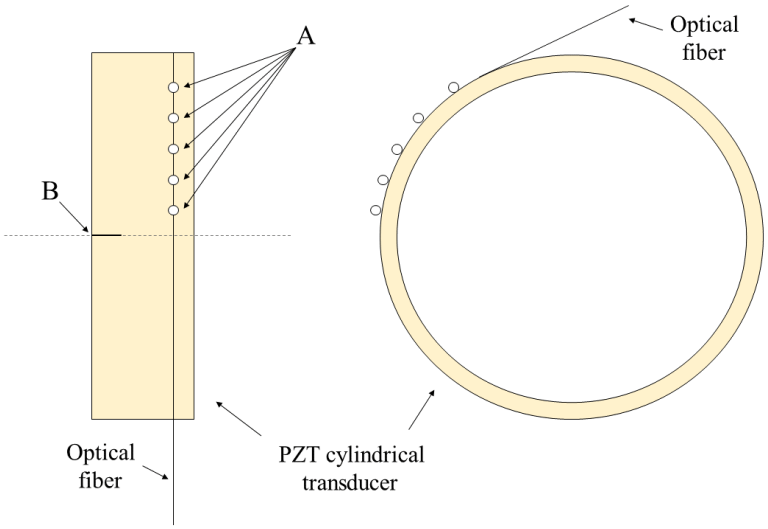

Source: From author.

the mechanical stress constant using the weight located at its end (Fig. 37). Then, the final fiber segment was attached by other 5 spots of UV glue below the B mark on the PZT. Another spare gap of at least 1 m should be left. The final glue spots are indicated with the C mark in Fig. 38.

Four different fiber phase modulators with piezoelectric cylinder were assembled in the laboratory. In Table 4, we show the number associated to each fiber phase modulator

Figure 37 – Setup (a) schematic and (b) photograph to build the fiber phase modulator.

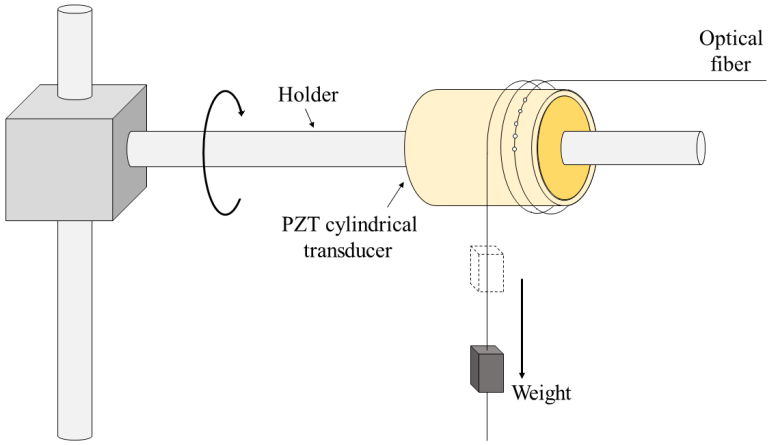

(a)

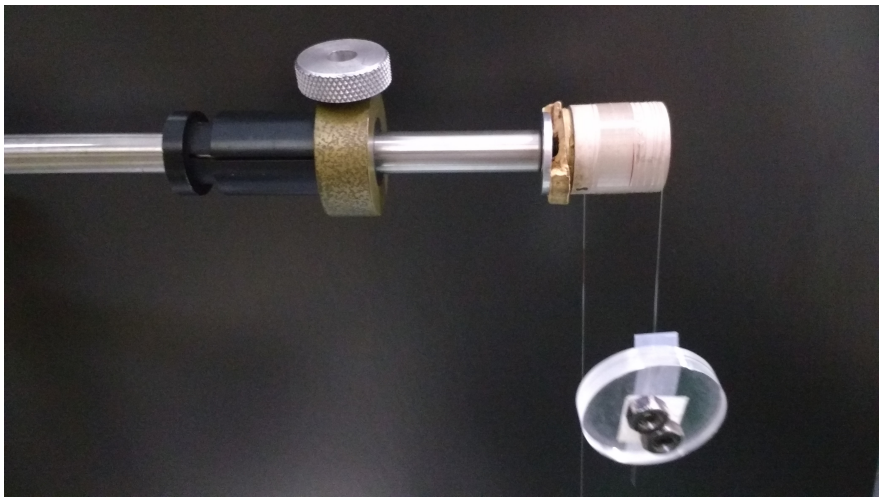

(b)

Source: From author.

(see Fig. 39), the fiber length, the total turns around the PZT, the actuator gain for the frequency of 10 Hz and the total layers.

It should be noted that there is a linear relationship between the experimental actuator gain and the number of turns around the PZT in the first layer of fiber (JACKSON et al., 1980). Regarding the second layer, the gain decreases to approximately one third for the same turns in the previous layer, as shown in Table 4. It is a result of the mechanical dumping due to the fiber layers. For instance, considering the three-layer experiment it is possible to calculate the gain by taking into consideration the fiber jacket and the PZT radius, as discussed below.

Considering that the PZT radius is 12.7 mm and is 25.4 mm long, using 20 mm length to coil the fiber, the first layer will have around 80 turns, and 6.38 m of fiber will be

Figure 38 – Setup (a) schematic and (b) photograph of the final fiber segment attached to 5 spots of UV glue below the B mark on the PZT base.

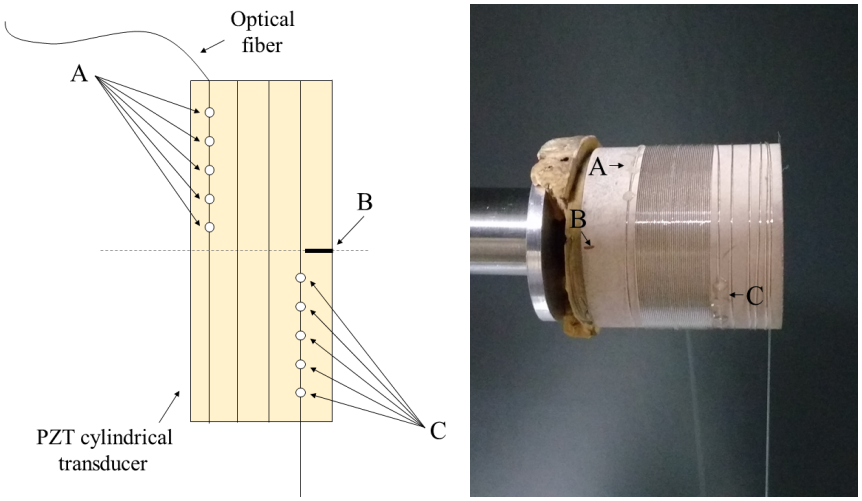

(a) (b)

Source: From author.

needed. If we consider the fiber cladding with 0.25 mm, on the second layer it is necessary to add 0.5 mm (because of the first layer). Therefore, the second layer will demand 6.51 m of fiber. Finally, on the last layer we add four layers of cladding (1 mm), thus, we will use 6.634 m of fiber. The total theoretical fiber of the three-layer PZT is 19.52 m.

The experimental gain obtained for one layer with 37 turns is 2.24 rad/V. As previously noted, for the first layer, there is a linear relationship between the experimental actuator gain and the number of turns (JACKSON et al., 1980). Therefore, the gain for 80 turns should be 4.84 rad/V. Regarding the second layer, if we have a linear relationship, the theoretical gain for 80 additional turns should be the same of the first layer, but the gain decreases in about one third for the same number of turns, thus, the gain for 80 turns in the second layer should be 1.61 rad/V. Finally, in the last layer the gain will be one third of the gain in the second layer, 0.53 rad/V. The total theoretical gain of three-layer PZT is 6.99 rad/V.

Regarding the control system applied to Mach-Zehnder interferometer, it is important to have a high gain in the PZT, such as PZT 4 (Table 4). The large amount of fiber required for a high gain PZT with multiple layers can cause high sensitivity to spurious perturbation. Thus in order to reduce sensitivity to spurious perturbation and to avoid losses due to the additional layers as well as to achieve high sensitivity, we suggest to use a single layer PZT with a linear amplifier in the control arm. Alternatively, phase modulators in parallel (less fiber for the same gain) could be employed. However, in Jackson et al. (1980) it is pointed that the gain in the PZT decreases when the wavelength of the light source is increased and also if the cylinder diameter is reduced.

Table 4 – Fiber phase modulators.

PZT	Fiber length [m]	Total turns	Gain at 10 Hz [rad/V]	Total layers
1	3	37	2.24	1 incomplete
2	3	37	2.24	1 incomplete
3	12	120	4.92	2 incomplete
4	20	200	7.17	3

Figure 39 – Fiber phase modulators (a) PZT1, (b) PZT2, (c) PZT3 and (d) PZT4.

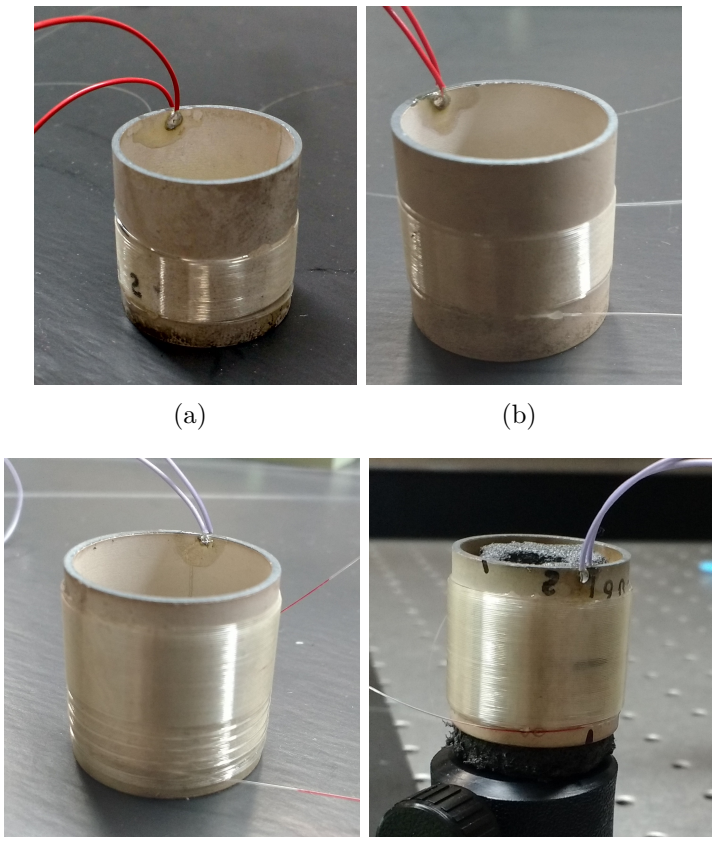

(a) (b)

(c) (d)

Source: From author.

The piezoelectric cylinders 1 and 4, shown in Table 4, were incorporated into the Mach-Zehnder, one as the signal arm and the other as the control arm, as shown in Fig. 32.

4.2.2 Laser coherence

The coherence length is a term used as a measure of the temporal coherence of a light source. The coherence region of an interferometer output is the region where phase modulation can be achieved. If the optical path difference in an interferometer is kept smaller than the coherence length of the light source employed, the fringe visibility of the output obtained will be between 1 and 0. However, when the optical path difference is

longer than the coherence length of the light source employed, the fringe visibility vanishes and the phase modulation becomes undetectable (GRATTAN; SUN, 2000).

The coherence length of the light source used in the all-fiber Mach-Zehnder interferometer was measured by employing a spectrum analyzer connected to the diode laser output to obtain the full width at half maximum (FWHM - $\Delta\nu$). The laser output spectrum is shown in Fig. 40.

Figure 40 – Laser source spectrum.

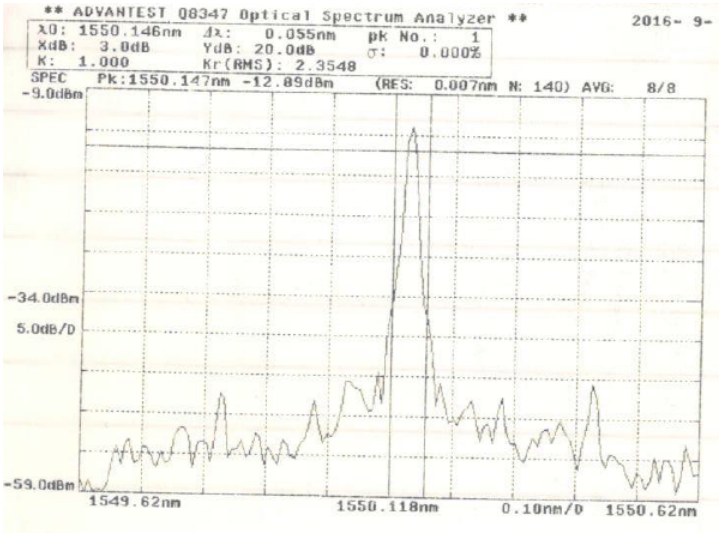

Source: From author.

The relation between the frequency (ν) and wavelength (λ) is given by:

$$\nu = \frac{c}{\lambda} \tag{118}$$

where c is the speed of light in vacuum (3.10^8 m/s).

By deriving (118):

$$\Delta\nu = -\frac{c}{\lambda^2}\Delta\lambda \tag{119}$$

From the Fig. 40, we obtain the values of the laser frequency ($\lambda = 1550.146$ nm) and the FWHM in terms of the wavelength ($\Delta\lambda = 0.055$ nm). Through (119), it is possible to obtain the FWHM in terms of the frequency ($\Delta\nu = 6.866.10^9$ Hz). Finally, the coherence length is given by Svelto and Hanna (1998):

$$\Delta sc = \frac{c}{2\pi\Delta\nu} \tag{120}$$

The coherence length of the light source by the spectrum analyzer is $\Delta sc = 6.95.10^{-3}$ m. The low coherence length obtained may be due to a low spectrum analyser

resolution, which can cause distortion in the measurement of $\Delta\lambda$. To practically estimate the coherence length, one arm of the interferometer was assembled with 7 additional meters. Then, we continually removed 0.5 m until we obtained the interferometric signal, hence, an estimation of the coherence length. This practical experiment indicated that the coherence length is around 1 m. Hence, throughout the assembly, it is important to guarantee that the interferometer arms have the same length due to this limited coherence length of the light source.

As shown in section 4.2.1, to provide the necessary gain, the control PZT (the PZT 4 was used) has a longer fiber length than the sensor PZT (PZT 1). Thus, interferometer arms are unbalanced, which compels the use of a piece of dummy fiber for balance. An alternative to avoid the problem with coherence length, which sometimes is very discrete, would be the use of a laser with better coherence length (e. g. semiconductor, DFB or fiber lasers) or a dummy piece of fiber to guarantee the same length in the interferometer arms. In the case of this work, we employed the second option, with 15.85 m of fiber to properly balance the interferometer, as shown in Fig. 32.

4.2.3 Difference output

It should be noted that before applying the nonlinear control in the interferometer it is necessary to suppress the DC signal of its output. For this purpose Martin et al. (2017b) used an electronic circuit (Section 4.3) consisting of passive filters, which causes a delay in the output signal and makes it difficult to acquire control parameters such as: overshoot, time of establishment, among others. These parameters are of great importance for a complete and detailed analysis of the control system. Unlike the bulk Michelson interferometer, with the all-fiber Mach-Zehnder interferometer it is possible to obtain two output signals that are 180° out of phase with a simple configuration taken in PD1 and PD2 in Fig. 34. This feature allow us to reach an output without DC components, by utilizing a simple difference electronic circuit presented in Fig. 41.

The circuit in Fig. 41 comprised two summing amplifiers and buffers. The first one gives the weighted sum between one interferometer output signal (V_a) and the voltage divider. The second summing amplifier sums the output of both interferometer output signals (V_x and V_y). The weighted sum is established by resistance ratios and can be regulated by the voltage divider (V_{DC}). Since the resistance values are equal, the weighted sum for both are equal to unity. The transfer function of difference circuit in Fig. 41 is given by:

$$V_{out} = -V_x - V_y = (V_a + V_{DC}) - V_y \tag{121}$$

In Fig. 42, we show the interferometer input signal with amplitude of 700 mV and

Figure 41 – Difference electronic circuit to obtain the interferometer output without DC.

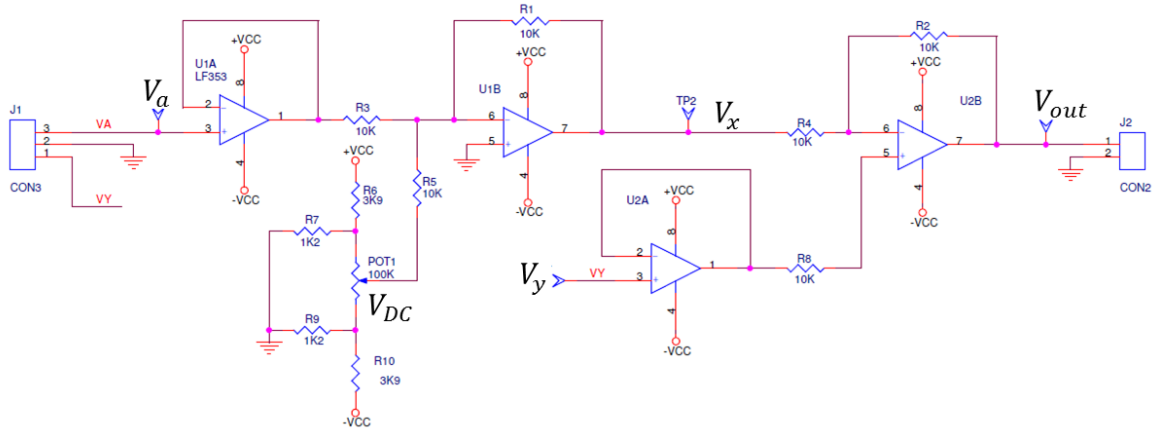

Source: From author.

at a frequency of 1 kHz as the top yellow line, the two outputs signals ((26) and (27)) as the bottom blue and red line, while the output signal without DC is shown in the middle green line. It can be observed that the two output signals are 180° out of phase as predicted in (26) and (27), the DC component was removed and the resultant signal has twice the amplitude of the interferometer output signals.

Figure 42 – Interferometric input signal (yellow), the two outputs signals (blue and red) and the interferometric output signal without DC (green).

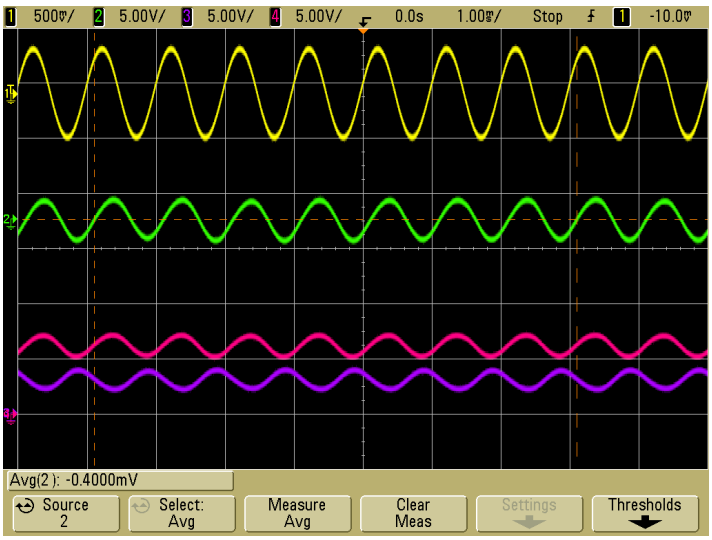

Source: From author.

4.2.4 All-fiber Mach-Zehnder interferometer for modified high-gain approach

To apply the modified high gain approch showed in Section 2.4.2, we use the experimental setup shown in Fig. 43 which comprises a modified all-fiber Mach-Zehnder configuration. Two different phase modulators are incorporated into the sensor arm of Mach-Zehnder: one is in the sensor coil with 21 m of fiber length, and the other is the Peltier cell used in order to vary the temperature in the fiber.

Figure 43 – Experimental setup with Peltier cell.

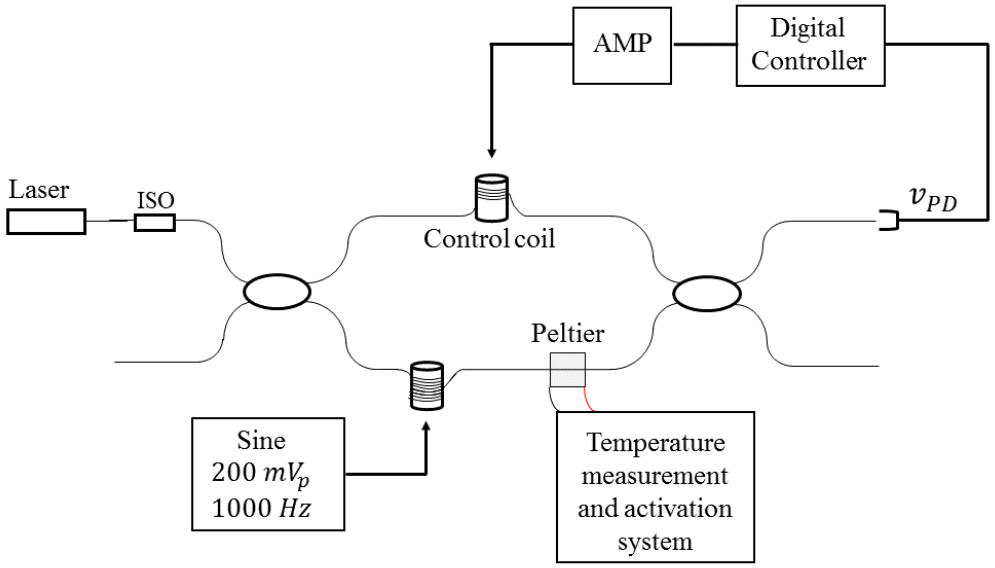

Source: From author.

This test was used to obtain the temperature response in a regular fiber, and since the ambient perturbations (ϕ_0) and the signal temperature of interest are in the same frequency range, it was necessary to use statistical processes to detect the signal of interest, shown in Section 2.4.2. Also, due to the large numbers of tests, repeatability was used to guarantee the quality of the results. Besides that, we use the interferometer in a controlled environment.

4.3 Nonlinear control system: analog approach

The proposed nonlinear control system was implemented using discrete analog components, with the circuit shown in Fig. 44. The input V_{IN} is connected to the photodetector, and the output V_o in a linear amplifier with gain 21 V/V, followed by the feedback actuator. It was used the LF353 operational amplifier due the high slew rate 13 V/μs, being convenient to implement the sign function.

Figure 44 – Analog circuit to implement the nonlinear control.

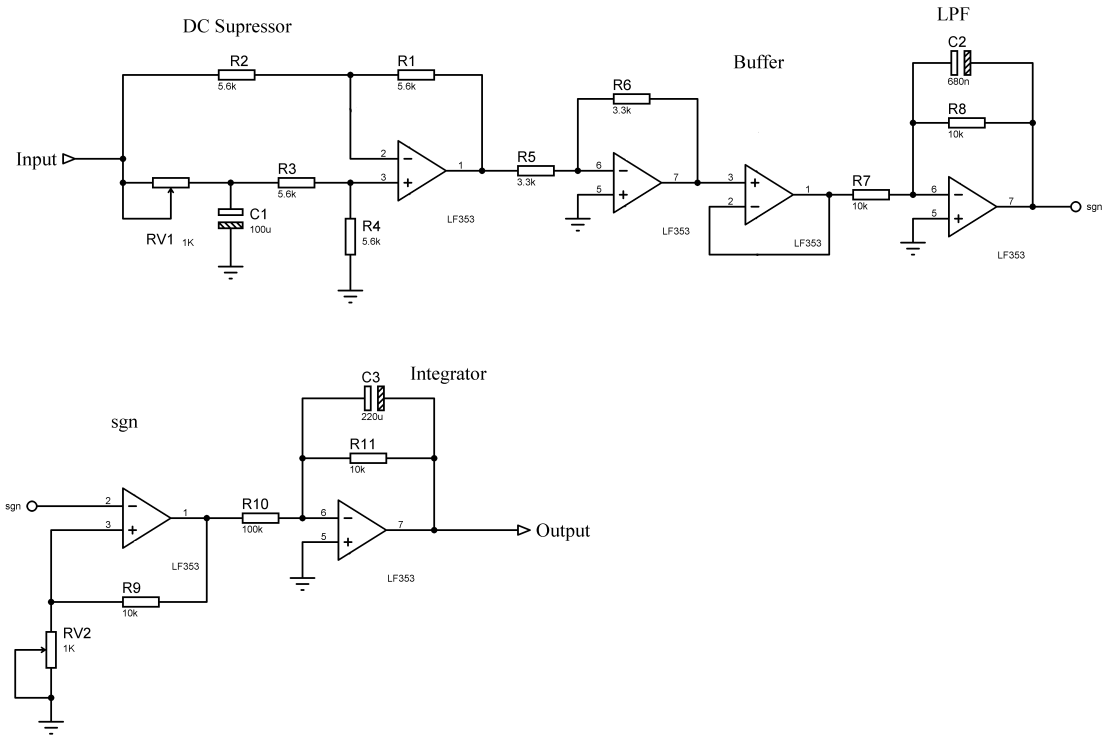

Source: From author.

The "DC supressor" refers to the circuit used to suppress the DC component of the ouput signal. It is important to point out that this DC supressor is only applicable to sinusoidal signals in low modulation index operation ($\Delta\phi(t) \ll \pi/2$ rad).

Through the Fig. 44 we obtain:

$$V_{out} = \left(-\frac{R_1}{R_2}V_{IN} + \left(\frac{R_1}{R_2}+1\right)\left(\frac{R_3}{R_3+R_4}\right)V_{DC}\right)\left(-\frac{R_6}{R_5}\right) \tag{122}$$

Replacing $V_{IN} = V_{DC} + V_{AC}$ in (122), we obtain:

$$V_{out} = \left(-\frac{R_1}{R_2}V_{AC} - \frac{R_2}{R_1}V_{DC} + \left(\frac{R_2}{R_1}+1\right)\left(\frac{R_3}{R_3+R_4}\right)V_{DC}\right)\left(-\frac{R_6}{R_5}\right) \tag{123}$$

In order to suppress the DC component it is necessary that $R_1 = R_2 = R_3 = R_4 = R$. Also, $RV1$ and $C1$ comprises a passive filter whose $RV1C1$ constant need to be adjusted. Thus, for a frequency f, the capacitive reactance in sinusoidal state ($s = j\omega = j2\pi f$) is given by:

$$X_C = \frac{1}{j2\pi f C1} \tag{124}$$

Therefore, the output voltage of the filter corresponds to:

$$V_y = V_x \frac{X_C}{X_C + RV1} = V_X \frac{1/j2\pi fC1}{(1/j2\pi fC1) + RV1} = V_X \frac{1}{1 + jRV1fc12\pi} \tag{125}$$

Hence, aiming to allow only the DC component in the output of the passive filter, the cutoff frequency should have low values, ideally 0 Hz.

The "Buffer" block corresponds to a voltage buffer (unity gain amplifier) used to isolate the feedback circuit and guarantee the coupling with the interferometer. The "LPF" block refers to a first order low pass filter with cutoff frequency of 20 Hz. In the "sgn" block we have a schimitt trigger circuit, and a integrator. A photograph of the feedback system is shown in Fig. 45.

Figure 45 – Photograph of the analog feedback system.

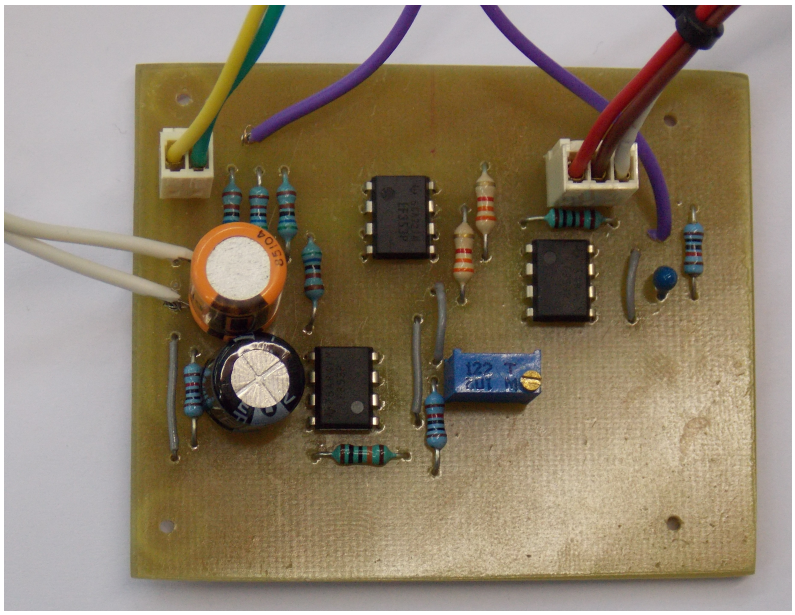

Source: From author.

Therefore, the analog approch presents a low implementation cost when compared to digital one, continuous time operation, avoiding signal sampling issues as aliasing and jitter. Besides, the overall system is more compact (mainly when using SMD - surface mount devices) and has wide input signal ranges.

Also, considering the slew rate of the analog component used to implement the schimitt trigger, i.e. the maximum voltage variation per time unit, we can obtain the ϵ factor to compare with the inclination in the sigmoid approach, as follows:

$$\frac{d}{dx}\left(\frac{x}{|x| + \epsilon}\right) = \frac{1}{\epsilon} = \text{slew rate factor} \tag{126}$$

Regarding that the slew rate factor for LF353 is $13V/\mu s$, we obtain $\epsilon = 7.6(10)^{-8}$. Therefore, using analog components, the sigmoid function becomes extremelly similar to the sign function, even using low slew rate components. However, the total feedback gain achieved in the analog approach is low, and does not cause a significant chattering, removing the requirement of the sigmoid approach as seen in Section 3.3.4.

4.4 Nonlinear control system: digital approach

The nonlinear control system was also implemented using the FPGA (Field Programmable Gate Array) inside the myRIO platform, from National Instruments (FELÃO, 2017), and comprises a DC suppressor (aiming to remove the term A in (16)) a low-pass filter (LPF), a sigmoid function (sgm), an integrator ($1/s$), and a PZT amplifier (G_{AMP}). It is noteworthy that LabVIEW Toolkit for programming and deployment of the FPGA device allows the hardware design to be carried out without prior knowledge of Hardware Description Language (HDL).

Digital controllers present several advantages when compared to analog ones. They are less susceptible to analog device aging and environmental variations and they are capable of performing complex computations at high speed with constant accuracy. Besides that, they present more flexibility since changes can be made in implemented system without rearranging the hardware. In addition it allows the implementation of more complex functions. This type of controller is often implemented in microcontrollers, Digital Signal Processors (DSP) and Field Programmable Gate Arrays (FPGA). In this section, we focus in the use of FPGA devices, since it presents great advantages in processing time, when compared to microprocessors. Each individual task can use different sets of logic cells, which allows multiple tasks to run concurrently.

Another great advantage of the implementation is the ability to digitally configure the gain γ, allowing high gains, and consequently, a fast response of the integrator output to track the spurious disturbances, especially for the proposed setup that has a low AV value. It is noteworthy that robustness and chattering have a trade-off relationship and the implementation in FPGA provides the flexibility to change the topology of the sigmoid function, allowing chattering reduction, still preserving the robustness. Moreover, with the hardware designed in FPGA, the system does not present the non-idealities intrinsic to discrete components.

According to Young, Utkin and Ozguner (1996) if the digital system presents a sufficiently fast sampling rate, the discrete-time implementation of the feedback loops can be considered as a continuous-time system. This assumption brings the advantages of a digital controller allied with the simplifications of continuous-time control design, without losing performance.

This subsection gives details about the functions, comprising the nonlinear control system and the synchronization of the real-time processor algorithm, with the hardware which were implemented in FPGA. The hardware block diagram of the chosen platform is shown in Fig. 46 (NI, 2013). One can see that the analog inputs and outputs are connected directly to the FPGA, which means that, compared with the real-time processor's performance, this configuration provides a higher sampling rate and is able to execute different tasks concurrently.

Figure 46 – Hardware block diagram of myRIO-1900 embedded plataform.

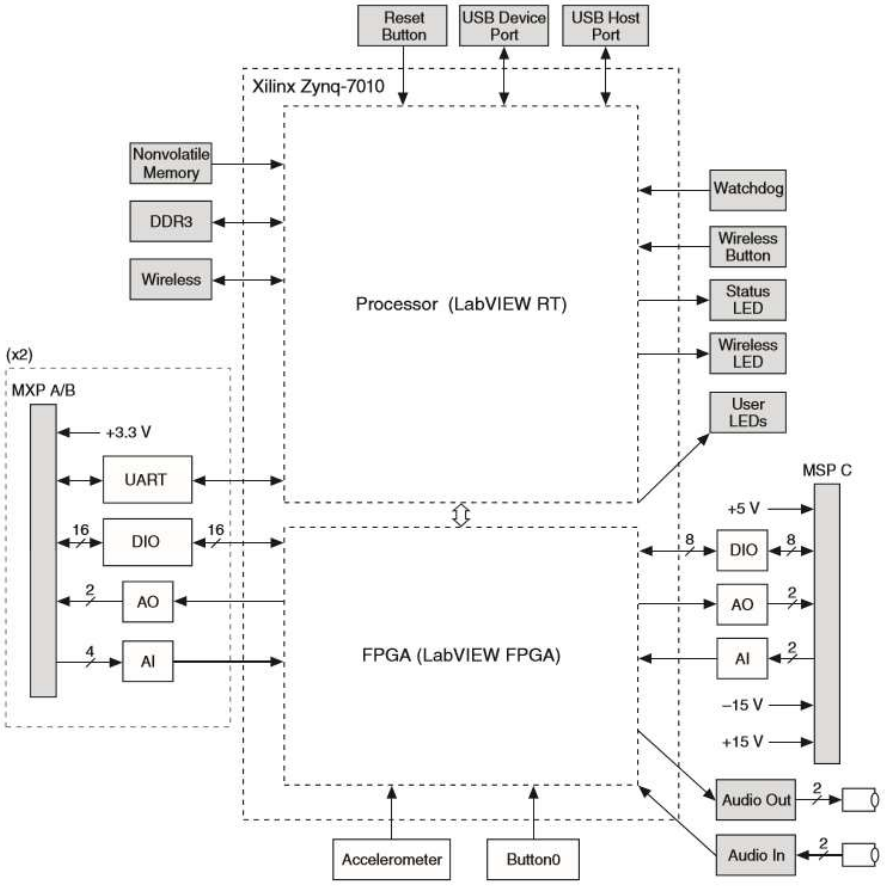

Source: (NI, 2013).

The output signal of the photodetector is sampled at 100 kHz by one of the analog inputs with voltage resolution of 4.883 mV. The DC level of the photodetector signal is determined experimentally through a self-calibration procedure while the system is operating in open loop. This DC value is then suppressed from the sampled signal.

4.4.1 Automatic DC and AV calibration process

As can be observed in Section 3, the nonlinear control system operates with the interferometric output without the DC component. In order to estimate this component, it was necessary to measure the maximum and minimum value of the output signal while a ramp signal was applied in the control actuator. The control algorithm is executed in the FPGA of the myRIO plataform, therefore, it was necessary to change the hardware configuration to apply a ramp signal to the analog output and after, change the FPGA hardware configuration back to the nonlinear control algorithm. When this process is carried out within the same real-time processor algorithm, it is called dynamic FPGA reconfiguration.

The automatic DC and AV calibration process is shown in Fig. 47. We can observe in Fig. 47(a,b) that the calibration system generates a ramp from 0 to 3 V during 220 ms, due the gain of the control PZT (0.18 rad/V) and considering the gain given by the linear amplifier, this voltage amplitude corresponds to 6.2 rad of phase displacement. Then, the system takes between 200 and 500 ms to dynamically reconfigure the FPGA, switching to the nonlinear control hardware configuration. It is important to note that, this time corresponds to the calibration process, and the settling time remains less than 50 ms.

4.4.2 Low-Pass Filter

In order to keep the operation point of the interferometer in quadrature, the resulting signal must have only the low frequencies components. For this task, a low-pass filter must be applied. Since the frequency band of the phase drift is lower than 20 Hz, and the signal applied to the phase modulator of interferometer sensor arm is generally on the order of kilohertz, there is no need for the filter to have a sharp frequency response. It is also desirable for the delay introduced by the filter to be the shortest possible. Therefore, we chose an IIR (Infinite Impulse Response) first-order Butterworth low-pass filter. In this work, we used the bilinear transformation methodology to design the IIR digital filters (PARKS; BURRUS, 1987). The Laplace transfer function for a continuous-time first-order Butterworth low-pass filter is of the form:

$$H(s) = \frac{\Omega_c}{s + \Omega_c}; \tag{127}$$

The parameter Ω_c is the cutoff frequency in radians per second. Applying the bilinear transform we have:

$$s = \frac{2(1 - z^{-1})}{T(1 + z^{-1})}; \tag{128}$$

Figure 47 – Automatic DC and AV calibration process (a) in a controlled environmental and (b) in a harsh environmental.

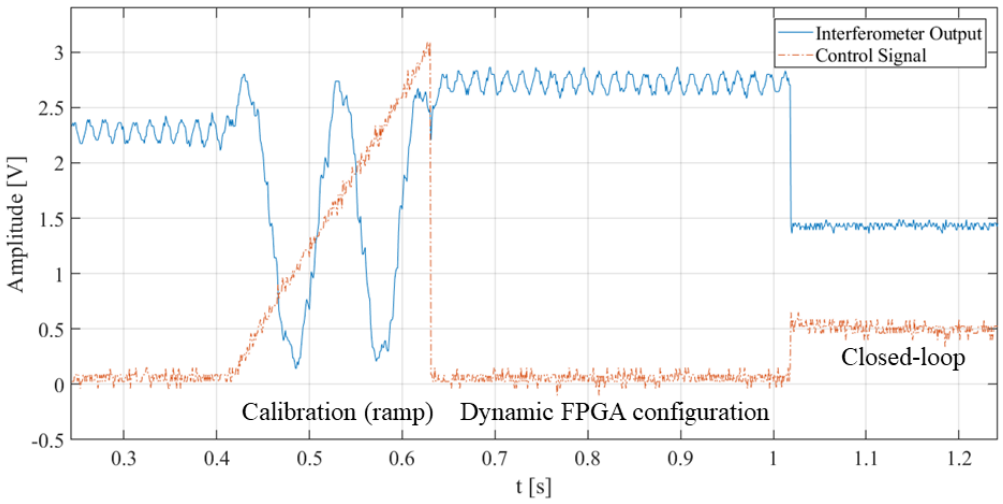

(a)

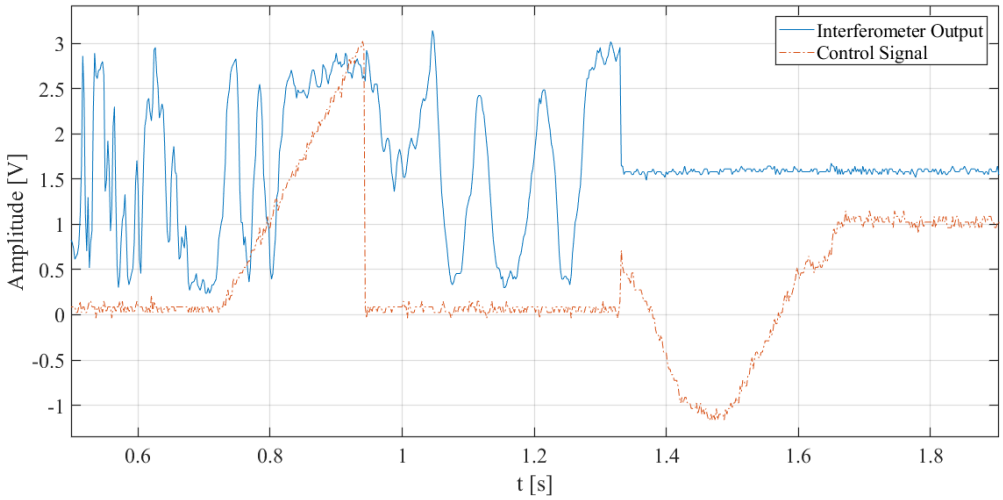

(b)

Source: From author.

$$H(z) = \frac{\Omega_c}{\frac{2(1-z^{-1})}{T(1+z^{-1})} + \Omega_c}; \tag{129}$$

$$H(z) = \frac{\Omega_c T(1+z^{-1})}{(\Omega_c T+2) + (\Omega_c T-2)z^{-}1}; \tag{130}$$

$$H(z) = \frac{\frac{\Omega_c T}{(\Omega_c T+2)}(1+z^{-1})}{1 + \frac{(\Omega_c T-2)}{(\Omega_c T+2)}z^{-}1}. \tag{131}$$

Substituting $\Omega_c = 40\pi$ and the sampling period $T = 10^{-5}$ s leads to:

$$H(z) = \frac{0.000627924 + 0.000627924z^{-}1}{1 - 0.998744z^{-}1} \tag{132}$$

The respective difference equation for the designed filter is:

$$y[n] = 0.998744y[n-1] + 0.000627924x[n] + 0.000627924x[n-1] \tag{133}$$

4.4.3 Simpson Integrator

Many authors have shown different strategies to solve the problem of numerical integration, that is, to estimate the number $S(f) = \int_a^b f(x)dx$, with $[a, b]$ a finite closed interval, in discrete systems (AL-ALAOUI, 1993; AL-ALAOUI, 2011; BIHAN, 1993; PAPAMARKOS; CHAMZAS, 1996; TSENG, 2007).

In case of spurious signal, since there isn't an anti-derivative in terms of known functions, we use methods which approximates the finite integral. Two of the most popular methods for approximating the evaluation of definite integrals are the Trapezoidal and Simpson's Rules (AL-ALAOUI, 2011; DAVIS; RABINOWITZ, 2007).

We employed the Simpson's rule to the integrator which was implemented in FPGA for the nonlinear control system. This method approximates a definite integral by using quadratic polynomials instead of straight lines segments used in the trapezoidal rule.

As shown in Al-Alaoui (2011), the Z-transform for the Simpson's, trapezoidal and ideal integrator rule are given by:

$$H_s(z) = \frac{Y(z)}{X(z)} = \frac{h}{3}\frac{(1 + 4z^{-1} + z^{-2})}{(1 - z^{-2})} \tag{134}$$

$$H_t(z) = \frac{h(1 + z^{-1})}{2(1 - z^{-1})} \tag{135}$$

$$H_{id}(z) = \frac{1}{1 - z^{-1}} \tag{136}$$

In Fig. 48 the frequency response magnitude of the integrator using Simpson's rule is compared to an integrator with trapezoidal rule and with ideal integrator.

We can see that, for frequencies until half of the normalized frequency, the Simpson's rule gives a better approximation to the ideal integrator than the trapezoidal rule. This result agrees with (AL-ALAOUI, 2011), therefore, it justifies the choice used in this work.

Figure 48 – Comparison of frequency response magnitudes between ideal, trapezoidal and Simpson Integrators

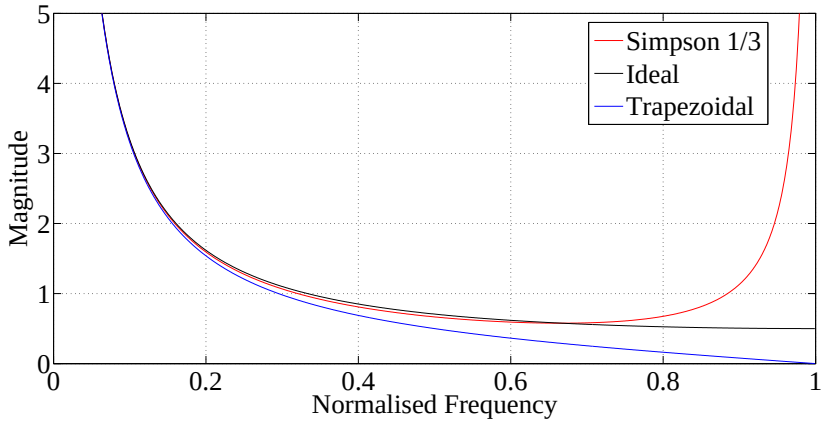

Source: From author.

4.4.4 Anti-Windup

Control systems with actuators subject to saturation may present an undesirable behavior, especially for controllers with integral action. When the actuator reaches the saturation level, the feedback loop doesn't act properly and the calculated values of the regulator may then drift to undesirable values. This phenomenon is referred to as windup. It was first noticed during practical implementations of PI and PID controllers, and many authors described this problem and proposed ways to overcome it (ASTROM; RUNDQWIST, 1989; BERGER; GUTMAN, 2016; KAPOOR; TEEL; DAOUTIDIS, 1998; PENG; VRANCIC; HANUS, 1996; RAN; WANG; DONG, 2016; TURNER; SOFRONY; HERRMANN, 2016; ZHENG; KOTHARE; MORARI, 1994).

The output of myRIO-1900 embedded platform is limited to the range of ±10 V. Therefore, considering the interferometer subject to a spurious disturbance high enough to make the analog output reach saturation, without any anti-windup strategy, the integrator would keep increasing the internally calculated value. Meanwhile the output value would stay fixed at the saturation level and, after the end of disturbance it would take a long time for the integrator output to reach again values in the range of ±10 V.

Once the integrator was implemented digitally, and according to (ASTROM; RUNDQWIST, 1989), a simple approach to overcome the windup problem is to stop the integration whenever the output reaches saturation levels. Therefore, a structure comprising a case condition loop was implemented in cascade with Simpson integrator, preventing windup phenomenon. It is noteworthy that, in this case, the controller does not need a reset system.

4.4.5 Transferring data between FPGA and Real Time Processor

As can be seen in the diagram block of myRIO-1900 embedded platform in Fig. 46, the nonvolatile memory communicates with the real-time processor of Xilinx Zynq-7010 (comprising a dual-core Arm cortex A9 microprocessor). Therefore, in order to log the acquired data of control signal and photodetector output signal, from FPGA, the data must be transferred to real-time processor. A recommended approach to transfer a large amount of sequential data is through a Target to Host FIFO (First-In First-Out).

FIFO is a type of structure which holds the elements and provides access to them in the receiving order, in such a way that the first element to be written will be the first read element.

It is essential to synchronize the rate that FPGA writes data into DMA FIFO and the rate that real-time processor retrieves the data, otherwise an unexpected behavior may occur and samples may be lost. First, considering that five analog channels must be sampled at rate of 10 kHz, in each execution of the sampling routine, five elements will be written.

Target to Host FIFO comprises two buffers and a DMA Channel to send data between them. The first buffer is allocated in the FPGA and therefore must be configured in the project. The second buffer is allocated in the Host and is configured in the VI (virtual instrument) executed for the real-time processor, through a structure called Invoke Node. The FPGA buffer is configured with 1023 position elements and it will retain any incoming data before it is transmitted to host buffer. The buffer in the host side will receive and store the data transmitted for the DMA channel until it is read out for the host VI. This buffer is configured to have 10000 element positions or twice the FPGA buffer capacity, whichever is greater (**??**).

Considering five channels being sampled at the rate of 10 KHz, in one second the FPGA will transmit 50000 samples. The host VI buffer is configured with 10000 element positions and is configured to read 2500 elements every 0.05 seconds, giving therefore 50000 samples per second.

5 Experimental Results

In this chapter, the experimental results regarding the application of the nonlinear control technique in the bulk Michelson and all-fiber Mach-Zehnder interferometer are presented. The experimental phase plane was acquired experimentally and compared with simulation curves, in order to validate the model. After that, the controlled interferometers were tested in dynamic operation, first in the characterization of the optical fiber response to temperature, characterization of a piezoelectric actuator, and to detect ultrasound waves directly from the surface of a sample.

5.1 Nonlinear control system evaluation

In this section, it is presented the evaluation of the proposed nonlinear control system, that comprises the study of perturbation supression, the experimental phase plane, a comparative analysis between the analog and digital control systems, as well as, the sign and sigmoid function approaches.

5.1.1 Supression of 120 Hz

This test was performed in the bulk speckle interferometer presented in Section 4.1.1. As seen, this configuration has a low AV parameter and consequently a low SNR (signal to noise ratio). This characteristic was observed during the experiments with ultrasound frequencies, due the low gain of the photodetector to this range of frequency. Hence, it was observed that the output signal of the interferometer had an interference at the frequency 120 Hz. This effect can be clearly observed in Fig. 49(a) at the output signal, and the respective component at 120 Hz frequency in the spectrum of the output signal in Fig. 49(b).

To overcome this issue, the cutoff frequency of the low pass filter (LPF) was set at 1000 Hz, a far greater value than the interference, in such way that it is suppressed by the control system. It is noteworthy that the value of the gain γ must increase proportionally with the frequency of ϕ_0 in order to keep the stability on the closed loop. For example, assuming that ϕ_0 is a sinusoidal signal which must be suppressed, $\phi_0 = A\sin(\omega t)$, then $\dot{\phi}_0 = \omega A\cos(\omega t)$, as seen in Section 3.3.4. The frequency ω is multiplied by the amplitude A, significantly increasing the value of the gain (γ), required value to compensate this disturbance, as stated by the control condition $\gamma > |\dot{\phi}_0|$.

The control system was tested to suppress the disturbance signal that comprises the environmental disturbance, the interference at 120 Hz and a sinusoidal signal with

Figure 49 – Interference at the frequency 120 Hz in the output signal and its spectrum.

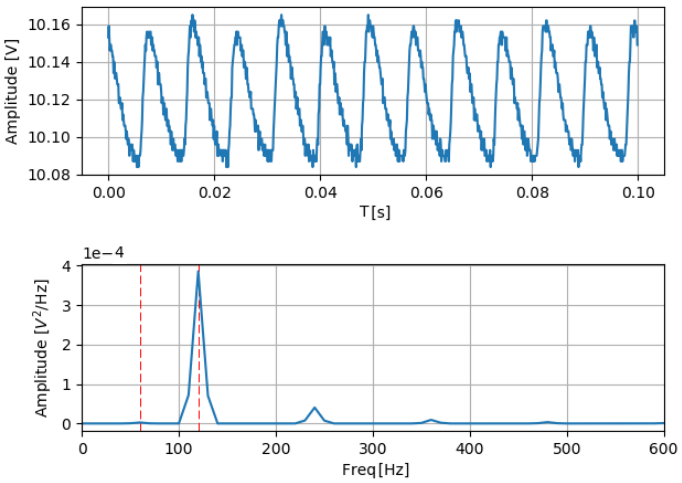

Source: From author.

amplitude 2 V and 3 Hz frequency. In Fig. 50, the interferometer output signal is shown as the top black line, while the control signal is shown as the bottom red line. The open loop operation is shown in Fig. 50(a), while the closed loop operation is shown in Fig. 50(b). As can be observed, in open loop operation, the interferometer output signal (Fig. 50(a), top) presents fading, i.e., the operation point is out of quadrature and the output signal is superimposed by the disturbances signal. Moreover, the control signal is zero (turned off) (Fig. 50(a), bottom). On the other hand, in closed loop operation, the interferometer output signal (Fig. 50(b), top) does not present fading and the disturbance signal was compensated, as we can observe in the control signal (Fig. 50(b), bottom).

Besides that, the output and the control signal spectra were acquired for open loop and closed loop operation to guarantee that the control system suppressed the disturbance. We can observe in Fig. 51(a) that in open loop operation (red signal), the spectrum has higher components in 3 and 120 Hz, and the control signal in closed loop operation (black signal) has the same characteristic, showing that this components are being compensated by the controller. This effect in output signal in closed loop operation (black signal) can be observed in Fig. 51(b) in which the components in 3 and 120 Hz were suppressed.

The higher the gain, better suppressed will be the disturbance, as shown in Fig. 52 in which we can observe the 120 Hz interference suppression with three different gains. It is important to note that the signal of interest is in the ultrasound frequency (above 20 kHz), making possible to increase the cutoff frequency of the low pass filter without deteriorate the output signal, as shown in Section 3.3.2.

Figure 50 – Interferometer output signal (top) and control signal (bottom) in (a) open loop and (b) closed loop operation

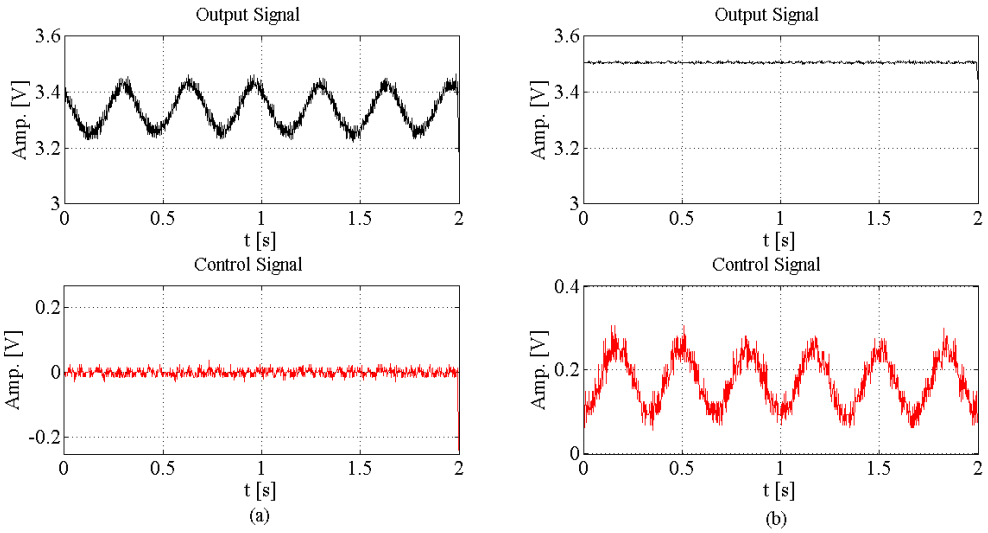

Source: From author.

Figure 51 – Comparative analysis in (a) open loop operation (red signal) and the control signal in closed loop operation (black signal), and (b) open loop operation (red signal) and the output signal in closed loop operation (black signal).

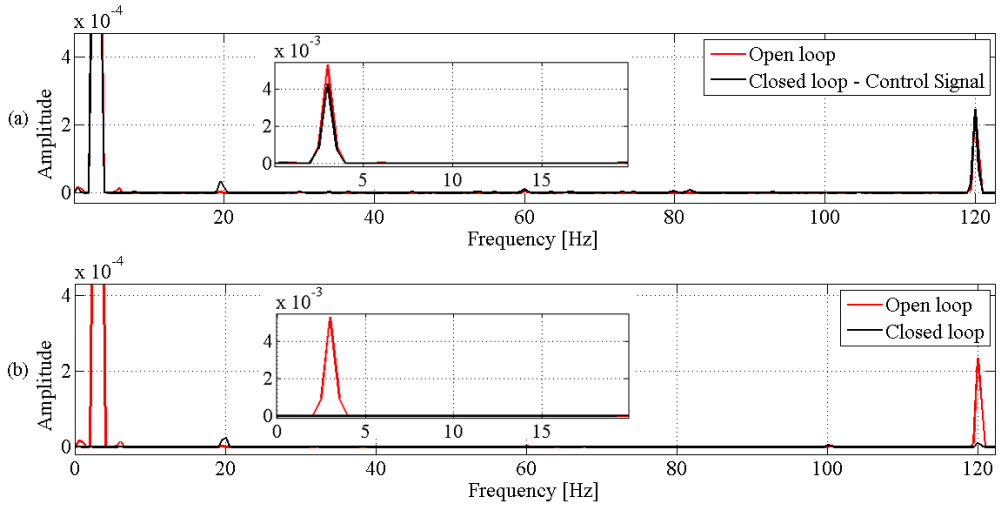

Source: From author.

5.1.2 Experimental phase-plane

In order to obtain the experimental phase-plane, the state variable used was named $\overline{x}_1$ and is located in the integrator circuit output. This variable was chosen because the state variable x_1 is not accessible in the implemented circuit plant. The state variable $\overline{x}_1$ is proportional to x_1, since the equilibrium point is ($x_1 = \pi/2$, $x_2 = 0$), $x_1 = \overline{x}_1 + \phi_o$,

Figure 52 – Interference suppression with three different gains

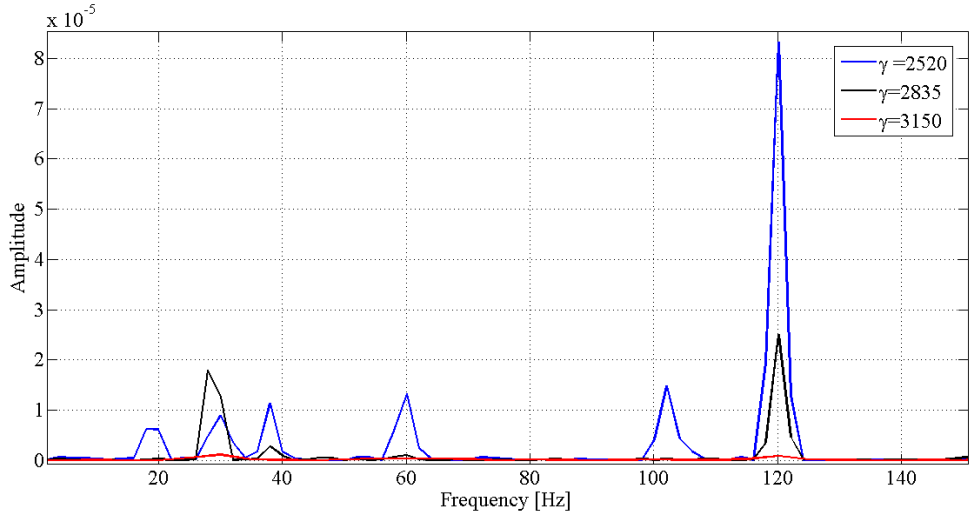

Source: From author.

i.e., in terms of $\overline{x}_1$, the equilibrium point is $\overline{x}_1 = \pi/2 - \phi_o$, which corresponds to the voltage required to vanish the fading and take the system input to the defined equilibrium point (quadrature). It is noteworthy that, from variable $\overline{x}_1$, it is possible to measure ϕ_o in real-time.

The signals used to obtain the phase-plane $\overline{x}_1$ and x_2 for gain γ equal to 5.01, 25.77 (bulk Michelson interferometer with analog control) and 1176 (for all-fiber Mach-Zehnder interferometer with digital controller) are shown in Fig. 53. It can be observed that, the higher the gain γ of the system, the faster the state $\overline{x}_1$ and x_2 converges to the equilibrium point, and more robust the system will be. Consequently, the overshoot will be greater and the settling time, shorter, as predicted in Chapter 3.

Therefore, the experimental phase-plane was first obtained in the bulk Michelson interferometer with $\gamma = 54$ implemented in analog approach, showed in Section 4.1, by plotting $x_2 \times \overline{x}_1$, as shown in Fig. 54(a), where the state tracks a trajectory from the left to the right mostly over the positive semi-plane, $x_2 > 0$ and ends at the equilibrium point. In Fig. 54(b), the state tracks a trajectory from the right to the left, mostly over the negative semi-plane, $x_2 < 0$, and ends at the equilibrium point.

Then, the experimental trials where performed in the all-fiber Mach-Zehnder interferometer setting the same values of parameters ($\gamma = 1176\ rad/V$, $\epsilon = 0.9$) in the digital implementation using the sigmoid approach, and the acquired experimental phase plan is showed in Fig.55 (a) and (b).

Thus, one can observe that the state trajectories are in agreement with the theoretical phase-plane, shown in Fig. 18 and Fig.19, always converging to the stable equilibrium

Figure 53 – Signals $\overline{x}_1$ and x_2 for gain γ (a) 5.01, (b) 25.77 and (c) 1176.

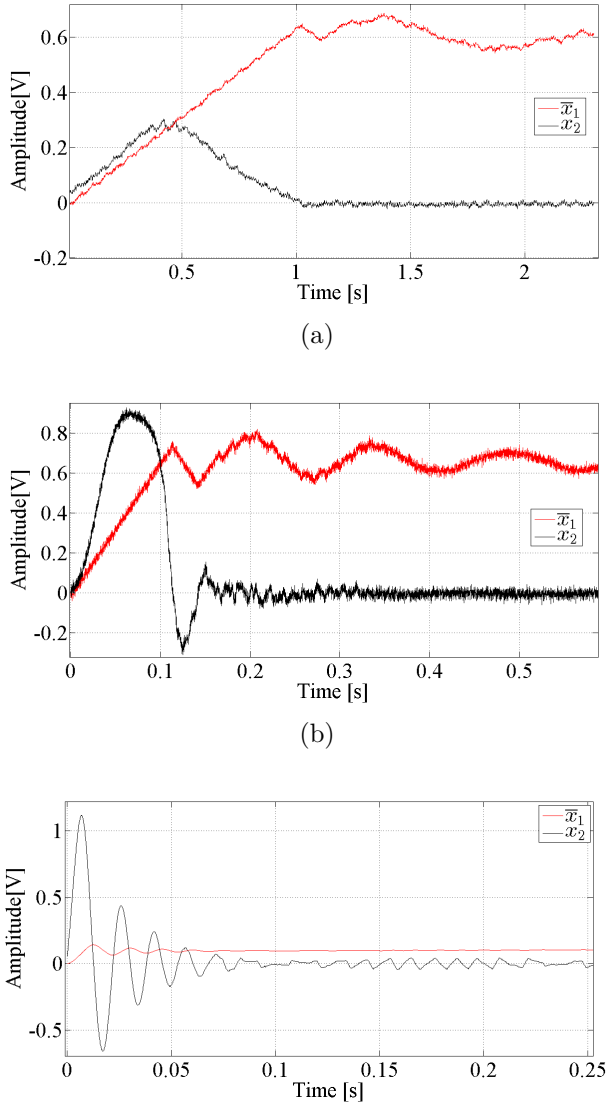

(a)

(b)

(c)

Source: From author.

point as $t \to \infty$. In Fig. 54, one can observe that $\overline{x}_1$ does converges to the voltage required to compensate ϕ_o and it takes the state x_1 to a stable equilibrium point (quadrature).

One can see that this two equilibrium points have qualitative behavior of stable foci and the trajectories evolve in a clockwise decreasing spiral. The experimental phase planes showed great similarity with the theoretical one, validating the implemented system. For both acquired phase plan, the trajectories evolve in a clockwise decreasing spiral.

Therefore, the experimental phase-plane was obtained in the all-fiber Mach-Zehnder interferometer with digital controller for three different gains, with sigmoid functions ($\gamma_1 = 2520$, $\gamma_2 = 2835$ and $\gamma_3 = 3150$ for $\epsilon = 0.9$), as shown in Fig. 56, where we have the phase plane. One can observe that the amplitude of the chattering increases for higher

Figure 54 – Experimental phase-plane obtained with the bulk Michelson interferometer with analog control system for different initial conditions.

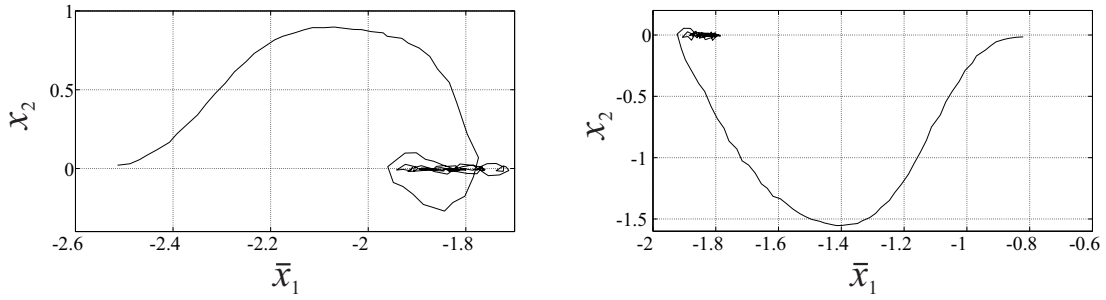

(a) (b)

Source: From author.

Figure 55 – Experimental phase planes obtained with all-fiber Mach-Zehnder interferometer with digital controller for $\gamma = 1176\ rad/V$, $\epsilon = 0.9$.

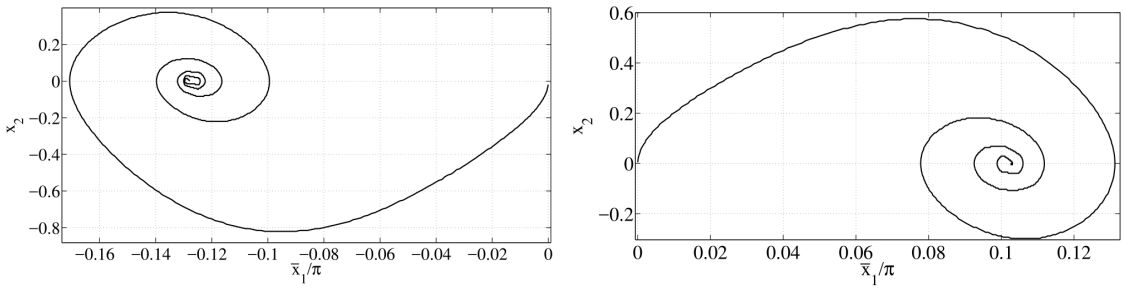

(a) (b)

Source: From author.

gains.

By analyzing Fig. 56, it is possible to see that the trajectory in phase plane only will cross the equilibrium point when $x_1 = \pi/2$ and $x_2 = 0$ at the same time. In the practical phase plane, shown in Fig. 56, this behavior does not occur because of the chattering effect. However, if the control condition($\gamma > |\dot{\phi}_0|$) is achieved, the stability is guaranteed, although there is an oscillation in the output signal.

Besides that, the chattering effect can be observed in the output signal, as shown in Fig. 57 for three different gains, with sigmoid functions ($\gamma_1 = 2520$, $\gamma_2 = 2835$ and $\gamma_3 = 3150$ for $\epsilon = 0.9$). Again, one can observe that the chattering amplitude increases for higher gains.

5.1.3 The use of the sigmoid approach

As presented in Section 3.3.4, the chattering effect becomes a drawback when we have a high closed-loop gain ($\gamma > 100$). The experimental results for the closed-loop

Figure 56 – Practical phase-plane obtained with different gains. (a)$\gamma_1 = 2520$, (b)$\gamma_2 = 2835$ and (c)$\gamma_3 = 3150$.

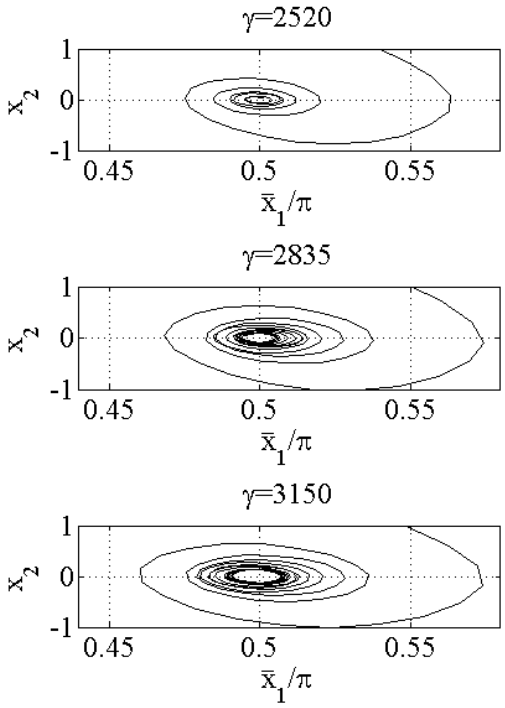

Source: From author.

operation with sign ($\gamma = 1176$) and sigmoid functions ($\gamma = 1176$ and $\epsilon = 0.9$) using the bulk Michelson interferometer with digital control are presented in Fig. 58. In this figure, the effect in the interferometer output signal due the sigmoid function and its advantages over the sign function on the system can be clearly observed. One can observe that the output signal for the sign function (red line) is disturbed by the chattering phenomenon causing distortion due the nonlinear characteristic of the interferometric system, oscillating around the equilibrium point. On the other hand, when the system operates with the sigmoid function (black line), this oscillation is heavily attenuated, smoothing the behavior of the system, and decreasing the chattering for the same gain value.

Besides that, the sigmoid effect can be observed in the phase plane. One can observe in Fig. 59 that the system converges to the equilibrium point ($x_1 = \pi/2, x_2 = 0$) with an abrupt change when the system state crosses the axis $x_2 = 0$, by using the sign function (Fig. 59(a)). On the other hand, the system has a smooth behavior for the sigmoid function (Fig. 59(b)). Consequently, the chattering effect observed is shorter for the sigmoid function.

Figure 57 – Output signal with chattering for (a)$\gamma_1 = 2520$, (b)$\gamma_2 = 2835$ and (c)$\gamma_3 = 3150$.

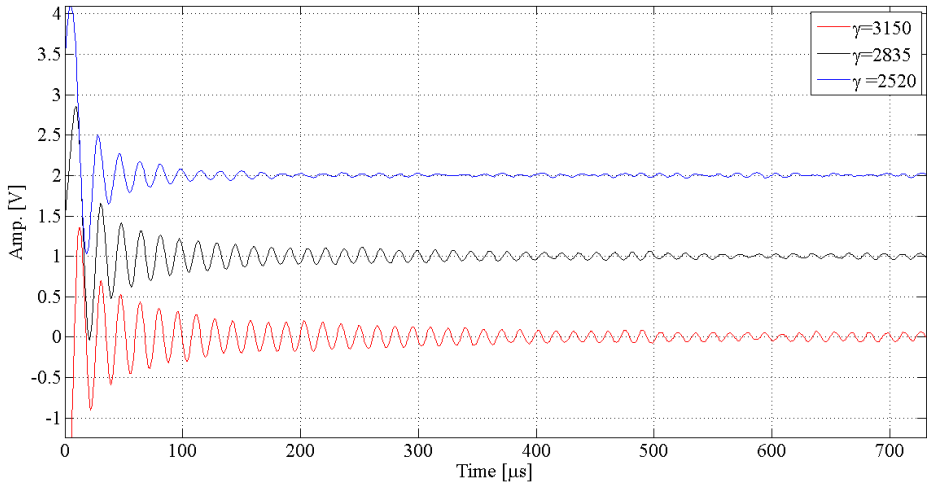

Source: From author.

Figure 58 – Comparative analysis of the interferometer output signal using the bulk Michelson interferometer with digital control for sign function in red and sigmoid function in black.

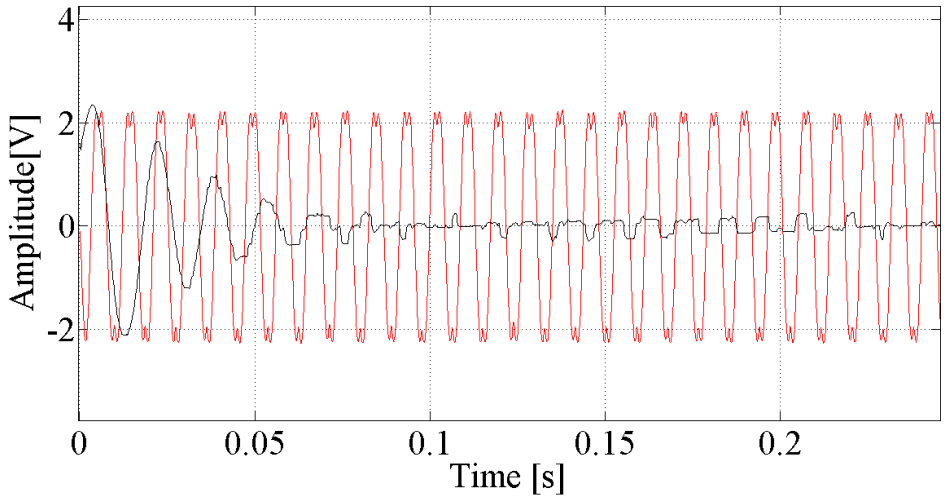

Source: From author.

5.2 Zero input signal

In the next experiment, the speckle interferometer, shown in Section 4.1.1, starts with the nonlinear control system turned off (open loop operation) and without signal of interest ($\Delta\phi(t) = 0$). Thus, it can be seen in the first 10 seconds of Fig. 60, that the interferometer output signal (top signal, in blue) presents random oscillations generated by spurious environmental disturbances superimposed by the 120 Hz interference (ϕ_0 spurious

Figure 59 – Phase plane comparative analysis for $\gamma = 1176$. (a) Sign and (b) sigmoid function with $\epsilon = 0.9$.

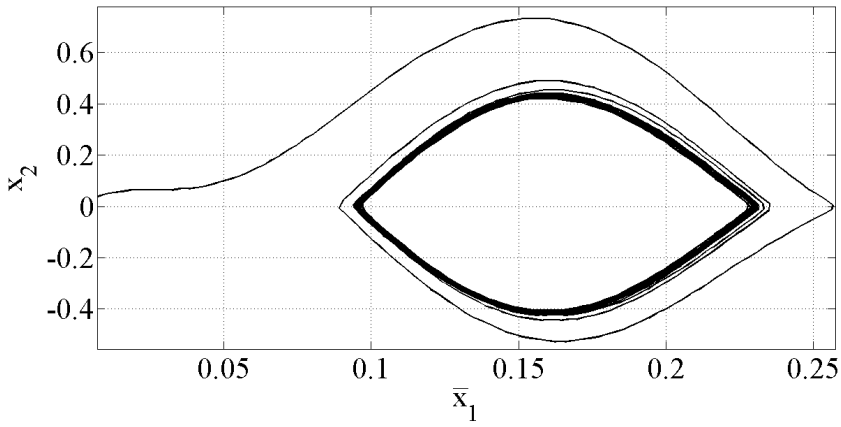

(a)

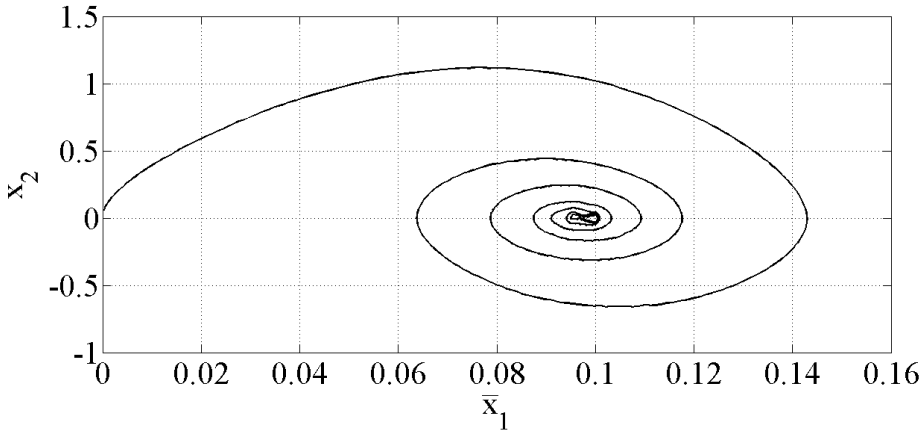

(b)

Source: From author.

variation). Moreover, the control signal (bottom signal, in black) keeps constant, i.e., the control is not actuating. However, after turning the nonlinear control system on (closed loop operation), after 10 seconds, and keeping the input signal null ($\Delta\phi = 0$), the output signal in Fig. 60 remains stabilized in a constant value, which corresponds to the parameter A from Eq. 16, while the control signal starts to actuate.

This result shows that the nonlinear control system operates properly, effectively removing the spurious disturbances from the output signal, even for zero input signal. This feature is important to some interferometer applications, e.g. laser ultrasonics, in which the system need to stay controlled with zero input signal until the ultrasonic pulse occurs.

Figure 60 – Interferometer output signal (top) and sign function (bottom), before and after turning on the nonlinear control system.

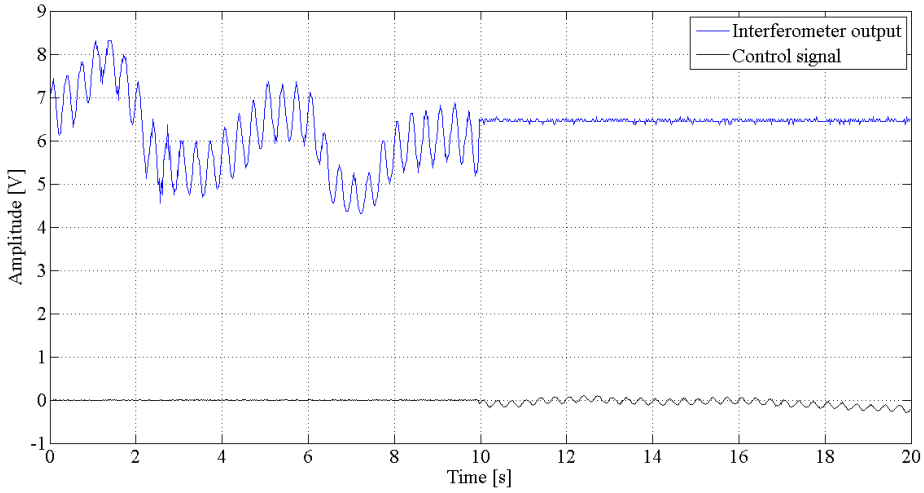

Source: From author.

5.3 Arbitrary signal detection

In this section, we check if the interferometer (bulk Michelson interferometer) with the analog nonlinear control system works properly even for an arbitrary signal at the input. As shown in Fig. 61, the input signal, applied to the piezoelectric actuator (sensor arm) is on the top (solid blue line) and the interferometer output signal on the bottom (dashed red line). Regarding the interferometer in open loop operation, the output signal presents fading and does not represent the input displacement, as shown in Fig. 62(a). On the other hand, once again, when the closed loop operation actuates, the interferometer output signal is in accordance with the displacement imposed by the piezoelectric actuator, as shown in Fig. 62(b). In this case, the input signal was shifted by 180° (on the oscilloscope) to provide a better comparison view between the input and output signals.

5.4 Sinusoidal signal detection

Since the control system was working properly, the next step was to apply a sinusoidal signal to the piezoelectric actuator (in the sensor arm) using the bulk Michelson interferometer with analog controller and verify if the interferometer with the nonlinear control system would be able to measure the corresponding displacement, and suppress the spurious signals. In this way, to generate the $\Delta\phi(t)$, we applied to the PZT under evaluation a sinusoidal input signal with peak voltage of 17.2 V and frequency of 1 kHz. In Fig. 62, the input signal is shown as the top solid blue line, while the interferometer output signal is shown as the bottom dashed red line. The sign function is shown in the

Figure 61 – Arbitrary displacement detected by the interferometer. Input on the top (solid blue line) and output on the bottom (dashed red line). (a) Open loop operation. (b) Closed loop operation (output shifted by 180°).

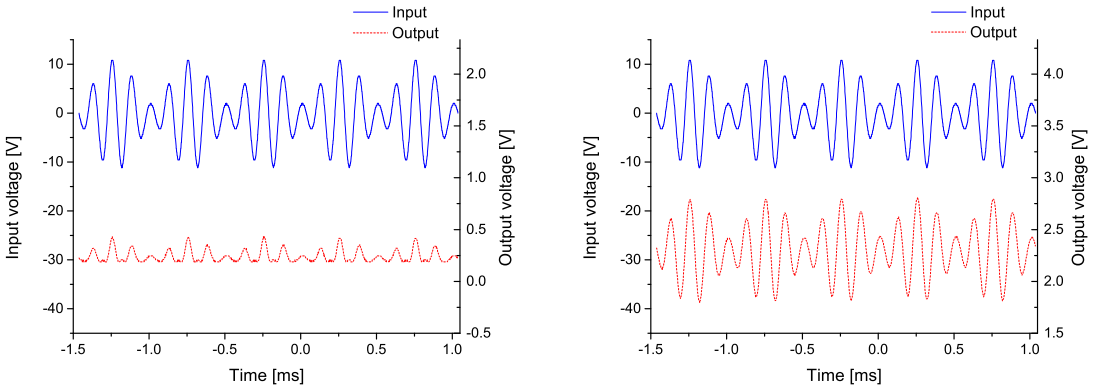

(a) (b)

Source: From author.

bottom graphic, as a solid black line. The open loop operation is shown in Fig. 62(a), while the closed loop operation is shown in Fig. 62(b).

Figure 62 – Sinusoidal displacement detected by the interferometer. Input voltage (solid blue line), output voltage (dashed red line), and sign function on bottom (solid black line). (a) Open loop operation. (b) Closed loop operation.

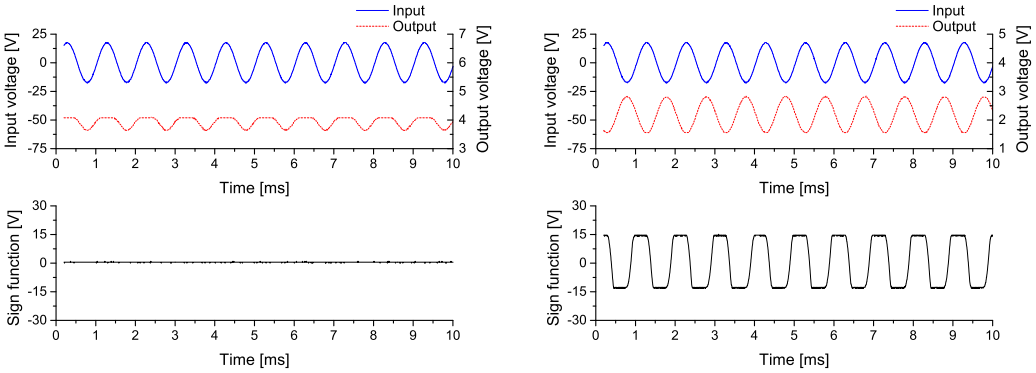

(a) (b)

Source: From author.

As can be observed, in open loop operation (Fig. 62)(a), the interferometer output signal presents fading, i.e., the operation point is out of quadrature and the sinusoidal displacement was not properly recovered. On the other hand, in closed loop operation (Fig. 62)(b), the interferometer output signal does not present fading and the sinusoidal signal was properly recovered. It is noteworthy that the closed loop output signal is shifted 180° in relation to the input signal.

5.4.1 Signal error correction using the first harmonic method

As shown in Section 3.3.2, the error in the closed-loop system only depends on well known parameters shown in (85), and decreases considerably as the frequency of the interest signal increases. This method can be applied in the correction of the error in the output signal in the practical system, aiming to increase the overall accuracy of the system.

Using the bulk Michelson interferometer with digital controller with gain $\gamma = 157.5$, we applied to the PZT under evaluation a sinusoidal input signal with peak voltage of 2.5 V and for different frequencies we obtain the amplitude of the signal interest and its correction, as shown in Table 5. It is important to note that, to correct the output signal in term of the error described in (85), we have to subtract the E_{FHM} of the $-\frac{v_{fb}}{AV}$ amplitude in radians.

Table 5 – Correction of the error in the output signal in a practical system by the first harmonic method.

Freq.$[Hz]$	$E_{FHM}[rad]$	**Output**$[V_p]$	**Output**$[rad]$	**Corrected output**$[rad]$
500	0.0638	2	0.561	0.4972
750	0.04255	1.594	0.447	0.4044
1000	0.03191	1.172	0.329	0.2971
1250	0.02553	1.156	0.324	0.2985
1500	0.02127	1.0625	0.2977	0.2764

It is important to point out that, through this method, we are minimizing and correcting any error that could be introduced by the feedback system. Therefore, highlighting the benefit and applicability of this method to improve the overall accuracy of the system.

5.5 Characterization of the optical fiber response to temperature

In this section, we present the study of single mode optical fiber response in radians to temperature in degrees. Also, we present the relation of fiber gain with temperature versus the fiber length. This is the first step aiming to use the temperature effect on optical fiber to control the interferometer, once this is a very good way to obtain very large gain with low length of fiber by applying control techniques actuating through the temperature, as will be seen in this section.

5.5.1 Peltier temperature measurement system

Firstly, in order to measure the temperature on Peltier, we use a Negative Temperature Coefficient (NTC) thermistor, in which its resistance decreases as the temperature increases, comprising an inversely proportional relationship. Then, it was necessary to

calibrate the NTC thermistor sensor (PS103J2). For this task, we expose the NTC to three different temperatures and compare with the temperature measured by a multimeter. From exposing the NTC sensor to a given temperature, we obtain a resistance and to derive a precise temperature value we need the Steinhart-Hart equation (STEINHART; HART, 1968):

$$\frac{1}{T_e} = A_S + B_S \ln(R) + C_S(\ln(R))^3 \tag{137}$$

where T_e is the temperature in Kelvin, R is the resistance in ohms at the temperature T_e and A_S, B_S and C_S are the Steinhart-Hart coefficients which are needed to be calibrated for each thermistor.

To find the Steinhart-Hart coefficients (A_S, B_S and C_S), we need at least three operating points. For this, we use three values of resistance data for three known temperatures obtained with the multimeter, as shown in Table 6.

Table 6 – Value of resistance for three different temperatures.

Temperature [K]	Resistance [ohms]
303.15	8056.61
318.15	4368.06
333.15	2487.69

The following equation was used to obtain the Steinhart-Hart coefficients:

$$\begin{bmatrix} 1 & \ln(R_1) & \ln^3(R_1) \\ 1 & \ln(R_2) & \ln^3(R_2) \\ 1 & \ln(R_3) & \ln^3(R_3) \end{bmatrix} \begin{bmatrix} A_S \\ B_S \\ C_S \end{bmatrix} = \begin{bmatrix} \frac{1}{T_{e1}} \\ \frac{1}{T_{e2}} \\ \frac{1}{T_{e3}} \end{bmatrix} \tag{138}$$

where R_1,R_2 and R_3 are values of resistance at the temperature T_{e1},T_{e2} and T_{e3}.

Thus, the coefficients obtained were: $A_S = 0.00006278504$, $B_S = 0.00041714959$ and $C_S = -0.00000067495$. The temperature measurement system with NTC thermistor (RT1) diagram is shown in Fig. 63.

A photocoupler (MOC3023) is used to uncouple the NTC measurement circuit and the circuit of activation with the power supply for the Peltier. This is necessary because when the Peltier cell is turned on, the current provided for the NTC varies, resulting in a wrong measurement in the NTC thermistor, once we consider the current constant on NTC to measure the resistance. The PWM1 signal is used like as a start bit, synchronizing the temperature measurement.

Figure 63 – Peltier temperature measurement system.

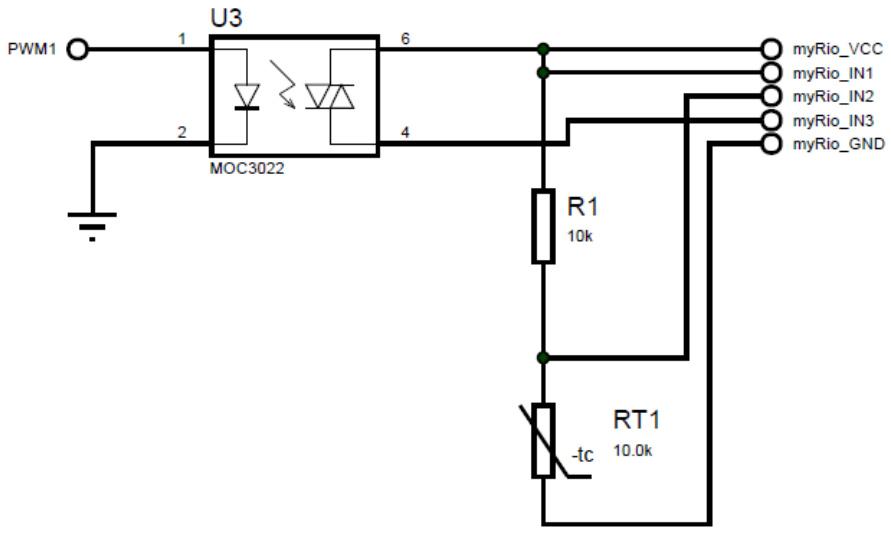

Source: From author.

5.5.2 Peltier temperature activation system

An H-bridge with four MOSFETs (FDD8424) was used to activate the Peltier Cell, as shown in Fig. 64. The FDD8424 contains a pair of N- and P-channel MOSFETs that can handle currents up to 20 A, requiring only one integrated circuit (IC) for each arm in the H-bridge. It is important to note that this circuit has an interlocking, provided by the BC546 transistor, preventing both sides of H-bridge from being triggered at the same time, causing a short-circuit and compromising the device.

The activation of the H-bridge is driven via two control signals, Enable 1 ($\overline{EN1}$) and Enable 2 ($\overline{EN2}$), that has active low logic. The enable pins are controlled by a PIC microcontroller, and their status were indicated by LEDs. In order to provide the maximum possible temperature variation to the Peltier, the input pin PWM1 was set to 100%, that is, logic level one.

5.5.3 Temperature variation for different lengths of optical fiber

Using the controlled interferometer shown in Section 4.2.4 with digital variable structure and sliding modes, the temperature is varied ten times from a 24°C (ambient temperature) to 58°C round trip (as shown in Fig. 65), and for three different lengths of fiber (40, 95 and 125 mm) to obtain the relation of fiber gain with temperature versus the fiber length. For this task, the Peltier activation system is turned on, causing the Peltier cell to warm up until it reached the desired temperature. Then, the system is turned off and the Peltier cell starts to cool down.

Figure 64 – Peltier temperature activation system.

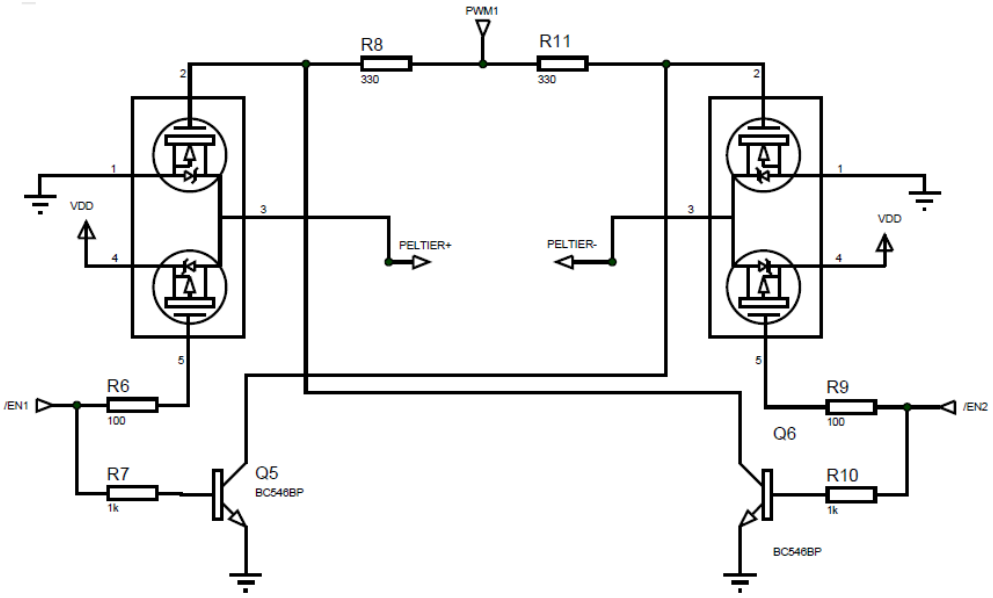

Source: From author.

It is important to note that, as the ambient perturbations (ϕ_0) and the signal temperature of interest are in the same frequency range, it is necessary to use statistical processes to detect the signal of interest. Also, due to the large numbers of tests, repeatability is used to guarantee the quality of the results. Besides that, we use the interferometer in a controlled environmental.

Then, since frequency of the temperature signal is below 20 Hz, hence, this signal is suppressed by the control system, as shown in Figs. 66, 67 and 68 for 40, 95 and 125 mm lengths of fiber, respectively. We can observe that the larger the fiber length the closer the control signal is to the temperature signal, and this occurs because the temperature disturbance will be much intense when compared to ambient variations. This effect can be clearly observed when we compare Figs. 66, 67 and 68.

Plotting the control signal (C [rad]) versus temperature (T [°C]), as shown in Fig. 69, we acquire the system response in [rad/°C]. Considering the linear region, shown in Fig. 69, we can obtain the slope of a straight line ($C = P1.T$) when the temperature increases and decreases with curve fitting, as shown in Tables 7 and 8, respectively.

It is important to note the linear relationship between the optical fiber response, in radians, and the temperature. Besides that, comparing the curve of the fiber response, in radians, with the temperature for each fiber length, as shown in Fig. 69, we note a hysteresis on the system, that can be related to the rate of time temperature variation and the slowness of heat dissipation to the ambient.

It is noteworthy that the linear coefficient (DC signal) presents a large error due the

Figure 65 – Temperature in Peltier measured with NTC sensor with (a) samples and (b) average and standard deviation.

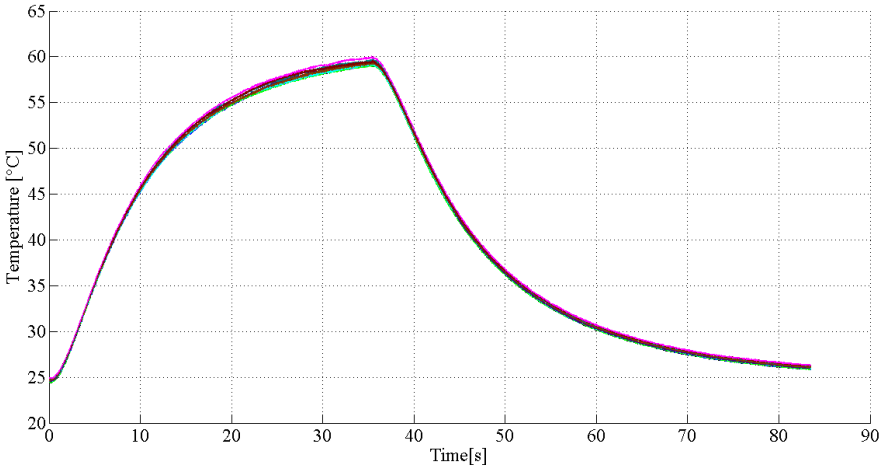

(a)

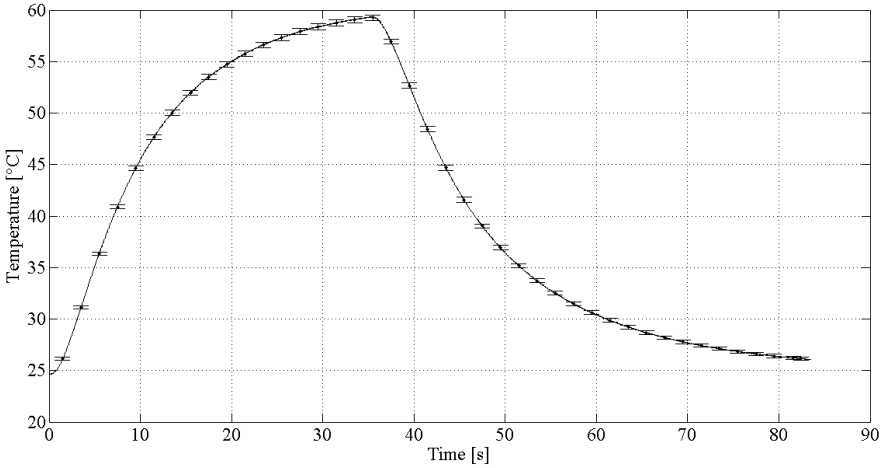

(b)

Source: From author.

Table 7 – Slope of a straight line (C=P1.T) increasing the temperature with the curve fitting.

Fiber length [mm]	P1 [rad/°C]	P1/Fiber length [rad/°C m]
40 ± 0.5	3.0145 ± 0.3871	0.07536 ± 0.0097
95 ± 0.5	5.6337 ± 0.6134	0.05930 ± 0.0007
125 ± 0.5	7.3854 ± 0.3671	0.05908 ± 0.0029

environmental perturbation. However, the interest in this work is the angular coefficient, which gives the slope of the curve and the gain of the optical fiber with temperature, and it presents a lower error, as will be seen.

Furthermore, we can obtain the relation of fiber gain with temperature [rad/°C]

Figure 66 – Control signal compensating the temperature variation for 40 mm with (a) samples and (b) average and standard deviation.

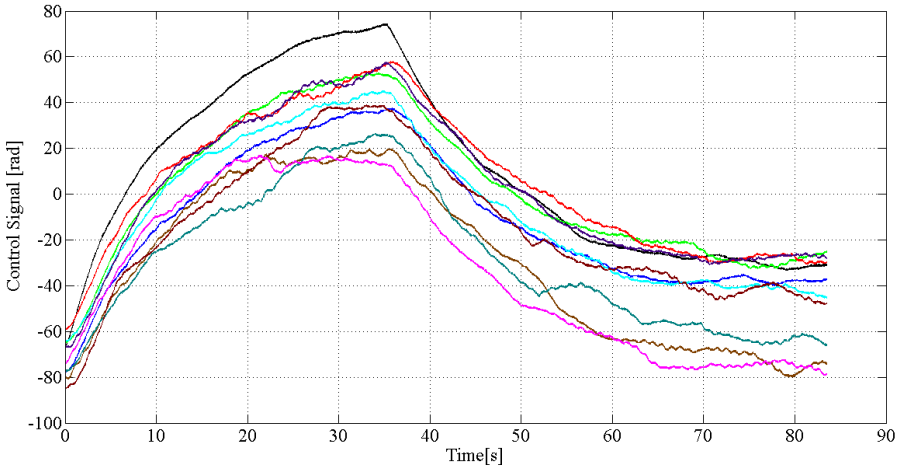

(a)

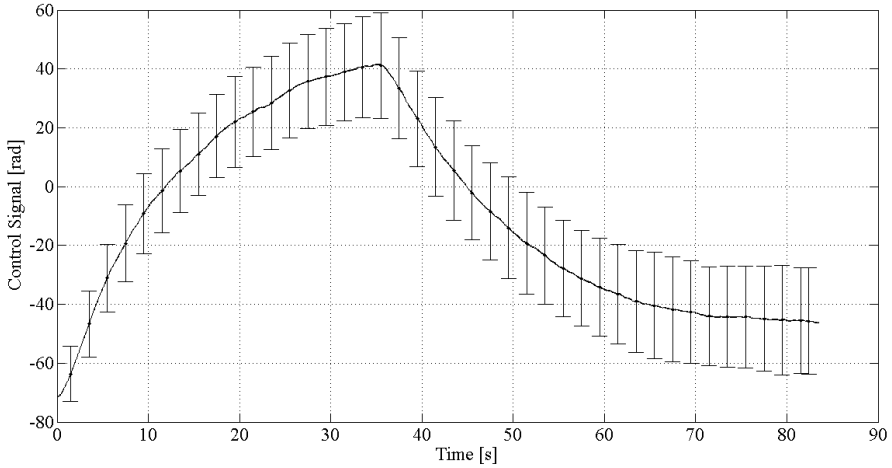

(b)

Source: From author.

Table 8 – Slope of a straight line (C=P1.T) decreasing the temperature with the curve fitting.

Fiber length [mm]	P1 [rad/°C]	P1/Fiber length [rad/°C m]
40 ± 0.5	2.4315 ± 0.2435	0.06078 ± 0.0061
95 ± 0.5	6.9111 ± 0.4028	0.07274 ± 0.0043
125 ± 0.5	8.2372 ± 0.369	0.06589 ± 0.0025

versus the fiber length. In this case, we observe that the fiber gain with temperature (G [rad/°C]) is linear with the optical fiber length (L [mm]), and its linear curve is $G = (0.06553 \pm 0.0043)L$, obtained through the rising and falling slopes of the fiber response curves in Fig. 69, which means that the optical fiber gains with temperature

Figure 67 – Control signal compensating the temperature variation for 95 mm with (a) samples and (b) average and standard deviation.

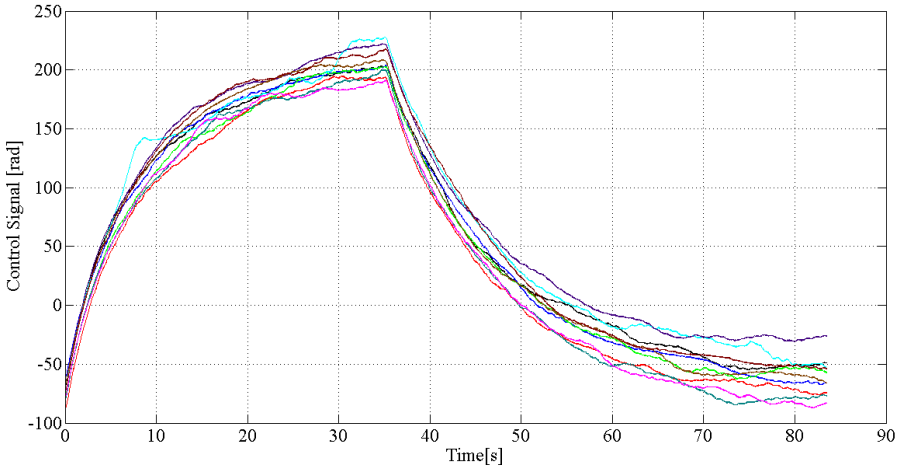

(a)

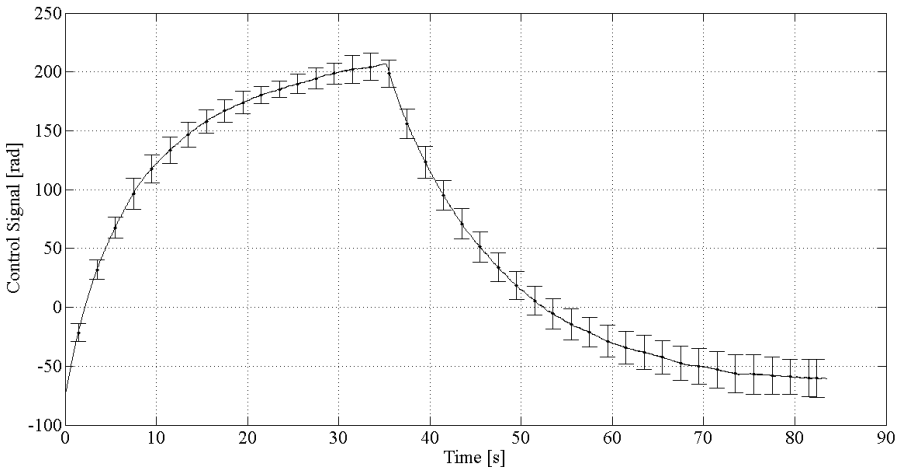

(b)

Source: From author.

varies (65.53 ± 4.3) rad/°C in one meter of heated fiber, i.e., (65.53 ± 4.3) rad/°Cm.

5.6 Piezoelectric actuators characterization

5.6.1 Multi-axis piezoelectric actuator characterization

Once we proved that the interferometer with the nonlinear control system works properly, we are concerned on the application of this device, for example, on the characterization of piezoelectric actuators. Therefore, the multi-axis piezoelectric actuator characterized in this work is of interest since it provides reduced displacements, corresponding to a phase variation smaller than $\pi/2$ rad, not enough to employ multi-fringe

Figure 68 – Control signal compensating the temperature variation for 125 mm with (a) samples and (b) average and standard deviation.

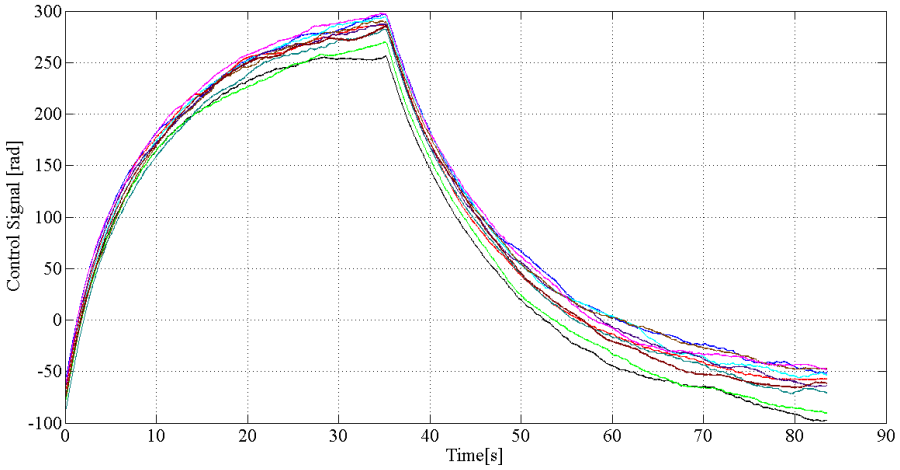

(a)

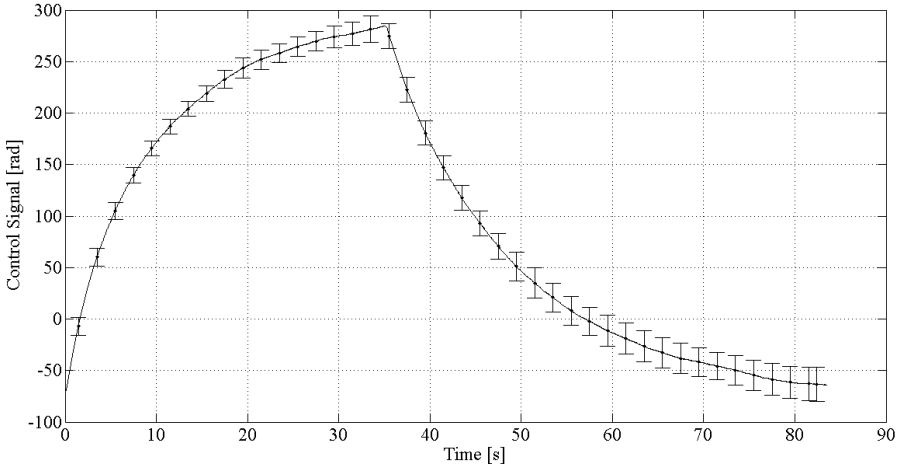

(b)

Source: From author.

demodulation methods (although, if necessary, the application of any phase unwrapping technique would solve such a problem). Therefore, the interferometer proposed in this work is suitable to evaluate this actuator design performance, since it can detect those reduced displacements.

The multi-axis piezoelectric actuator comprises two piezo-ceramics and an aluminum structure, as shown in Fig. 70, designed by a topological optimization method with finite elements method (CARBONARI; SILVA; NISHIWAKI, 2005). This structure was optimized such that each piezo-ceramic provides mechanically amplified displacement in one direction, i.e., one piezo-ceramic (PZT B1) provides displacement in the x direction, while the other (PZT B2), in the y direction. However, the actuator built in practice can

Figure 69 – Curve of fiber response in radians and the temperature for 40, 95 and 125 mm fiber length (a), and its linear region (b).

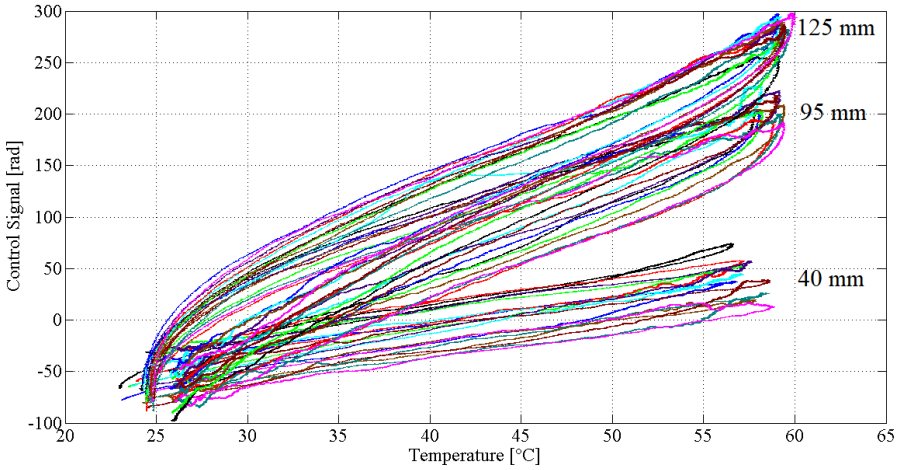

(a)

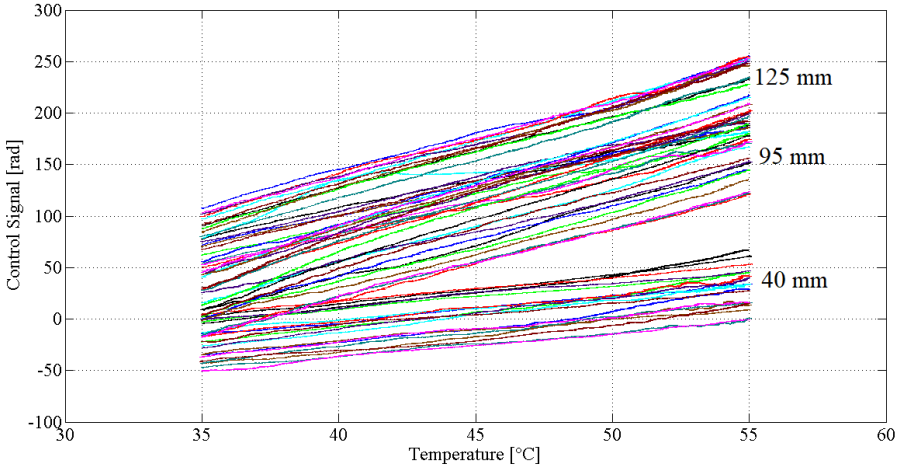

(b)

Source: From author.

generate displacements of two types: the direct one (PZT B1 causes a displacement in x, or PZT B2 causes a displacement in y) and the coupled one (PZT B1 causes a displacement in y, or PZT B2 causes a displacement in x).

The "piezoelectric actuator under evaluation" shown in the closed-loop Michelson interferometer shown in Fig. 26 was then replaced by the multi-axis piezoelectric actuator, while the "feedback piezoelectric actuator" was kept the same. Thus, the multi-axis piezoelectric actuator was characterized by measuring its frequency response and linearity (at a resonance frequency and at a frequency out of resonance), for direct and coupled displacements.

The frequency response curves were obtained from 100 Hz to 20 kHz, by applying

Figure 70 – Multi-axis piezoelectric actuator. (a) Top view. (b) Lateral view.

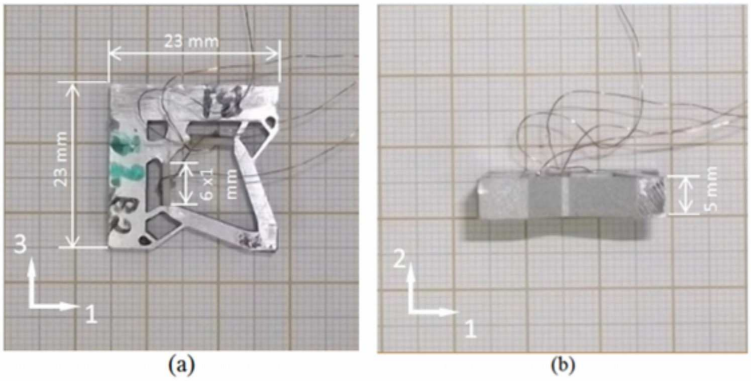

Source: From author.

sinusoidal signals to PZT B1 or to PZT B2 and measuring the direct or coupled displacements. This provides four different situations: i) PZT B1 direct displacement (x direction); ii) PZT B1 coupled displacement (y direction); iii) PZT B2 direct displacement (y direction); and iv) PZT B2 coupled displacement (x direction). The results are shown in Fig. 71, where the displacement was evaluated by $\Delta l(t) = \frac{\lambda}{4\pi}\Delta\phi(t)$. In Figs. 71(a) and 71(b) one can see a main resonance at 19.15 kHz, a secondary resonance followed by an anti-resonance at 12 kHz, and several micro-resonances around 8 kHz. This can also be readily seen from the phase graphics, Figs. 71(c) and 71(d).

One can observe that the coupling factor (ratio between the coupled and direct displacements) is higher in resonance frequencies and, in some cases, the coupled displacement can be as high than the direct one. Therefore, we emphasize the importance of measuring the resonance frequencies in actuators, in order to prevent unintended movements. In applications like sample positioning in an atomic force microscope, for example, an undesired displacement can cause permanent damage to the sample.

The linearity for the direct displacement (PZT B1) was acquired at two frequencies: 4.5 kHz and 19.3 kHz and the results are shown in Fig. 72.

It can be noted that the actuator presents a linear behavior at the frequency of 4.5 kHz, and the curve slope (also called linear length-to-voltage sensitivity) was calculated and equates to 38.6 nm/V (see Fig. 72(a)). On the other hand, at 19.3 kHz, an elliptical hysteresis curve was obtained (see Fig. 72(b)), with slope of 400.8 nm/V (about ten times bigger than the one acquired at 4.5 kHz). The hysteresis and the bigger slope can indicate the presence of a resonance around 19.3 kHz.

5.6.2 Piezoelectric actuator response at ultrasound frequencies

We already tested the nonlinear control system in the frequency range below 20kHz in (MARTIN et al., 2017a; MARTIN et al., 2017b). In this section, we are concerned in

Figure 71 – Frequency response for PZB B1 and B2. (a) Magnitude (PZT B1). (b) Magnitude (PZT B2). (c) Phase (PZT B1). (d) Phase (PZT B2).

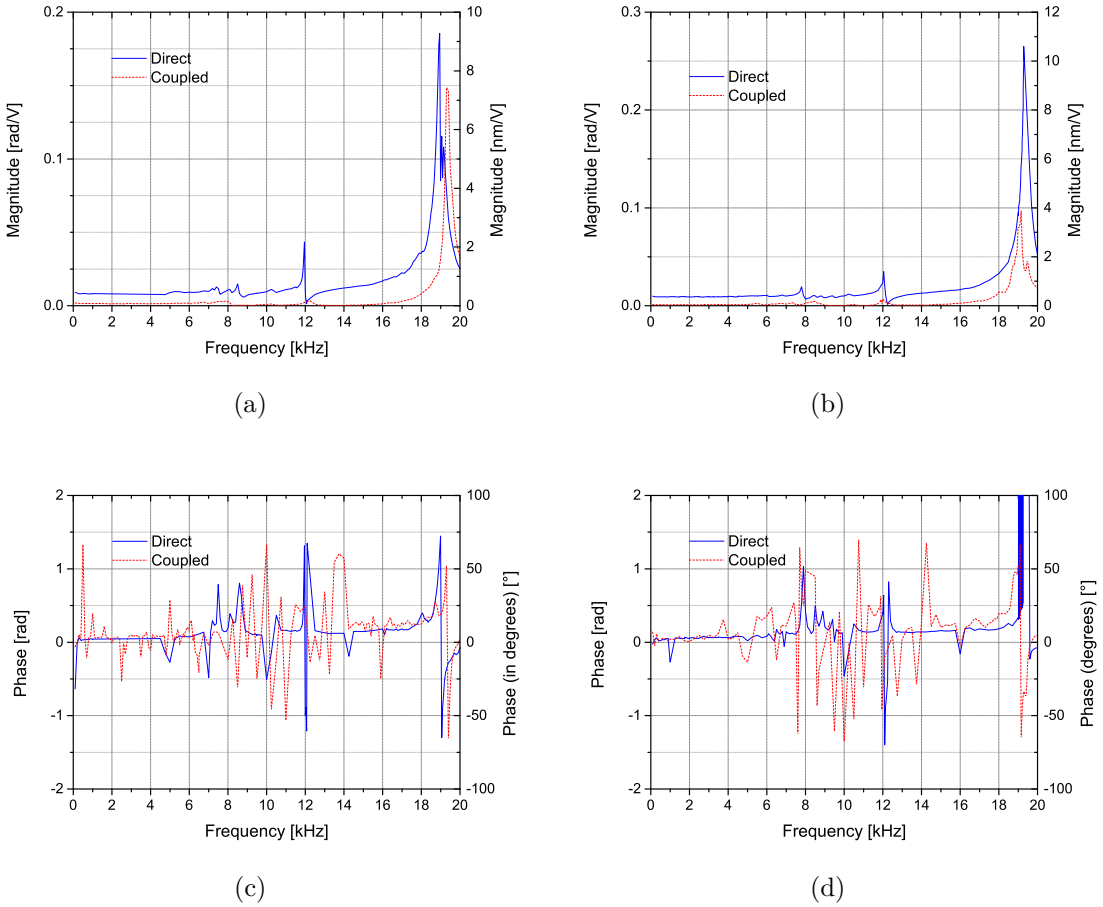

Source: From author.

the detection of ultrasonic frequencies. Once we proved that the interferometer with the nonlinear control system works properly, we are concerned on the application of this device, for example, on the characterization of a piezoelectric actuator at ultrasonic frequencies for well-behaved signals (sinusoidal). For this task, we use the bulk speckle Michelson interferometer described in Section 4.1.1 with the digital controller. Then, the piezoelectric actuator to be characterizes is without mirror.

The frequency response curves were obtained from 34 kHz to 1150 kHz, by applying sinusoidal signals to the piezoelectric actuator and measuring the displacements. The results are shown in Fig. 73, where the displacement was evaluated by $\Delta l(t) = \lambda/4\pi\Delta\phi(t)$. In Fig. 73 one can see a main resonance at 34 kHz and several microresonances between 95 kHz and 410 kHz.

The linearity curve of the transducer was acquired keeping the frequency on the resonance, i.e., 34 kHz, and the input voltage V_{input} was varied from 1 to 10 V (peak-to-peak voltage). The result is shown in Fig. 74. As can be observed on the graphic, the transducer

Figure 72 – Linearity of the actuator. (a) Linearity of the actuator at 4.5 kHz. (b) Hysteresis of actuator at 19.3 kHz.

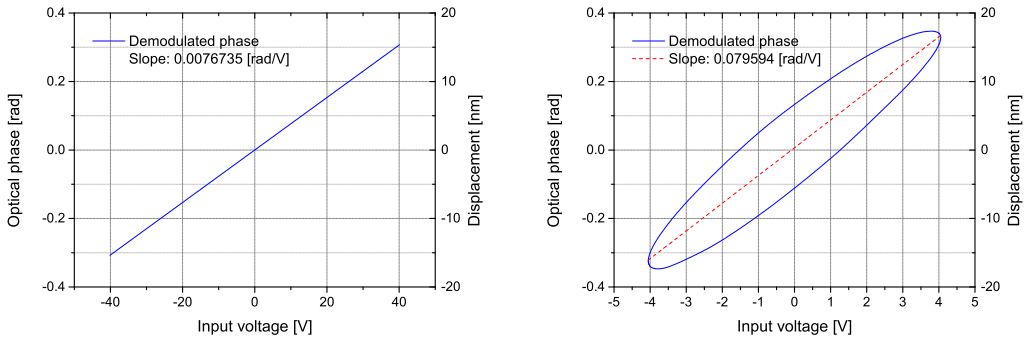

(a) (b)

Source: From author.

presents a linear response in the range analyzed.

Also, we acquire the gain in [rad/V] on surface of the transducer in 34 kHz using the speckle interferometer with digital control. The actuator was 45 mm of diameter. The result is shown in Fig. 75 with the samples and the polynomial fit in green. As can be observed, the maximum gain occurs in the central region of the transducer.

It is important to point out that this results was obtained with speckle interferometer, then, we can perform high-sensitivity measurements on objects without a polish surface, and the alignment of the sample is not crucial for the proper operation of the interferometer, once we have speckle pattern in the interferometers arm.

5.6.3 Sensor coil transducer

In the next step, we characterize a piezoelectric cylinder (in the sensor arm) with the all-fiber Mach-Zehnder interferometer and verify if the interferometer with the digital nonlinear control system was able to measure the corresponding displacement, suppressing the spurious signals. So, to generate the $\Delta\phi$, we applied a sinusoidal input signal to the PZT1 with peak voltage of 600 mV and frequency of 2 kHz. In Fig. 76, the input signal is represented as the top solid line, while the two interferometer output signals as the bottom solid and dashed line.

As we can observe, in closed-loop operation, the interferometer output signal does not present fading and the sinusoidal signal was properly recovered. It is noteworthy that the two closed-loop output signals are 180° shifted, as predicted in Eq. 26 and 27.

In a second test, a soldering iron was placed near the sensor coil to vary the temperature and to verify the robustness of the nonlinear control system. Thus, in

Figure 73 – The (a) frequency response curves and (b) displacement measurement from 34 kHz to 1150 kHz

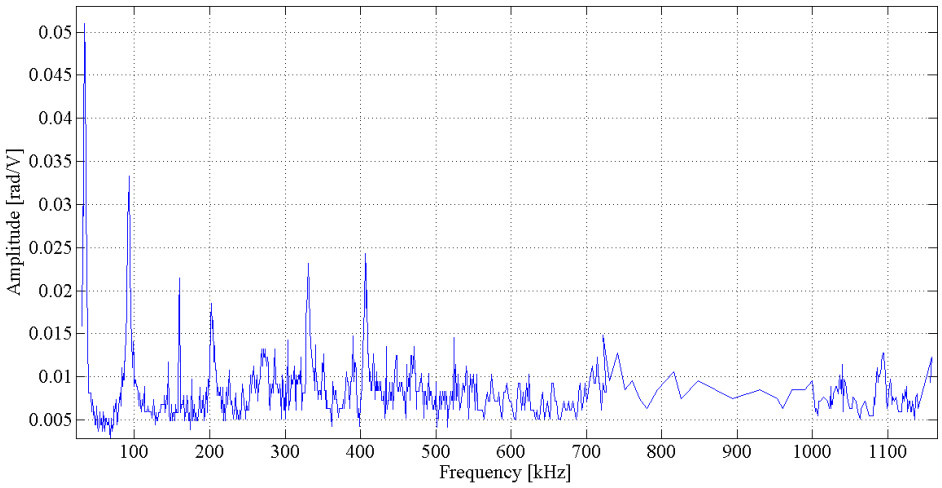

(a)

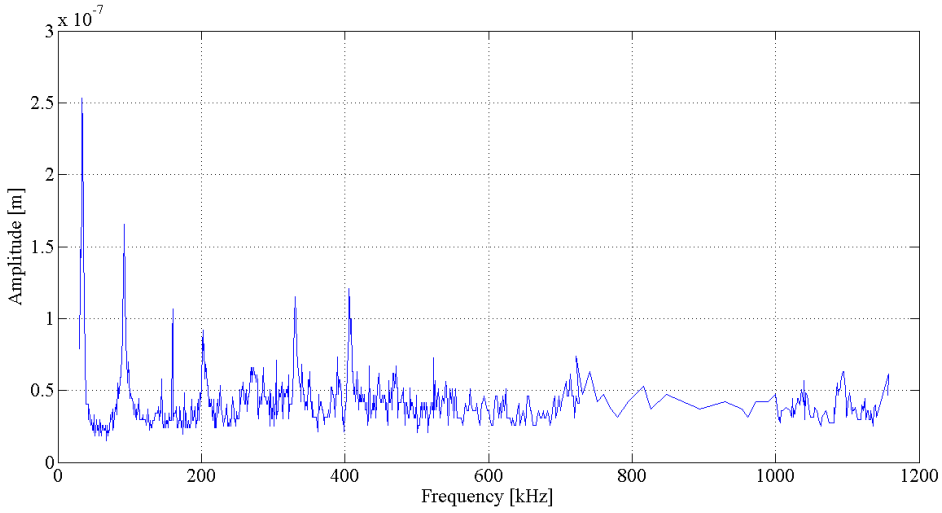

(b)

Source: From author.

open-loop operation (nonlinear controller turned off), the interferometer output presented signal fading and the amplitude drifted over 90 rad in a few seconds, which compromise the interferometer operation. On the other hand, in close-loop operation (nonlinear controller turned on), even with severe external disturbance (the soldering iron imposing a temperature variation of 430 K), the system presented a suitable behavior, i.e., the nonlinear control system satisfied the interferometer quadrature condition and eliminated signal fading.

During the experiments, we observed that all-fiber interferometers are less sensitive to mechanical disturbances than bulk interferometers. However, all-fiber interferometers

Figure 74 – Linearity curve of the transducer for 34 kHz.

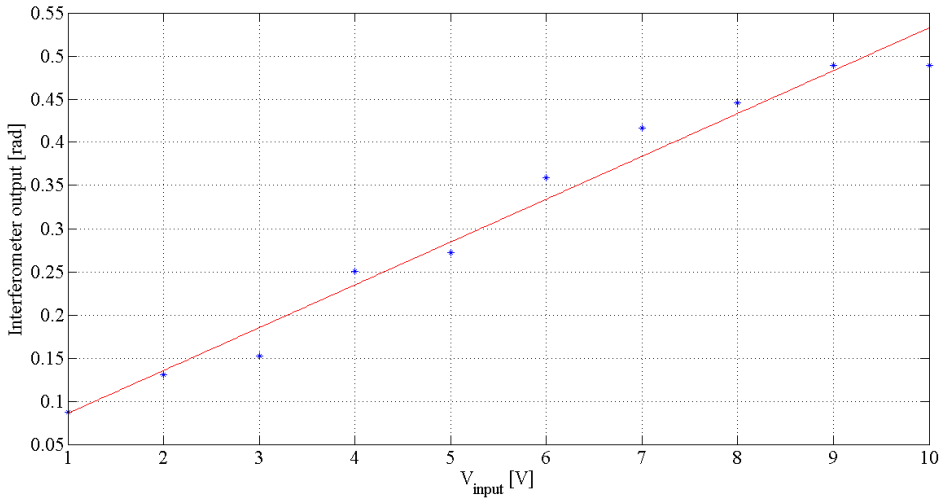

Source: From author.

Figure 75 – Surface gain of the transducer for 34 kHz.

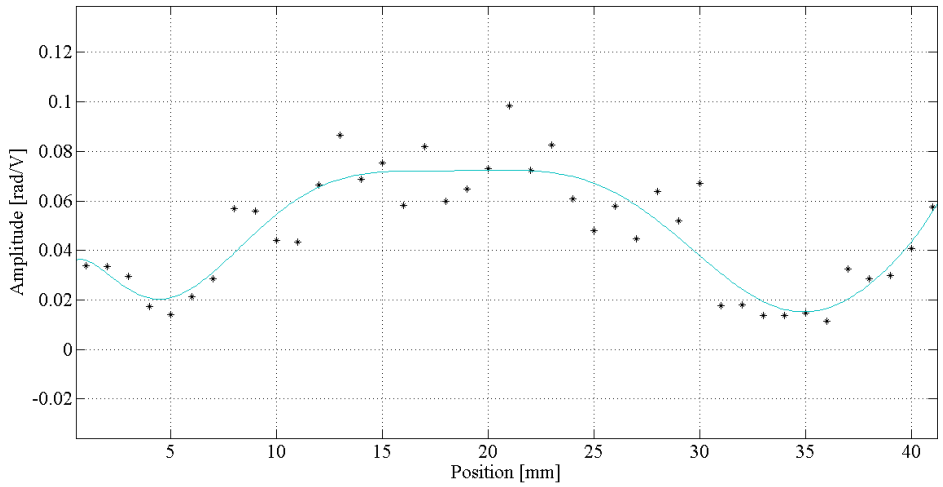

Source: From author.

are more sensitive to temperature variation, which may be due to polarization variation on the fiber mode.

Also, we noted that the nonlinear control system can deal with RF interference pick up in the control arm. For instance, when we exposed the whole system to an electronic pick up caused by inductive reactors from fluorescent lamps (approximately 8 V RMS), we observed that in open loop operation as shown in Fig. 77(a), this strong pick up was present in the interferometric output signal. On other hand, in closed loop operation shown in Fig. 77(b), the surrounding pick up was eliminated in the output signal.

Figure 76 – Interferometric input signal (top solid line) and the two outputs signals (middle solid and dashed line).

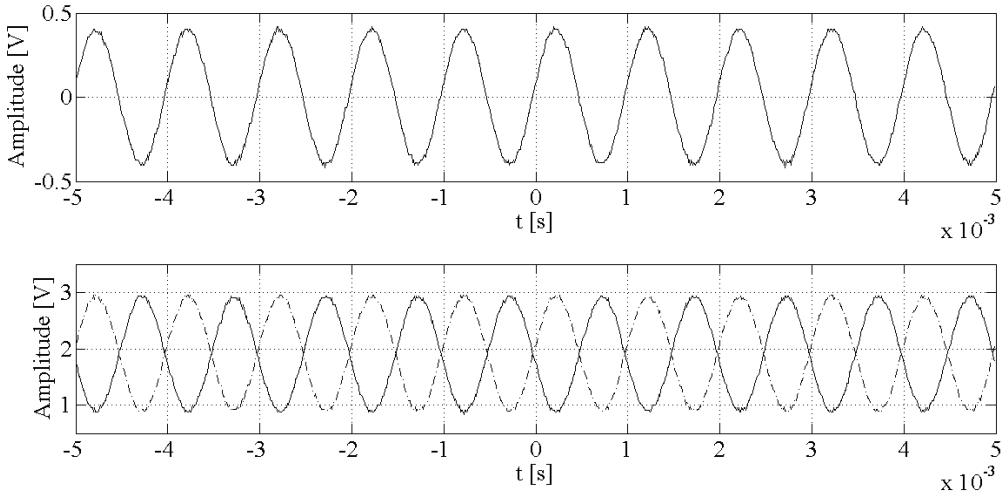

Source: From author.

Figure 77 – Interferometric input signal (yellow), two output signals (red and purple) and sign function (green), with the system expose to an RF electronic pick up (a) open loop operation and (b) closed loop operation.

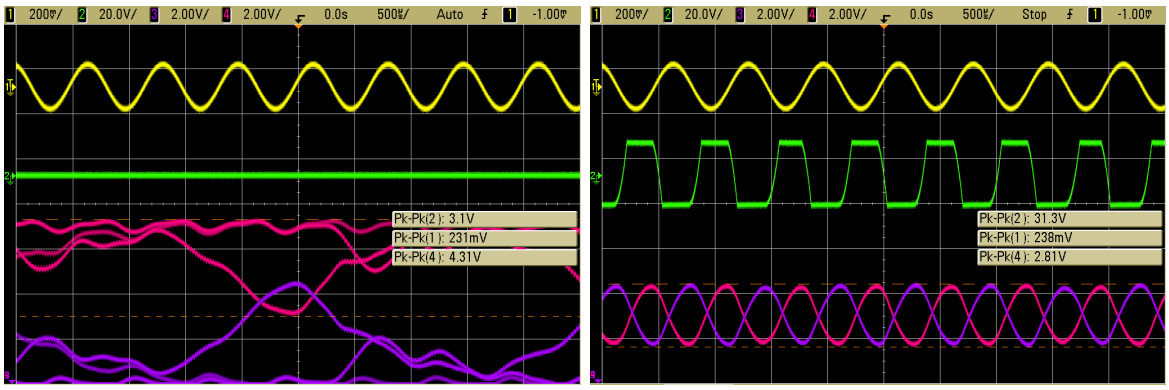

(a) (b)

Source: From author.

Finally, the frequency response curve of the phase modulator PZT4 was obtained from 1 Hz to 25 kHz, by applying sinusoidal signals on sensor arm and measuring the phase variation. The results are shown in Fig. 78. The resonance is centered approximately on 10 Hz. From the inset of Fig. 78, it can be observed that the gain for low frequency (less than 20 Hz) is 7.17 rad/V, which agrees with the total theoretical gain obtained in section 4.2.1.

Figure 78 – Frequency response of the piezoelectric transducer PZT 4.

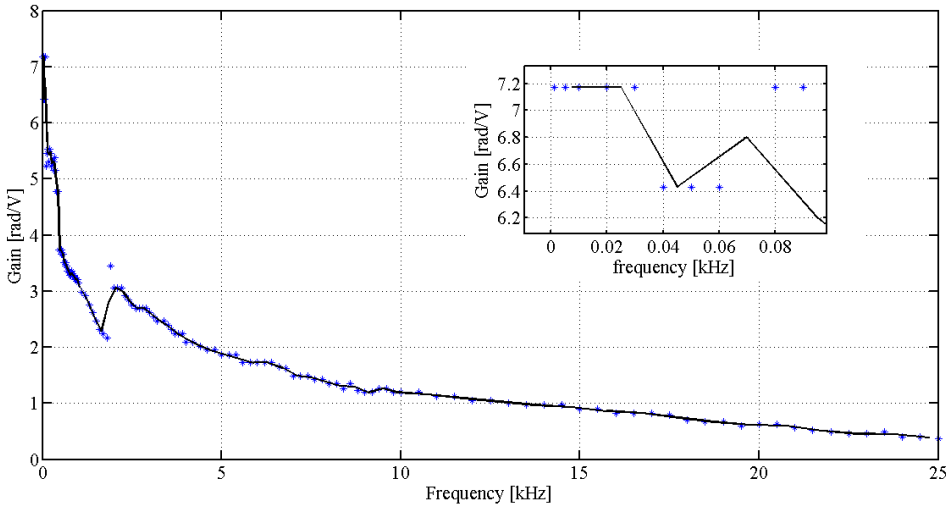

Source: From author.

5.7 Laser ultrasound detection

There are different ways to generate and receive ultrasound, being the most common by using piezoelectric transducers (SCRUBY; DRAIN, 1990; CHEEKE; DAVID, 2017). However, such transducers are contacting devices with a limited bandwidth, due to the presence of strong mechanical resonances, so that sensitivity is high only over/along a few narrow frequency bands within the spectrum of interest. Besides that, the mechanical characteristic of such transducers can vary, so that devices must be individually calibrated. Even with calibration, results depend very strongly on the quality of the mechanical coupling between transducer and surface, which in practice is highly variable. The contact transducers are also restricted to a limited temperature operation due the fluid couplants (SCRUBY; DRAIN, 1990; MCBRIDE et al., 1993; CHEEKE; DAVID, 2017).

In terms of ultrasound generation, laser techniques have received attention due the advantage of being entirely couplant free and non-contact. In additional, they have flat spectral response over large bandwidth, wide temperature range of application, high accuracy, can be used for inspection on structures with complex geometries and in hard access areas, are robot compatible, among others (SCRUBY; DRAIN, 1990; GREEN; ROBERT, 2004; CHEEKE; DAVID, 2017).

The optical interferometry may be used to detect ultrasonic waves with a large and flat broadband frequency response (SCRUBY; DRAIN, 1990; MCBRIDE et al., 1993; GREEN; ROBERT, 2004; CHEEKE; DAVID, 2017), and with the advantage of a non-contact self-calibrated technique. However, the alignment, surface conditions and stability requirements of conventional homodyne bulk and all-fiber optic interferometers limit their

use to laboratory environments. In applications outside the laboratory, the sensor must to work in the presence of much larger amplitude ($1\mu m - 1mm$) low frequency disturbance. In this way, the nonlinear control system for speckle optical interferometry proposed in this work can bring several advantages such as high-accuracy, featuring ease of implementation and high robustness for the measurements of ultrasonic waves in rough surfaces even under strong external disturbances.

Therefore, in this section, we use a closed loop bulk speckle Michelson interferometer on the ultrasonic range aiming to detect pulsed ultrasonic waves. In this case we will measure bulk waves and their velocities. The experimental setup is shown in Fig. 79, where a Q-switched Nd:YAG laser was used to generate ultrasonic pulses in aluminum and steel samples. This laser can generate longitudinal, shear and surface waves, and was operated at single shot with an energy of approximately 450 mJ and pulsewidth of 12 ns in ablation regime (SAKAMOTO, 2012).

Figure 79 – Block diagram of the experimental setup to detect pulsed ultrasonic waves.

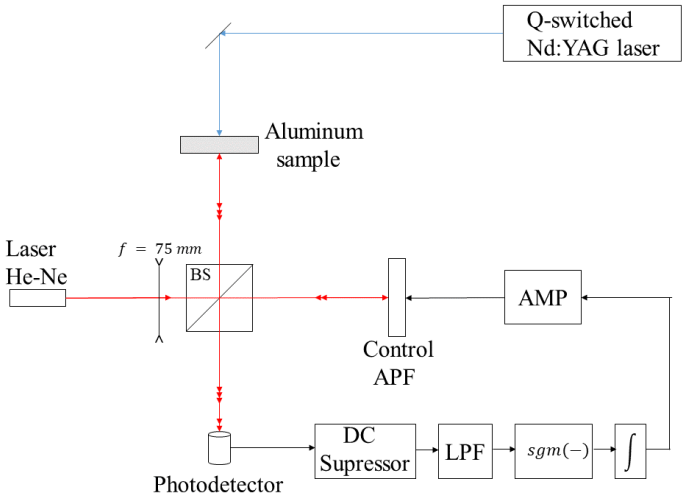

Source: From author.

5.7.1 Aluminum samples

The experiment was performed using two aluminum samples, one with 4.58 mm and the other with 9.5 mm thickness. The generation laser spot and the sensor arm of the interferometer were aligned, each one in opposite sides of the sample, as shown Fig. 79. The light pulse from the generation laser was used as a trigger on the oscilloscope to avoid jitter and delay from the electronic circuits.

The waveforms acquired are shown in Fig. 80 for the sample with 9.5 mm, where T corresponds to the trigger (light pulse), $1L$ corresponds to the first arrival of the

longitudinal wave after traveling through the thickness once, $3L$ corresponds to the second arrival of the longitudinal wave after traveling the thickness three times, and so on.

Figure 80 – Longitudinal wave detection for aluminum sample of 9.5 mm thickness for three different tests (a), (b) and (c).

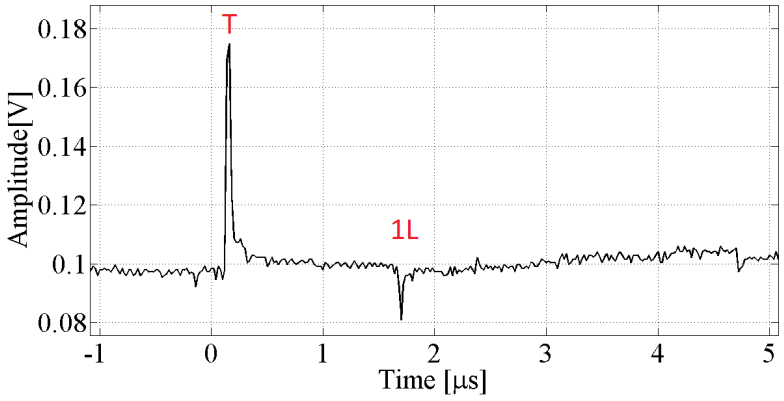

(a)

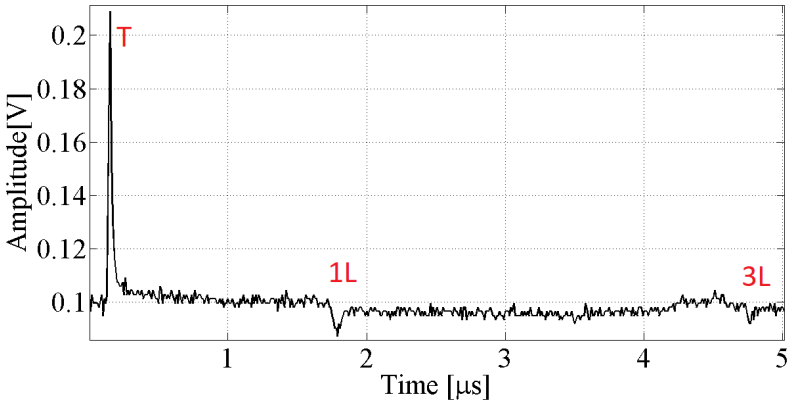

(b)

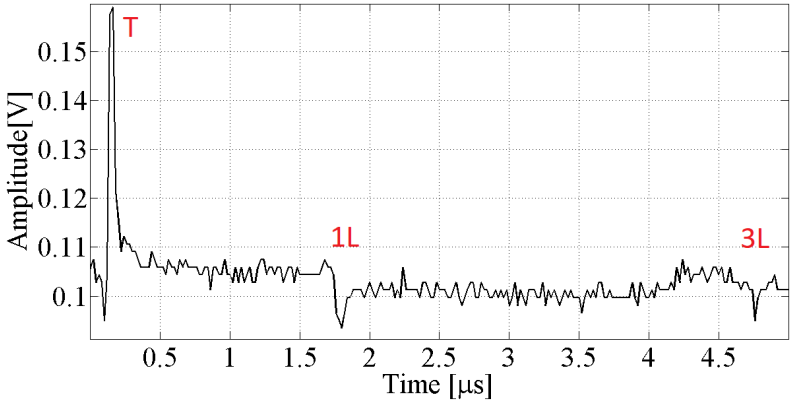

(c)

Source: From author.

The waveforms acquired for the sample with 4.58 mm thickness are shown in Fig. 81. The distance traveled by the longitudinal wave between T and $1L$ corresponds to the

thickness, i.e., $\Delta S_L = 4.58$ mm, and the distance between $1L$ and $3L$ corresponds to twice the thickness ($\Delta S_{1L} = 2 \times 4.58$ mm). The arrival time of T and $1L$ were measured as t_T and t_{1L}, therefore the time delay was calculated as $t_L = t_{1L} - t_T$. Consequently, the time delay between $1L$ and $3L$ will be $t_{1L} = t_{3L} - t_{1L}$, and so on for the other reflections. Finally, the longitudinal wave velocity was evaluated as $v_L = \Delta S_L / t_L$ and $v_{1L} = \Delta S_{1L} / t_{1L}$, and so on. The ultrasonic velocity of the longitudinal wave on aluminum, according to Sakamoto (2012), is approximately 6.375 mm/μs. The longitudinal wave velocities results obtained for the 9.5 mm and 4.58 mm thickness and the error values are shown in Tables 9 and 10, respectively.

Table 9 – Time delay and velocity between the longitudinal waves aluminum sample of 9.5 mm thickness.

-	**Test**	ΔS **[mm]**	Δt [μ **s**]	**v [mm/**μ **s]**	**Error [%]**
T - 1L	1	9.5	1.7-0.16=1.54	6.169	3.23
T - 1L	2	9.5	1.79-0.15=0.64	5.792	9.145
3L - 1L	2	19	4.77-1.79=2.98	6.376	0.015
T - 1L	3	9.5	1.78-0.15=1.63	5.828	8.58
3L - 1L	3	19	4.76-1.78=2.98	6.376	0.015

Table 10 – Time delay and velocity between the longitudinal waves aluminum sample of 4.58 mm thickness.

-	**Test**	ΔS **[mm]**	Δt [μ **s**]	**v [mm/**μ **s]**	**Error [%]**
T - 1L	1	4.58	0.934-0.148=0.786	5.827	8.59
T - 1L	2	4.58	0.93-0.15=0.78	5.871	7.9
3L - 1L	2	9.16	2.39-0.93=1.46	6.274	1.6
5L - 3L	2	9.16	3.87-2.39=1.48	6.189	2.92
7L - 5L	2	9.16	5.35-3.87=1.48	6.189	2.92
T - 1L	3	4.58	0.96-0.15=0.81	5.65	11.37
3L - 1L	3	9.16	2.4-0.96=1.44	6.361	0.22
5L - 3L	3	9.16	3.88-2.4=1.48	6.189	2.92
7L - 5L	3	9.16	5.35-3.88=1.47	6.23	2.27

One can observe through the results showed in Table 9 and 10 that the greatest errors occurs in the velocity calculated between T and $1L$. It is important to note that, the trigger is not measured by the interferometric sensor, probably causing an higher error during the time delay calculation when the trigger was taken in account. On the other hand, the error decrease considerably between $1L$ and $3L$, and so on, that are measured by the proposed sensor. Also, it must be pointed out that the AV factor for this setup was 0.083, that is a low value as predicted in Section 4.1.1.

5.7.2 Steel sample

Another experiment was performed using a steel sample plate with (0.631 ± 0.0005) mm thickness measured using a micrometer. A photograph of the experimental setup with the steel sample plate is shown in Fig. 82(a) and the scattered light by the sample in Fig. 82(b). It is important to note that, in this test, the thermoelastic regime was used and no damage is caused in the tested material.

In this step, we used two different approaches aiming to measure the system resolution. In the first one, we consider the velocity of the longitudinal wave in the medium unknown, and to measure it, we used the the sample thickness and time delay between two consecutive pulses, using the same procedure as the test with aluminum samples. For this task, we use 100 samples to measured the time delay between two consecutive pulses of (0.2045 ± 0.0042) μs. An example of the waveforms acquired is shown in Fig. 83. It is important to note that, with the speckle setup modification, shown in Section 4.1.1, we achieved a better AV factor.

Considering the measurement theory, we obtain a longitudinal wave velocity of (6.171 ± 0.131) mm/μs, which lies within the range of longitudinal velocity in steel (5.385 - 6.200 mm/μs). Therefore, calculating the distance traveled by the longitudinal wave with the velocity and considering the oscilloscope resolution of 0.001 μs, we obtain a system resolution of 0.016 mm. It is possible to see that, this resolution depends directly of the micrometer resolution, that is, the system resolution will be 10 times smaller than the resolution of the instrument used to measure the thickness.

In the second test, we calculate the sample thickness considering the velocity of the longitudinal wave in this medium is known and constant. In this case, using the velocity and the time delay with the oscilloscope resolution (0.2045 ± 0.001) μs we obtain the resolution of 0.003 mm. It is noteworthy that, if the longitudinal wave velocity is known, the system resolution will depend only on the acquisition system resolution, and in this case, we have a better accuracy in the system.

Figure 81 – Longitudinal wave detection for aluminum sample of 4.58 mm thickness for three different tests (a), (b) and (c).

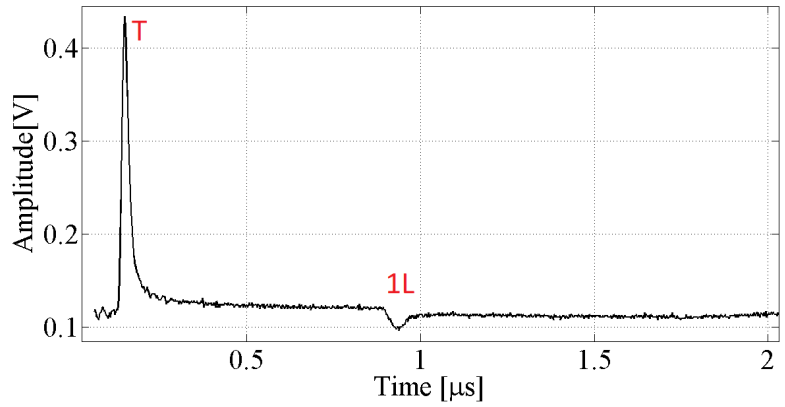

(a)

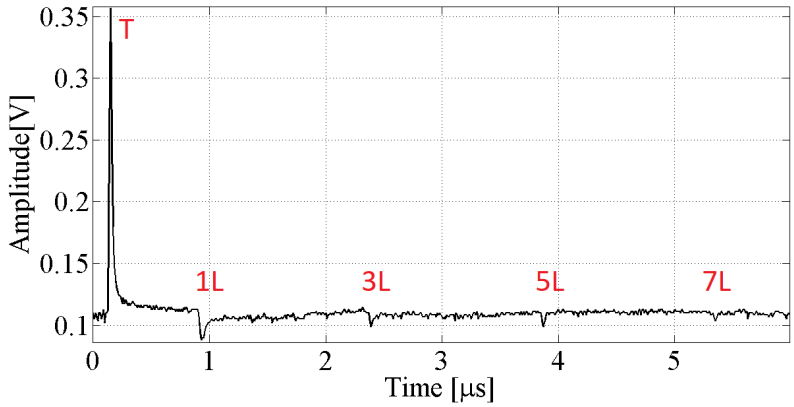

(b)

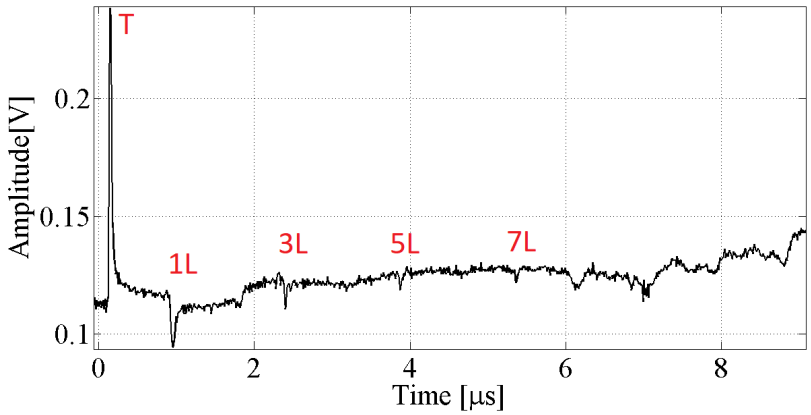

(c)

Source: From author.

Figure 82 – Photograph of the (a) experimental setup with the steel plate is shown and (b) the scattered light by the sample.

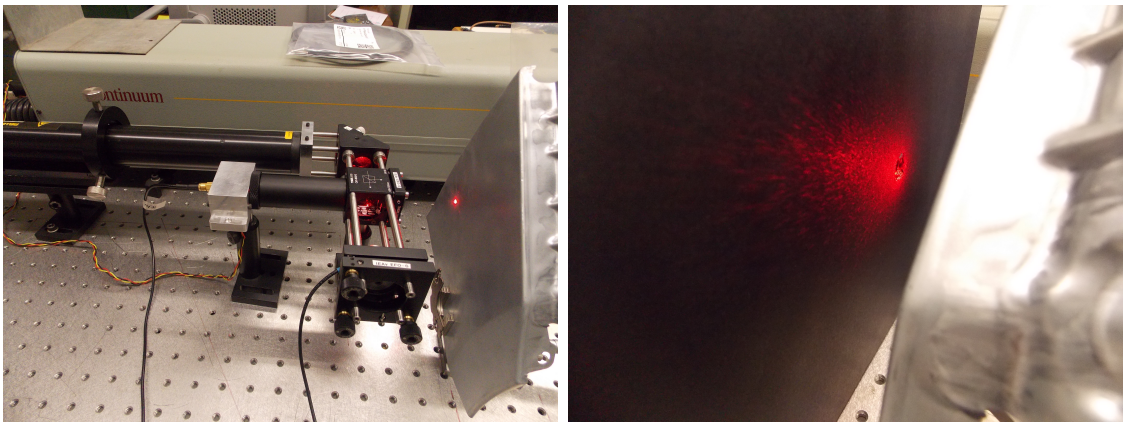

(a) (b)

Source: From author.

Figure 83 – Longitudinal wave detection for steel sample.

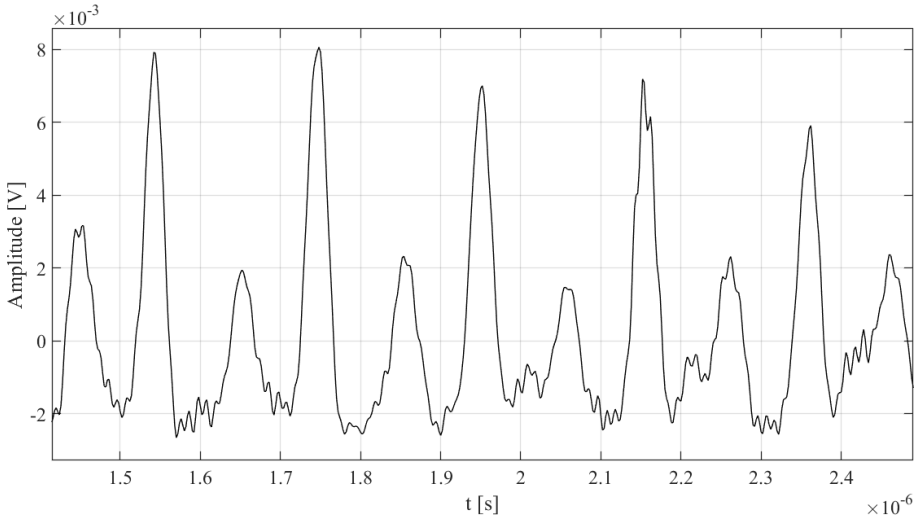

Source: From author.

6 Conclusion

The nonlinear control system for two beam optical interferometer developed in this work presented high accuracy, robustness and, furthermore, it is simple and low cost, increasing the measurement capability for different applications of interferometric sensors.

Compared with the state of the art control techniques applied in optical interferometry, the proposed system presents important features and takes into account the nonlinear characteristic of the interferometer, increasing its measurement capability. Consequently, a reset circuit is not necessary, the interferometer can work in harsh environments, the assembly and adjustment of the parameters are simpler (easy implementation), with simplicity of the setup and low cost, achieving high robustness and accuracy. Regarding demodulation techniques based on signal spectrum (SUDARSHANAM; SRINIVASAN, 1989; SUDARSHANAM; CLAUS, 1993), the proposed system has a higher dynamic range, resolution, can measure time delay and operate with arbitrary time signals. Also, it improves the temporal demodulation methods increasing the accuracy for small amplitude signals, maintaining the quadrature condition (maximum point of sensitivity) and, therefore, eliminates the effect of signal fading, even under strong external disturbances as vibration, temperature variation and air current flow.

Assembly details of the different experimental setups for bulk Michelson and all-fiber Mach-Zehnder were shown. Considering the Michelson interferometer in which the sample in the sensor arm and the piezoelectric actuator in the control arm are without mirrors, we have a speckle pattern in the output signal resulting from the scattered beam reflected by the sample. In this case, the AV factor will smaller due to the scattering of the light in the interferometer's arms. Therefore, as the AV factor decreases, the total feedback gain (γ) must increase in order to guarantee stability.

Regarding the assembly details of phase modulators with piezoelectric cylinders for all-fiber interferometers, is important to consider the gain of the phase modulator before applying control techniques. The phase modulator used for controlling requires a minimum gain, which implies the need of a large amount of fiber and leads to a greater sensitivity to spurious perturbation. Aiming to avoid loss of gain in additional layers, we then suggested the use of a linear amplifier in the control arm, or phase modulators associated in parallel (less fiber for the same gain). Also, it should be noted other advantage of the proposed system: the polarizing fading problem in all-fiber interferometer was avoided using regular fibers with the nonlinear control, which reduces even more the overall costs. This is an advantage when compared with the work of Stowe, Moore and Priest (1982), where Hi-Bi (polarization maintaining) fibers were used to control the polarization in interferometers

due to the degradation of the output signal for uncorrelated random drifts in polarization (fading).

Two distinct approaches were addressed with the nonlinear control system, low-gain and modified high-gain. The low-gain approach presents a higher frequency range, being specially suited to small amplitude with high frequencies measurements (e.g. laser ultrasonics). The modified high-gain approach can bring many advantages. For instance, it presents a much greater linear dynamic range for amplitude, good noise performance, no need for calibration process nor demodulation methods. However, it is important to consider the frequency range to apply this technique, because the control system must have a sufficient gain to fully compensate the signal of interest, and the higher the frequency of this signal the greater the gain (especially when compared to the low-gain approach). Also, when the filtering is not used in the output, the longer the fiber the closer the control signal is to the signal of interest. It occurs because the relevant disturbance signal will be much intense when compared to ambient variations.

Regarding the theoretical analysis of the controller, despite the mathematical difficulty to operate with the discontinuity of the sign function, it was possible to develop the theoretical stability study with several methods. Initially, we used Lyapunov's linearization method and the system was linearized using the sigmoid approach. In this case, we observed the occurrence of stable foci (strictly stable equilibrium points) as well as saddle points (unstable equilibrium points), and the linear approach is locally asymptotically stable. Using the first harmonic method, it was possible to obtain the system error, that depends only on the frequency of the signal of interest (ω) and the feedback gain (γ), that are well known parameters of the system. The error obtained by the first harmonic method was compared with the simulation and shown good concordance. This is a very important result due to its application when fixing the output signal in practical systems as shown in this work, increasing its overall accuracy. Through the phase plane method, we considered all the nonlinearities from the system, and we proved that for any initial condition, the nonlinear system is stable and converges to the equilibrium point. Thus, the system is globally asymptotically stable and it does not tend to a limit cycle nor to instability. Finally, we obtained the Lyapunov equation for the nonlinear system taking into account the phase plane analysis, proving the system's stability. Therefore, this approach can fully compensate the nonlinear behavior of the interferometer, keep it in the quadrature point and suppress the signal fading.

Moreover, the control system was implemented using both, discrete analog components (analog approach) and via FPGA (digital approach). The analog approach presents a low implementation cost when compared to digital one, continuous time operation, avoiding signal sampling issues (aliasing and delay). The overall system is more compact (mainly when using SMD - surface mount devices) and has wide input signal ranges.

On the other hand, the digital control approach allows the system to log the data from experimental tests, which enables the assembly of an embedded system. Another great advantage of the digital implementation is the ability to digitally configure the gain γ , allowing high gains, and consequently, a fast response of the integrator output to track the spurious disturbances, especially for the proposed setup that has a low AV value. It is noteworthy that robustness and chattering have a trade-off relationship and the implementation in FPGA provides the flexibility to change the topology of the sigmoid function, allowing optimization of the chattering which preserves the robustness. Also with the hardware designed in FPGA, the system does not present the non-idealities intrinsic to discrete components.

Furthermore, we obtained the fiber optical response in radians to temperature. It is important to note the linear relation between fiber response and temperature. Comparing the curve of the fiber response in radians with the temperature for each fiber length, we note a hysteresis in the system, which can be related with the thermal hysteresis in optical fibers. Also, we obtained the relation of fiber gain with temperature versus the fiber length. In this case, we observed that the fiber gain with temperature is linear with the fiber length. One important characteristic that was noticed is that the response of the fiber to temperature varies approximately (65.53 ± 4.3) rad/°Cm. This is a very good way to obtain very large gain with low length of fiber by applying control techniques actuating through the temperature. This is the first study aiming to use the temperature effect on optical fiber to control the interferometer. This approach will benefit the nonlinear control technique since it allows to obtain higher feedback gain with less fiber, reducing the overall cost, increasing robustness and accuracy.

Regarding the ultrasound detection, the sensor was initially tested to detect the sinusoidal vibration to the characterization of a piezoelectric actuator. The time domain signal, the sub-nanometric displacement amplitudes, linearity, hysteresis, frequency response and mechanical resonances were acquired and they proved the capability of detecting in this frequency range. Besides that, we use the closed loop interferometer to detect longitudinal waves, generated by a Q-switched laser. The velocity of the longitudinal waves were measured in aluminum samples, the error proved to be smaller than 3% between 1 L and 3 L, and so on. The greatest errors occur in the velocity calculated between T and 1 L . It is important to note that the trigger is not measured by the interferometric sensor, probably causing an higher error during the time delay calculation when the trigger was taken in account. On the other hand, the error decrease considerably between $1L$ and $3L$, and so on, that are measured by the proposed sensor.

Also, another experiment was performed to obtain the system thickness measurement resolution. Therefore, with the obtained longitudinal wave velocity and calculating the distance traveled by the longitudinal wave, considering the oscilloscope resolution of

0.001 μs, we obtain a system resolution of 0.016 mm. It is possible to see that, this resolution depends directly on the micrometer resolution, that is, the system resolution will be 10 times smaller of the instrument used to measure the thickness resolution. In the second test, we calculate the sample thickness considering the velocity of the longitudinal wave in this medium known and constant. In this case, using the velocity and the time delay with the oscilloscope resolution, we obtain the resolution of 0.003 mm. It is noteworthy that, if the longitudinal wave velocity is known, the system resolution will depend only of the acquisition system resolution, and in this case, we have a better accuracy in the system.

The development of this thesis resulted in one publication on the Optics Express journal (MARTIN et al., 2017a) and other publication in an international SPIE conference (MARTIN et al., 2017b).

6.1 Future Work

As shown in this text, the proposed control system offers many advantages to optical interferometry that may be useful in different applications in future works. Concerning future researches and the improvement of the nonlinear control system, the next steps to be taken in order to improve the sensor are presented below:

- Apply the high-gain approach (UDD; SPILLMAN, 2011) with the proposed nonlinear control technique in displacement measurements;
- Implement the nonlinear control system using Open Source software platforms (e.g. Python, C);
- Develop an application for the controlled Mach-Zehnder sensor presented, such as temperature and inertial sensors (e.g. accelerometers);
- Apply the nonlinear control method to the all-fiber Sagnac interferometer, in order to stabilize the all-fiber gyro;
- Use sub-angstrom measurement to determine a minimum detectable signal through the nonlinear control technique.

In this work, we managed to solve a great challenge of the homodyne interferometric systems, the high sensibility to spurious perturbations, reaching high robustness and accuracy with simplicity and low cost. However, the high variability of the AV factor and the DC component over time in closed-loop speckle interferometry in harsh environmental is still a challenge to be overcome. Therefore, we propose to develop a methodology aiming to eliminate the need of measuring the AV factor and the DC component and, consequently, the calibration required for interferometric system.

Bibliography

AL-ALAOUI, M. A. Novel digital integrator and differentiator. *Electronics letters*, London, v. 29, n. 4, p. 376–378, 1993. 80

AL-ALAOUI, M. A. Class of digital integrators and differentiators. *IET Signal Processing*, IET, London, v. 5, n. 2, p. 251–260, 2011. 80

ASTROM, K.; RUNDQWIST, L. Integrator windup and how to avoid it. In: IEEE AMERICAN CONTROL CONFERENCE, 1989. *Proceedings...* [S.l.]: IEEE, 1989. p. 1693–1698. 81

BARBOSA, F. d. A. A.; NADER, G.; HIGUTI, R. T.; KITANO, C.; SILVA, E. C. N. A simple interferometric method to measure the calibration factor and displacement amplification in piezoelectric flextensional actuators. *Revista Controle e Automação*, Campinas, v. 21, n. 06, p. 577–587, 2010. 15, 25

BARNES, T.; EIJU, T.; CHEUNG, D.; WU, C. Phase measurement accuracy of feedback interferometers. *Optics and lasers in engineering*, London, v. 38, n. 6, p. 387–404, 2002. 15, 16

BERGER, A.; GUTMAN, P. A new view of anti-windup design for uncertain linear systems in the frequency domain. *International Journal of Robust and Nonlinear Control*, Chichester, v. 26, n. 10, p. 2116–2135, 2016. 81

BIHAN, J. L. Novel class of digital integrators and differentiators. *Electronics Letters*, London, v. 29, n. 11, p. 971–973, 1993. 80

CARBONARI, R. C.; SILVA, E. C.; NISHIWAKI, S. Design of piezoelectric multi-actuated microtools using topology optimization. *Smart Materials and Structures*, New York, v. 14, n. 6, p. 1431, 2005. 101

CHEEKE, J.; DAVID, N. *Fundamentals and applications of ultrasonic waves*. [S.l.]: CRC, 2017. 109

CHEN, X.; ZENG, X.; FAN, D.; LIU, Q.; BIE, B.; ZHOU, X.; LUO, S. Note: Phase retrieval method for analyzing single-phase displacement interferometry data. *Review of Scientific Instruments*, Maryland, v. 85, n. 026106, 2014. 14, 15, 25

CHEUNG, D.; BARNES, T.; HASKELL, T. Feedback interferometry with membrane mirror for adaptive optics. *Optics communications*, Amsterdam, v. 218, n. 1, p. 33–41, 2003. 15, 16

CONNELLY, M.; GALETI, J.; KITANO, C. Michelson interferometer vibrometer using self-correcting synthetic-heterodyne demodulation. *Applied optics*, Washington, v. 54, n. 18, p. 5734–5738, 2015. 15

DAVIS, P.; RABINOWITZ, P. *Methods of numerical integration*. [S.l.]: Courier Corporation, 2007. 80

DECARLO, R. A.; ZAK, S. H.; MATTHEWS, G. P. Variable structure control of nonlinear multivariable systems: a tutorial. *Proceedings of the IEEE*, Piscataway, v. 76, n. 3, p. 212–232, 1988. 29

DENG, W.; LI, H.; ZHANG, C.; WANG, P. Optimization of detection accuracy of closed-loop optical voltage sensors based on Pockels effect. *Sensors*, New York, v. 17, n. 8, p. 1723, 2017. 16

DEVASIA, S.; ELEFTHERIOU, E.; MOHEIMANI, S. R. A survey of control issues in nanopositioning. *IEEE Transactions on Control Systems Technology*, Piscataway, v. 15, n. 5, p. 802–823, 2007. 14

ERTUGRUL, M.; KAYNAK, O.; SABANOVIC, A.; OHNISHI, K. A generalized approach for Lyapunov design of sliding mode controllers for motion control applications. In: INTERNATIONAL WORKSHOP ON ADVANCED MOTION CONTROL, 4., 1996. *Proceedings...* [S.l.]: IEEE, 1996. v. 1, p. 407–412. 50, 51

FELÃO, L. H. V. Digital variable structure control system implementation in FPGA applied to all-fiber optical interferometer. UNESP-Departamento de Engenharia Elétrica, 2017. 76

FRITSCH, K.; ADAMOVSKY, G. Simple circuit for feedback stabilization of a single-mode optical fiber interferometer. *Review of Scientific Instruments*, Rochester, v. 52, n. 7, p. 996–1000, 1981. 15, 16

GALETI, J.; KITANO, C.; CONNELLY, M. Improved synthetic-heterodyne Michelson interferometer vibrometer using phase and gain control feedback. *Applied optics*, Washington, v. 54, n. 35, p. 10418–10424, 2015. 15

GIALLORENZI, T.; BUCARO, J.; DANDRIDGE, A.; SIGEL, G.; COLE, J.; RASHLEIGH, S. Optical fiber sensor technology. *IEEE Transactions on Microwave Theory and Techniques*, Piscataway, v. 30, n. 4, p. 472–511, 1982. 14, 63

GRATTAN, K.; SUN, T. Fiber optic sensor technology: introduction and overview. In: *Optical Fiber Sensor Technology*. Boston: Springer, 2000. v. 82, n. 1, p. 1–44. 70

GREEN, J.; ROBERT, E. Non-contact ultrasonic techniques. *Ultrasonics*, Surrey, v. 42, n. 1-9, p. 9–16, 2004. 109

HECHT, E. *Optics*. 4. ed. San Francisco: Addison-Wesley, 2002. v. 3. (International Edition, v. 3). 14

HOCKER, G. Fiber-optic sensing of pressure and temperature. *Applied Optics*, Washington, v. 18, n. 9, p. 1445–1448, 1979. 14

HUI, L.; LAN, B.; LIJING, L.; SHULING, H.; XIUJUAN, F.; CHUNXI, Z. Tracking algorithm for the gain of the phase modulator in closed-loop optical voltage sensors. *Optics & Laser Technology*, Amsterdam, v. 47, p. 214–220, 2013. 16

JACKSON, D.; PRIEST, R.; DANDRIDGE, A.; TVETEN, A. Elimination of drift in a single-mode optical fiber interferometer using a piezoelectrically stretched coiled fiber. *Applied Optics*, Washington, v. 19, n. 17, p. 2926–2929, 1980. 15, 16, 65, 67, 68

JING, W.; ZHANG, Y.; ZHOU, G.; TANG, F.; LI, H. Measurement accuracy improvement with PZT scanning for detection of DPC in Hi-Bi fibers. *Optics Express*, Washington, v. 10, n. 15, p. 685–690, 2002. 14

KAPOOR, N.; TEEL, A.; DAOUTIDIS, P. An anti-windup design for linear systems with input saturation. *Automatica*, Elmsford, v. 34, n. 5, p. 559–574, 1998. 81

MAIMAN, T. Stimulated optical radiation in ruby. *Nature*, Springer, New York, v. 187, n. 4736, p. 493–494, 1960. 14

MALACARA, D. *Optical shop testing*. [S.l.]: John Wiley & Sons, 2007. v. 59. 59, 60

MARTIN, R. I.; SAKAMOTO, J. M. S.; TEIXEIRA, M. C. M.; MARTINEZ, G. A.; PEREIRA, F. d. C.; KITANO, C. Nonlinear control system for optical interferometry based on variable structure control and sliding modes. *Optics Express*, Washington, v. 25, n. 6, p. 6335–6348, 2017a. 33, 36, 63, 103, 119

MARTIN, R. I.; SAKAMOTO, J. M. S.; TEIXEIRA, M. C. M.; KITANO, C. Variable structure and sliding modes nonlinear control system applied to a fiber optic interferometer. In: INTERNATIONAL CONFERENCE ON APPLICATIONS OF OPTICS AND PHOTONICS, 3. *Proceedings...* Faro, 2017b. 64, 71, 103, 119

MCBRIDE, R.; CAROLAN, T.; BARTON, J.; WILCOX, S.; BORTHWICK, W.; JONES, J. Detection of acoustic emission in cutting processes by fibre optic interferometry. *Measurement Science and Technology*, Bristol, v. 4, n. 10, p. 1122, 1993. 109

MILNE-THOMSON, L. M.; ABRAMOWITZ, M.; STEGUN, I. A. *Handbook of mathematical functions*. [S.l.]: Dover Publications, 1972. 19

MOORE, A.; MCBRIDE, R.; BARTON, J.; JONES, J. Closed-loop phase stepping in a calibrated fiber-optic fringe projector for shape measurement. *Applied Optics*, Washington, v. 41, n. 16, p. 3348–3354, 2002. 15, 26

MURPHY, K.; GUNTHER, M.; VENGSARKAR, A.; CLAUS, R. Quadrature phase-shifted, extrinsic Fabry-Perot optical fiber sensors. *Optics Letters*, Optical Society of America, Washington, v. 16, n. 4, p. 273–275, 1991. 14

NATIONAL INSTRUMENTS. *NI myRIO-1900*: user guide and specifications. Redmond, 2013. 32 p. 77

2016]dmafifo NATIONAL INSTRUMENTS. *What is the difference between configuring the number of elements in a FIFO and requesting the depth of the FIFO*. [S. l.], 2016. Available in: <http://digital.ni.com/public.nsf/allkb/1B7F7C2C9A650DE186257B6E003FDED4>. Accessed in: 15 Mar. 2017.

OGATA, K.; SEVERO, B. *Engenharia de controle moderno*. [S.l.]: Prentice Hall do Brasil, 1998. 35

PANG, M.; ZHANG, M.; WANG, L.; ZOU, Q.; KUANG, W.; WANG, D.; ; LIAO, Y. Phase mode-matching demodulation scheme for interferometric fiber-optic sensors. *IEEE Photonics Technology Letters*, Piscataway, v. 19, n. 1, p. 39–41, 2007. 15, 25

PAPAMARKOS, N.; CHAMZAS, C. A new approach for the design of digital integrators: Fundamental theory and applications. *IEEE Transactions on Circuits and Systems I*, Piscataway, v. 43, n. 9, p. 785–791, 1996. 80

PARKS, T.; BURRUS, C. *Digital filter design*. [S.l.]: Wiley-Interscience, 1987. 78

PENG, Y.; VRANCIC, D.; HANUS, R. Anti-windup, bumpless, and conditioned transfer techniques for PID controllers. *IEEE Control Systems*, Piscataway, v. 16, n. 4, p. 48–57, 1996. 81

PISANI, M. A homodyne Michelson interferometer with sub-picometer resolution. *Measurement Science and Technology*, Bristol, v. 20, n. 8, p. 084008, 2009. 15, 25

PUTRA, A.; HUANG, S.; TAN, K.; PANDA, S.; LEE, T. Design, modeling, and control of piezoelectric actuators for intracytoplasmic sperm injection. *IEEE Transactions on Control Systems Technology*, Piscataway, v. 15, n. 5, p. 879–890, 2007. 14

RAN, M.; WANG, Q.; DONG, C. Anti-windup design for uncertain nonlinear systems subject to actuator saturation and external disturbance. *International Journal of Robust and Nonlinear Control*, Chichester, v. 26, n. 15, p. 3421–3438, 2016. 81

SAKAMOTO, J. M. S. *Laser ultrasonics system with a fiber optic angular displacement sensor*. 2012. 177 p. Tese (PhD Thesis in Spatial Sciences and Technologies) — Instituto Tecnológico de Aeronáutica, São José dos Campos, 2012. 110, 112

SCRUBY, C.; DRAIN, L. *Laser ultrasonics techniques and applications*. [S.l.]: CRC, 1990. 109

SHEEM, S.; GIALLORENZI, T. G.; KOO, K. Optical techniques to solve the signal fading problem in fiber interferometers. *Applied Optics*, Washington, v. 21, n. 4, p. 689–693, 1982. 14

SHIRAI, T.; BARNES, T.; HASKEL, T. Surface-profile measurement by means of a polarization Sagnac interferometer with parallel optical feedback. *Optics letters*, Washington, v. 24, n. 5, p. 297–299, 1999. 15

SLOTINE, J.; LI, W. et al. *Applied nonlinear control*. New Jersey: Prentice hall Englewood Cliffs, 1991. v. 199. 16, 34, 36, 41, 45, 50, 51, 53, 54

SLOTINE, K.; SASTRY, S. Tracking control of non-linear systems using sliding surfaces, with application to robot manipulators. *International journal of control*, London, v. 38, n. 2, p. 465–492, 1983. 50, 51

STEINHART, J. S.; HART, S. R. Calibration curves for thermistors. In: *Deep Sea Research and Oceanographic Abstracts*. [S.l.: s.n.], 1968. v. 15, n. 4, p. 497–503. 95

STOWE, D.; MOORE, D.; PRIEST, R. Polarization fading in fiber interferometric sensors. *IEEE Transactions on Microwave and Techniques*, Piscataway, v. 30, n. 10, p. 1632–1635, 1982. 63, 116

SUDARSHANAM, V.; CLAUS, R. O. Generic J1...J4 method of optical phase detection: accuracy and range enhancement. *Journal of Modern Optics*, Abingdon, v. 40, n. 3, p. 483–492, 1993. 15, 25, 116

SUDARSHANAM, V.; SRINIVASAN, K. Linear readout of dynamic phase change in a fiber-optic homodyne interferometer. *Optics letters*, Washington, v. 14, n. 2, p. 140–142, 1989. 15, 25, 116

SVELTO, O.; HANNA, D. *Principles of lasers*. [S.l.]: Springer, 1998. v. 4. 70

TSENG, C.-C. Design of FIR and IIR fractional order simpson digital integrators. *Signal Processing*, Amsterdam, v. 87, n. 5, p. 1045–1057, 2007. 80

TURNER, M. C.; SOFRONY, J.; HERRMANN, G. An alternative approach to anti-windup in anticipation of actuator saturation. *International Journal of Robust and Nonlinear Control*, Chichester, v. 27, n. 6, p. 963–980, 2016. 81

UDD, E.; SPILLMAN, W. B. J. *Fiber Optic Sensors: an introduction for engineers and scientists*. New York: Wiley, 2011. 14, 20, 21, 27, 28, 63, 119

UTKIN, V. Sliding modes and their applications in variable structure systems. *Moscow*, 1978. 29

VALI, V.; SHORTHILL, R. Fiber ring interferometer. *Applied optics*, New York, v. 15, n. 5, p. 1099–1100, 1976. 14

VERMA, S.; KIM, W.; SHAKIR, H. Multiaxis maglev nanopositioner for precision manufacturing and manipulation applications. In: INDUSTRY APPLICATIONS CONFERENCE - IAS ANNUAL MEETING, 39., 2004. *Proceedings...* Piscataway: IEEE, 2005. v. 3, p. 2084–2091. 14

WHITE, R.; EMMONY, D. Active feedback stabilisation of a Michelson interferometer using a flexure element. *Journal of Physics E: Scientific Instruments*, London, v. 18, n. 8, p. 658, 1985. 15, 16

XIE, F.; CHEN, X.; ZHANG, L. High stability interleaved fiber Michelson interferometer for on-line precision displacement measurements. *Optics and Lasers in Engineering*, Amsterdam, v. 47, n. 11, p. 1301–1306, 2009. 16

XIE, F.; CHEN, Z.; REN, J. Stabilisation of an optical fiber Michelson interferometer measurement system using a simple feedback circuit. *Measurement*, Amsterdam, v. 42, n. 9, p. 1335–1340, 2009. 16

XIE, F.; REN, J.; CHEN, Z.; FENG, Q. Vibration-displacement measurements with a highly stabilised optical fiber Michelson interferometer system. *Optics & Laser Technology*, Elsevier, Amsterdam, v. 42, n. 1, p. 208–213, 2010. 14

YIMNIRUN, R.; MOSES, P.; JR, R. M.; NEWNHAM, R. A single-beam interferometer with sub-ångström displacement resolution for electrostriction measurements. *Measurement Science and Technology*, Bristol, v. 14, n. 6, p. 766, 2003. 14

YOUNG, K. D.; UTKIN, V. I.; OZGUNER, U. A control engineer's guide to sliding mode control. In: IEEE INTERNATIONAL WORKSHOP ON VARIABLE STRUCTURE SYSTEMS, 1996; [S.l.]. *Proceedings...* [S.l.]: IEEE, 1996. p. 1–14. 50, 76

YU, M.; DYER, M.; SKIDMORE, G.; ROHRS, H.; LU, X.; AUSMAN, K. D.; EHR, J. R. V.; RUOFF, R. S. Three-dimensional manipulation of carbon nanotubes under a scanning electron microscope. *Nanotechnology*, Bristol, v. 10, n. 3, p. 244, 1999. 14

ZHEN, S.; CHEN, B.; YUAN, L.; LI, M.; LIANG, J.; YU, B. A novel interferometric vibration measurement sensor with quadrature detection based on $\lambda/8$ wave plate. *Optics & Laser Technology*, Amsterdam, v. 42, n. 2, p. 362–365, 2010. 15

ZHENG, A.; KOTHARE, M.; MORARI, M. Anti-windup design for internal model control. *International Journal of Control*, London, v. 60, n. 5, p. 1015–1024, 1994. 81